

MICROCOPY RESOLUTION TEST CHART
NATIONAL BUREAU OF STANDARDS-1963-A

AD-A184 132

DTIC FILE COPY

2

NAVAL POSTGRADUATE SCHOOL
Monterey, California



DTIC
ELECTE
SEP 04 1987
S D
C.D.

THESIS

NUMERICAL SIMULATION OF
UNSTEADY SEPARATED FLOWS

by

Samir I. M. Mostafa

June 1987

Thesis Advisor

T. Sarpkaya

Approved for public release; distribution is unlimited.

87 9 1 312

REPORT DOCUMENTATION PAGE

1a REPORT SECURITY CLASSIFICATION Unclassified		1b RESTRICTIVE MARKINGS	
2a SECURITY CLASSIFICATION AUTHORITY		3 DISTRIBUTION/AVAILABILITY OF REPORT Approved for public release, distribution is unlimited.	
2b DECLASSIFICATION/DOWNGRADING SCHEDULE			
4 PERFORMING ORGANIZATION REPORT NUMBER(S)		5 MONITORING ORGANIZATION REPORT NUMBER(S)	
6a NAME OF PERFORMING ORGANIZATION Naval Postgraduate School	6b OFFICE SYMBOL (if applicable) 69	7a NAME OF MONITORING ORGANIZATION Naval Postgraduate School	
6c ADDRESS (City, State, and ZIP Code) Monterey, CA., 93943-5000		7b ADDRESS (City, State, and ZIP Code) Monterey, California 93943-5000	
8a NAME OF FUNDING/SPONSORING ORGANIZATION	8b OFFICE SYMBOL (if applicable)	9 PROCUREMENT INSTRUMENT IDENTIFICATION NUMBER	
8c ADDRESS (City, State, and ZIP Code)		10 SOURCE OF FUNDING NUMBERS	
		PROGRAM ELEMENT NO	PROJECT NO
		TASK NO	WORK UNIT ACCESSION NO
11 TITLE (Include Security Classification) NUMERICAL SIMULATION OF UNSTEADY SEPARATED FLOWS			
12 PERSONAL AUTHOR(S) Mostafa, Samir Ismail Mohamed			
13a TYPE OF REPORT Ph.D. Dissertation	13b TIME COVERED FROM _____ TO _____	14 DATE OF REPORT (Year, Month, Day) 1987 June	15 PAGE COUNT 141
16 SUPPLEMENTARY NOTATION			
17 COSATI CODES		18 SUBJECT TERMS (Continue on reverse if necessary and identify by block number) Discrete Vortex Model, Harmonic Flow, Cambered Plate, Unsteady Flow, Vortex Motion.	
FIELD	GROUP		
	SUB-GROUP		
19 ABSTRACT (Continue on reverse if necessary and identify by block number) Two unsteady flows dominated by the occurrence of separation are simulated through the use of the discrete vortex model. The first of these is a sinusoidally oscillating flow about a circular cylinder at a Keulegan-Carpenter number of $K=10$. The vortex model has been combined with the boundary layer calculations and the positions of the separation and stagnation points, the evolution of the wake, the velocity and pressure distributions, and the instantaneous forces have been calculated and compared, whenever possible, with those obtained experimentally. The model has successfully simulated the occurrence of the transverse half Karman vortex street. The calculated positions of the vortices were found to be in good agreement with those obtained experimentally. The measured and calculated in-line forces and the differential pressure distributions showed reasonably good agreement.			
20 DISTRIBUTION/AVAILABILITY OF ABSTRACT <input checked="" type="checkbox"/> UNCLASSIFIED/UNLIMITED <input type="checkbox"/> SAME AS RPT <input type="checkbox"/> DTIC USERS		21 ABSTRACT SECURITY CLASSIFICATION UNCLASSIFIED	
22a NAME OF RESPONSIBLE INDIVIDUAL Professor T. Sarpkaya		22b TELEPHONE (Include Area Code) (408) 646-3425	22c OFFICE SYMBOL 69-SL

19. ABSTRACT (Con't)

The second simulation dealt with a rapidly decelerating flow about a two-dimensional sharp-edged camber. An extensive study of the velocity field in the vicinity of the singular points led to the development of a novel method for the introduction of vorticity at variable time intervals. The measured and calculated characteristics of the flow, such as the evolution of the wake and the forces acting on the camber, were found to be in excellent agreement. Furthermore, the simulation provided a plausible explanation for the cause of parachute collapse, a phenomenon which gave impetus to the numerical and physical experiments described herein.

Accession For	
NTIS CRARI	<input checked="" type="checkbox"/>
DTIC TAB	<input type="checkbox"/>
Unannounced	<input type="checkbox"/>
Justification	
By	
Distribution/	
Availability Codes	
Dist	Avail and/or Special
A-1	



Approved for public release; distribution is unlimited.

Numerical Simulation of
Unsteady Separated Flows

by

Samir I. M. Mostafa
Colonel, Egyptian Airforce
B.S., Cairo University, 1970
M.S., Cairo University, 1981

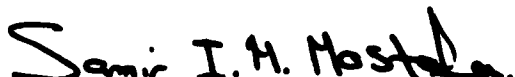
Submitted in partial fulfillment of the
requirements for the degree of

DOCTOR OF PHILOSOPHY IN MECHANICAL ENGINEERING

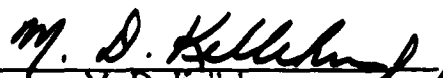
from the

NAVAL POSTGRADUATE SCHOOL
June 1987

Author:

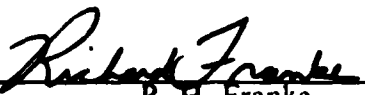

Samir I. M. Mostafa

Approved by:


M. D. Kelleher
Professor of Mechanical Engineering


R. H. Nunn
Professor of Mechanical Engineering


G. J. Thaler, Distinguished
Professor of Electrical
and Computer Engineering

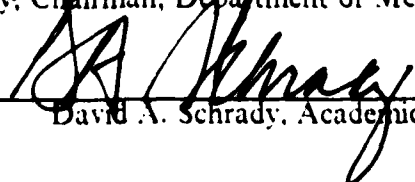

R. H. Franke
Professor of Mathematics


T. Sarpkaya, Distinguished
Professor of Mechanical Engineering
Dissertation Supervisor

Approved by:


A. J. Healey, Chairman, Department of Mechanical Engineering

Approved by:


David A. Schrad, Academic Dean

ABSTRACT

Two unsteady flows dominated by the occurrence of separation are simulated through the use of the discrete vortex model. The first of these is a sinusoidally oscillating flow about a circular cylinder at a Keulegan-Carpenter number of $K = 10$. The vortex model has been combined with the boundary layer calculations and the positions of the separation and stagnation points, the evolution of the wake, the velocity and pressure distributions, and the instantaneous forces have been calculated and compared, whenever possible, with those obtained experimentally. The model has successfully simulated the occurrence of the transverse half Karman vortex street. The calculated positions of the vortices were found to be in good agreement with those obtained experimentally. The measured and calculated in-line forces and the differential pressure distributions showed reasonably good agreement.

The second simulation dealt with a rapidly decelerating flow about a two-dimensional sharp-edged camber. An extensive study of the velocity field in the vicinity of the singular points led to the development of a novel method for the introduction of vorticity at variable time intervals. The measured and calculated characteristics of the flow, such as the evolution of the wake and the forces acting on the camber, were found to be in excellent agreement. Furthermore, the simulation provided a plausible explanation for the cause of parachute collapse, a phenomenon which gave impetus to the numerical and physical experiments described herein.

TABLE OF CONTENTS

I.	DISCRETE VORTEX ANALYSIS OF SINUSOIDALLY OSCILLATING FLOW ABOUT CIRCULAR CYLINDERS	14
A.	INTRODUCTION	14
B.	NUMERICAL SOLUTION OF THE NAVIER-STOKES EQUATIONS	16
C.	VORTEX METHODS	17
1.	Discrete Vortex Analysis	17
2.	Formulation of the Problem	19
3.	Specific Details of Creation and Convection of the Vortices	19
4.	Discussion of Results	22
D.	CONCLUDING REMARKS ON OSCILLATING FLOW ABOUT CYLINDERS	57
II.	DISCRETE VORTEX ANALYSIS OF UNSTEADY FLOW ABOUT CAMBERED PLATES	59
A.	INTRODUCTION	59
III.	ANALYSIS	61
A.	TRANSFORMATIONS AND THE COMPLEX VELOCITY POTENTIAL	61
B.	COMPLEX VELOCITIES OF VORTICES	63
C.	KUTTA CONDITION	65
D.	TIP VELOCITY	67
E.	TIME DEPENDENT-FORCES	68
F.	METHOD OF CALCULATION	70
IV.	DISCUSSION OF RESULTS	88
A.	NUMERICAL AND PHYSICAL EXPERIMENTS	88
B.	CONCLUDING REMARKS	109

V. CONCLUSIONS	117
APPENDIX A: NUMERICAL RESULTS	119
LIST OF REFERENCES	137
INITIAL DISTRIBUTION LIST	140

LIST OF TABLES

1. SUMMARY OF THE PARAMETRIC RELATIONSHIP 62

LIST OF FIGURES

1.1	Time sequence from flow visualization experiments ($0.12 < T^* < 1.00$)	24
1.2	Time sequence from flow visualization experiments ($1.13 < T^* < 1.75$)	25
1.3	Position of vortices, velocity and pressure distributions at $T^* = 0.200$	27
1.4	Position of vortices, velocity and pressure distributions at $T^* = 0.4875$	28
1.5	Position of vortices, velocity and pressure distributions at $T^* = 0.6063$	29
1.6	Position of vortices, velocity and pressure distributions at $T^* = 0.7625$	30
1.7	Position of vortices, velocity and pressure distributions at $T^* = 0.8625$	31
1.8	Flow field at $T^* = 0.500$	34
1.9	Flow field at $T^* = 0.625$	35
1.10	Flow field at $T^* = 0.750$	36
1.11	Flow field at $T^* = 0.875$	37
1.12	Flow field at $T^* = 1.00$	38
1.13	Flow field at $T^* = 1.125$	39
1.14	Flow field at $T^* = 1.250$	40
1.15	Flow field at $T^* = 1.375$	41
1.16	Flow field at $T^* = 1.500$	42
1.17	Flow field at $T^* = 1.625$	43
1.18	Flow field at $T^* = 1.750$	44
1.19	Flow field at $T^* = 1.875$	45
1.20	Flow field at $T^* = 2.00$	46
1.21	Comparison of numerical and experimental differential pressures	48
1.22	The calculated drag coefficient	49
1.23	The calculated lift coefficient	50
1.24	Measured and calculated drag force	52
1.25	Upstream stagnation point	53
1.26	Downstream stagnation point	54
1.27	Primary separation points	55
1.28	Secondary separation points	56

1.29	Vorticity fed into the flow field	58
3.1	Circle and physical planes	61
3.2	Tip region in the circle and physical planes	72
3.3	Velocity profile along the radial line (nascent vortex on OM)	73
3.4	Velocity profile along the radial line (nascent vortex to the right of OM)	75
3.5	Velocity profile along the radial line (nascent vortex on OZ)	76
3.6	Three-dimensional plot of and the contour lines for Γ distribution	77
3.7	Three-dimensional plot of the velocity ratio	78
3.8	Three-dimensional plot of the tip velocity	79
3.9	Velocity profile along the radial line (nascent vortex at $\epsilon = 0.05$, $\delta\theta = 25.0^\circ$)	80
3.10	Velocity profile along the radial line (nascent vortex at $\epsilon = 0.10$, $\delta\theta = 25.0^\circ$)	81
3.11	Velocity profile along the radial line (nascent vortex at $\epsilon = 0.20$, $\delta\theta = 25.0^\circ$)	82
3.12	Velocity field in the vicinity of the tip	84
4.1	Variations of the velocity and the acceleration	89
4.2	Position of vortices and tangential velocity distribution	90
4.3	Velocity profile along the radial line passing through the tip	91
4.4	Pressure distribution on the upstream and downstream faces	92
4.5	Tangential velocity at $T^* = 10.84$	94
4.6	Tip velocity at $T^* = 10.84$	95
4.7	Pressure distribution at $T^* = 10.84$	96
4.8	Tangential velocity at $T^* = 17.86$	97
4.9	Tip velocity at $T^* = 17.86$	98
4.10	Pressure distribution at $T^* = 17.86$	99
4.11	The velocity field about the camber at $T^* = 4.35$	100
4.12	The velocity field about the camber at $T^* = 6.05$	101
4.13	The velocity field about the camber at $T^* = 8.55$	103
4.14	The velocity field about the camber at $T^* = 14.20$	104
4.15	The velocity field about the camber at $T^* = 16.30$	105
4.16	The velocity field about the camber at $T^* = 21.50$	106
4.17	Variation of V_1 with time	107

4.18	Variation of V_2 with time	108
4.19	Drag coefficient calculated from pressure integration	110
4.20	Drag coefficient calculated from impulse expression	111
4.21	Calculated and measured drag coefficients	112
4.22	Comparison of flow fields at $T^* = 6.05$	113
4.23	Comparison of flow fields at $T^* = 8.55$	114
4.24	Comparison of flow fields at $T^* = 16.30$	115
A.1	Position of vortices, velocity and pressure distribution at $T^* = 1.025$	120
A.2	Position of vortices, velocity and pressure distribution at $T^* = 1.100$	121
A.3	Position of vortices, velocity and pressure distribution at $T^* = 1.250$	122
A.4	Position of vortices, velocity and pressure distribution at $T^* = 1.350$	123
A.5	Position of vortices, velocity and pressure distribution at $T^* = 1.525$	124
A.6	Position of vortices, velocity and pressure distribution at $T^* = 1.600$	125
A.7	Differential pressure distributions at $T^* = 1.350$ and 1.600	126
A.8	Position of vortices, velocity and pressure distribution at $T^* = 1.756$	127
A.9	Position of vortices, velocity and pressure distribution at $T^* = 1.850$	128
A.10	Position of vortices, velocity and pressure distribution at $T^* = 1.950$	129
A.11	Position of vortices, velocity and pressure distribution at $T^* = 2.250$	130
A.12	Position of vortices, velocity and pressure distribution at $T^* = 2.300$	131
A.13	Position of vortices, velocity and pressure distribution at $T^* = 2.450$	132
A.14	Position of vortices, velocity and pressure distribution at $T^* = 2.550$	133
A.15	Position of vortices, velocity and pressure distribution at $T^* = 2.725$	134
A.16	Position of vortices, velocity and pressure distribution at $T^* = 2.925$	135
A.17	Position of vortices, velocity and pressure distribution at $T^* = 2.975$	136

TABLE OF SYMBOLS AND ABBREVIATIONS

4b	Chord Length of the Cambered Plate.
C_d	Drag Coefficient. = $D/\rho c U_m^2$ for Circular Cylinder. = $D/2\rho b U_o^2$ for Cambered plate.
C_L	Lift Coefficient. = $L/\rho c U_m^2$ for Circular Cylinder. = $L/2\rho b U_o^2$ for Cambered plate.
C_p	Pressure Coefficient.
c	Radius of the Circular Cylinder.
D	Drag Force (in Pounds/ft).
i	= $\sqrt{-1}$
K	Keulegan-Carpenter Number.
L	Lift Force (in Pounds/ft).
q	Velocity Vector.
$\Re []$	Real Part of a Complex Quantity.
Re	Reynolds Number.
r	Radial Distance.
r^*	Vortex Core Radius.
T	Period of Oscillation of Ambient Flow Velocity.
T^*	Nondimensional Time. = t/T for Oscillating Flow Case. = Ut/c for Cambered plate.
t	Time (in seconds).
U	Ambient Flow Velocity (in ft/s).
U_m	Ambient Velocity Amplitude.
U_o	Reference Velocity.
U_s	Flow Velocity at Separation Point.
U_{max}	Maximum Value of Tangential Flow Velocity.
\dot{U}	Ambient Flow Acceleration (in ft/s^2).
u	x-Component of Velocity.
V_1	Tip Velocity.

V_2	Velocity at the Inner Edge of the Shear Layer.
V_t	Tangential Velocity Component.
v	y-Component of Velocity.
W	Complex Potential Function.
z	Nondimensional Location in the Physical Plane. = $x + iy$
z_n	Location of the n^{th} Vortex.
z_t	Tip Coordinate in the Physical Plane.
Δt	Time Increment.
Γ_n	Circulation of the n^{th} Vortex.
2α	Camber Angle.
ε	Radial Incremental Location of the Nascent Vortex.
ζ	Nondimensional Location in the Circle Plane. = $\xi + i\eta$
ζ_t	Coordinate of the Edge of the Camber in the Circle Plane.
ζ_0	Location of the Nascent Vortex in the Circle Plane.
θ	Angular Coordinate Measured Counter-Clockwise.
θ_s	Angular position of the Separation Point.
ν	Kinematic Viscosity (in ft^2/s).
ρ	Density (in slugs/ft^3).

ACKNOWLEDGEMENTS

Foremost, I would like to express my sincere appreciation to Distinguished Professor T. Sarpkaya for his inspiration and guidance throughout the course of this investigation. Professor Sarpkaya's confidence in me often exceeded my self-confidence and enabled me to achieve things I would otherwise have been unable to. I sincerely hope that in the future I will be able to meet the standard of technical competence and personal integrity that Professor Sarpkaya has set. It has been a great honor to study with a man of his professional stature, knowledge, and dedication.

Personnel at the Naval Postgraduate School have assisted me in a variety of ways. In particular, the computer center staff have been most helpful whenever approached with questions. Knowledge and friendship were the gifts given to me by the faculty of the Department of Mechanical Engineering during the past four years. A special note of thanks is extended to Mr. Jack McKay for his most skilful and dedicated work in the construction and smooth operation of the test facilities.

I would like also to thank the Egyptian Ministry of Defense for giving me the opportunity to study at the Naval Postgraduate School.

Finally, I would like to thank my wife Neamat for her love, support and understanding. This thesis is dedicated to her and to the land of Egypt and its people.

I. DISCRETE VORTEX ANALYSIS OF SINUSOIDALLY OSCILLATING FLOW ABOUT CIRCULAR CYLINDERS

A. INTRODUCTION

The separated steady and unsteady flows about bluff bodies have been almost completely unyielding to both analysis and numerical simulation for a number of mathematical reasons and fundamental fluid dynamic phenomena. Separation gives rise to the formation of free shear layers which roll up into vortex rings or counter-rotating vortices. They, in turn, interact with each other, with the counter-sign vorticity generated at the base of the body, and with the motion of often unknown separation points. The wake becomes unsteady even for a steady ambient flow and the problem of the determination of the characteristics of the wake becomes coupled to the conditions prevailing upstream of the separation points. Evidently, viscosity modifies radically the inviscid flow, which, in this case, cannot serve even as a first approximation to the actual flow. The boundary layer equations are not applicable beyond the separation points and are, therefore, of limited use in bluff-body flow problems.

Fage and Johansen's pioneering experimental work (1928), Gerrard's (1966) vortex formation model, and Roshko's (1954) numerous contributions, followed by a large number of important papers, have provided extremely useful insights into the mechanism of vortex shedding. It became clear that a two-dimensional body immersed in a two-dimensional steady flow does not give rise to a two-dimensional steady wake and only a fraction (about 60% for a circular cylinder) of the original-circulation survives the vortex formation. It also became clear that bluff-body flows exhibiting separation, turbulence, and time-dependence are almost completely unyielding to both analysis and simulation even if the ambient flow is assumed to be time invariant.

Many flows of practical interest are unsteady, i.e., the characteristics of the ambient flow are time-dependent. In the past twenty years or so a large number of theoretical and experimental studies have been carried out. These dealt primarily with unseparated laminar flows, the early stages of impulsively started flow over plates and cylinders (numerical and experimental studies), and oscillating flows with zero or non-zero mean flow (on an infinite flat plate and over a cylinder with streaming flow, all

under laminar flow conditions) for the purpose of studying the effects of flow unsteadiness on the transition mechanism and turbulence development (see e.g. Bradbury et al. 1982). Very little has been attempted either theoretically or experimentally to analyze the wake-boundary-layer interaction in time-dependent flows (i.e., with unsteady ambient flow).

The subject of separated time-dependent flow at large Reynolds numbers is lesser developed but of greater practical importance (particularly to marine related topics) relative to other classical component disciplines of fluid mechanics.

A number of unsteady flow machines and their use in the investigation of unsteady turbulent boundary layers have been reviewed and documented by Carr (1981). These included flat plate, diffuser, pipe, airfoil, and cascade flows. The results have shown that (i) the time-averaged mean velocity profile is almost always the same as the velocity profile that would occur in a steady flow having an equivalent mean external flow velocity; (ii) the turbulent structure in the oscillating flow is not changed from the equivalent steady-state counterpart; and (iii) the unsteady effects are often confined to a thin layer near the wall, while the outer region of the boundary layer is not strongly affected. These conclusions, apparently valid for unsteady turbulent boundary layer flows, are not applicable to unsteady separated, turbulent, bluff-body flows.

The separated unsteady flow situations involving wake return, as in the case of a sinusoidally oscillating flow about a cylinder, or wake retardation, as in the case of a decelerating parachute, are an order of magnitude more complex.

In steady flow the position of the separation points is nearly stationary, except for small excursions of about 3 degrees (on a circular cylinder). Furthermore, the interference between the vortices and the body is confined mostly to the vortex formation region.

For oscillating flows the net effect of the shed vortices is twofold. Firstly, their return to the body dramatically affects the boundary layer, outer flow, pressure distribution, and the generation and survival rate of the new vorticity. Secondly, they not only give rise to additional separation points (during the early stages of the flow reversal) but also strongly affect the motion of the primary separation points. These effects are further compounded by the diffusion and decay of vortices and by the three-dimensional nature of the flow (all of which give rise to cycle-to-cycle variations, numerous flow modes, etc.). The stronger and better correlated the returning vortices,

the sharper and more pronounced the changes are in the pressure distribution on the body and in the integrated quantities such as lift, drag, and inertia coefficients. Nevertheless, the increased correlation does not entirely eliminate the consequences of the stochastic variations in the motion of vortices.

In periodic flow, the mobile separation points (when they are not fixed by sharp edges), undergo large excursions (as much as 120 degrees during a given cycle of oscillating flow over a circular cylinder). This experimental fact renders the treatment of boundary layers on bluff-bodies subjected to periodic wake return extremely difficult, particularly when the state of the boundary layer changes during a given cycle. Furthermore, the classical criterion of separation for steady flow, i.e., the vanishing of skin friction on the body, is no longer valid for unsteady flow. According to the MRS criterion (Moore 1958, Rott 1956, and Sears 1972), it is the simultaneous vanishing of the shear and velocity at a point within the boundary layer that determines the separation point. Furthermore, the time rate of change of circulation is no longer given by $d\Gamma/dt = 0.5U_s^2$ as in steady flow, where U_s is the outer flow velocity at separation, but by $(0.5U_s^2 - U_s c\dot{\theta}_s)$ where $c\dot{\theta}_s$ is the speed of the separation point. It is clear from the foregoing that there is little hope of devising a satisfactory theoretical model before something is understood of the unsteady processes associated with the formation and reversal of the wake, spanwise coherence, the sensitive dependence of the motion of vortices on small changes in the previous conditions and on the nature of transition in oscillating flow about smooth and rough cylinders.

B. NUMERICAL SOLUTION OF THE NAVIER-STOKES EQUATIONS

For steady ambient flow about bluff bodies (mostly cylindrical and airfoils), the numerical studies based on the use of the steady or unsteady form of the Navier-Stokes equations and some suitable spatial and temporal differencing schemes are limited, out of necessity, to relatively low Reynolds numbers (less than about 1,000) (see e.g., Lecoq & Piquet (1984) for a finite difference solution and Gresho et al. (1984) for a finite element solution). The major obstacles to the application of either the finite difference or the finite element methods to higher Reynolds number laminar flow are stability, computation time, treatment of the boundary conditions, and accuracy. Even though many differencing schemes have been developed to overcome the instability problem (Roache 1976), maintaining stability continues to be a problem with increasing Reynolds number. The truncation errors decrease the apparent Reynolds number by introducing an unknown artificial viscosity. Even if the problems

associated with stability and truncation errors were to be resolved, the attempt to obtain solutions of the Navier-Stokes equations at higher Reynolds numbers are limited by a fundamental fluid dynamic phenomenon: the stability of the flow itself. When the flow becomes turbulent either in the wake and or in the boundary layers, one needs a closure model for turbulence to solve the Reynolds equations for a time-dependent, three-dimensional, separated, turbulent flow (even if the ambient flow is smooth and the bluff body is two dimensional). Clearly, the roots of the most serious problem in the solution of the Navier-Stokes equations are buried in the physics of turbulence. The stability and truncation-error problems associated with the differencing schemes may be resolved but the problem of turbulence appears to transcend all efforts.

The numerical solution of unsteady incompressible Navier-Stokes equations in their vorticity-stream-function formulation has been investigated by numerous researchers through the use of various finite-difference techniques. These studies concern mostly the separated flow about circular cylinder and prisms at relatively low Reynolds numbers (see e.g., Davis & Moore 1982).

It appears that the existing numerical methods cannot yet treat the high Reynolds number flows with sufficient accuracy for a number of reasons. The finite difference schemes require a very fine grid, a turbulent model, and a very large computer memory. It seems that the modelling of the turbulent stresses in the wake, particularly in time-dependent flows, will be the major source of difficulty in all future calculations. Whether or not it will ever be practical to apply the finite difference and finite element methods to high Reynolds number flows is unknown. The inherent difficulties are certainly significant enough to warrant exploring other solution methods.

C. VORTEX METHODS

1. Discrete Vortex Analysis

Certain separated time-dependent flows may be simulated through the use of the discrete vortex model (DVM) (see e.g. Chorin 1973; Sarpkaya 1975). The free shear layers which emanate from the sides of the body are represented by an assembly of discrete vortices. It has not yet been proven that a continuous vortex sheet may be so discretized. Thus, attention is given here to large scale vortex structures rather than to small-scale instabilities resulting from the vortex interactions. Furthermore, only the most important features of the method, as it is applied to sinusoidally oscillating flow about a smooth cylinder are described.

The previous attempts to apply the DVM to oscillating flow had either gross simplifications or met with various difficulties. Ward and Dalton (1969) considered only the symmetric flow situation with fixed separation points. Stansby (1977, 1979, 1981) fixed the separation points at ± 90 degrees and used the velocity of the nascent vortex rather than the velocity at the separation point to calculate the vortex strengths. This resulted in significantly less vorticity input and prevented the returning vortices from interacting freely with the boundary layers and separation points. Subsequently, Stansby and Dixon (1983) used a Lagrangian vortex scheme and replaced the body surface by a polygon of line segments. The strengths of the segments of vortex sheet needed to establish the zero-velocity condition on the surface were determined from the inverse of an influence matrix and the tangential velocities just inside the surface. Subsequently, the segments were replaced by one or more point vortices. Stansby's calculations for Keulegan-Carpenter number $K = 10$, ($K = U_m T D$), failed to predict the transverse vortex street observed experimentally.

Sawaragi and Nakamura (1979) determined the separation points using Schlichting's (1932) periodic boundary layer theory (valid only for $K \ll 1$). They have not used the Kutta condition and incorrectly included an image vortex at the center of the cylinder. Finally, the calculations were performed for only three-quarters of a cycle, hardly enough time for the transient flow to develop into quasi-steady state. Kudo (1979, 1981) investigated the sinusoidally oscillating flow about a flat plate normal to the flow. The wake was assumed to remain symmetrical. Kudo's model used a Kutta condition, combined with a highly complicated force-and momentum-free nascent vortex placement scheme. Ikeda and Himeno (1981) studied the oscillating flow about a cylinder and a Lewis form. Separation points were assumed to be given by Schlichting's (1932) solution. As with Sawaragi and Nakamura (1979), they have incorrectly retained the image vortices at the center of the cylinder.

The discrete vortex model, as used in the present investigation, is relatively free from the arbitrary assumptions and inconsistencies noted above. However, the inclusion of the effect of turbulence in the boundary layers and in the wake remains unresolved. As it will be noted shortly, the determination of the separation points requires the use of a separation criteria based on a laminar or turbulent flow separation.

2. Formulation of the Problem

The complex velocity potential may be written as

$$W(z) = -U(t) \left(z + \frac{1}{z} \right) + \frac{1}{2\pi} \sum_{n=1}^m \Gamma_n \left[\text{Ln}(z - z_n) - \text{Ln} \left(z - \frac{1}{\bar{z}_n} \right) \right] \quad (1.1)$$

where $U(t) = \sin(2\pi t/T)$, Γ_n and z_n are the strength and position of the n -th vortex. The velocities are normalized by U_m and the distances by c . The complex velocity is given by $dW/dz = -u + iv$.

The instantaneous force acting on the cylinder may be calculated either through the integration of pressure or through the use of the rate of change of impulse. It is relatively easy to show that the pressure on the cylinder is given by

$$P(z) = -2\rho \frac{\partial U(t)}{\partial t} \cos\theta - \rho \mathcal{R} \left(\frac{i}{2\pi} \sum_{n=1}^m \Gamma_n \left(\frac{\dot{z}_n}{z - z_n} + \frac{\dot{\bar{z}}_n}{(z\bar{z}_n - 1)\bar{z}_n} \right) - \frac{1}{2} \rho q^2(z) \right) \Bigg|_{z = r e^{i\theta}} \quad (1.2)$$

In terms of dimensional quantities, the use of the rate of change of impulse yields,

$$D + iL = i\rho \frac{\partial}{\partial t} \sum_{n=1}^m \Gamma_n \left(z_n - \frac{1}{\bar{z}_n} \right) + 2\pi\rho c^2 \dot{U} \quad (1.3)$$

where D and L represent, respectively, the in-line and transverse forces.

3. Specific Details of Creation and Convection of the Vortices

The solution procedure employed was as follows:

- (1) The positions of the stagnation points at the upstream and downstream faces of the cylinder are calculated. For this purpose, the points at which the velocity is zero and changes its sign are located, starting from the most recent stagnation points. When the ambient flow reverses its direction (at the beginning of each cycle) the stagnation points switch their positions (the upstream one becomes downstream and vice versa).

- (2) The positions of the primary and secondary separation points are calculated through the use of one of the following methods:
- (a) Pohlhausen's Method: The velocity is calculated at one degree intervals along the cylinder, starting at the stagnation points. Then the positions of the separation points are determined through the use of Pohlhausen's technique (for details see e.g., Schlichting 1932). When the vortices returning to the cylinder cause irregularities in the velocity distribution along the cylinder (because of the disproportionately large influence of some of the point vortices), the Pohlhausen's method fails to predict a separation point. Under these circumstances, the maximum velocity criterion is used.
 - (b) Maximum Velocity Criterion: The velocity distribution is calculated along the cylinder and the position of the maximum absolute velocity on each side of the cylinder is determined. Then the separation points are located at points where the tangential velocity is a certain time-averaged fraction of the maximum velocity. Further details of this fraction will be discussed later.
 - (c) Absolute Maximum Pressure Criterion: When the difference between the primary separation angles calculated at times t_n and t_{n-1} , either through the use of Pohlhausen's technique or through the use of the maximum velocity criterion, is larger than 8 degrees, then the positions of the maximum absolute pressure are used to calculate the separation points. For this purpose, all velocity peaks are calculated through the use of the tangential velocity distribution. Then the maximum velocity at which the maximum absolute pressure occurs is determined. Then the positions of the separation points are calculated using the maximum velocity criterion. In other words, the pressure distribution is used to locate the position of the maximum velocity nearest the true separation point.

The foregoing, relatively time consuming, steps could have been eliminated through the use of a suitable numerical filter so as to remove the secondary oscillations imposed on the velocity distribution by a few point vortices in the vicinity of the cylinder. It was realized that the use of such a filter will not only consume more computer time but will also introduce uncertainties into the calculations. Thus, its use was disregarded.

- (3) The velocity U_s is calculated at each separation point and the ratio U_s/U_{\max} is determined. Then the cumulative average of this ratio is calculated for use in connection with the maximum velocity criterion to determine the position of the separation points whenever the Pohlhausen criterion fails.
- (4) The strength of the primary nascent vortex is calculated from,

$$\Gamma_{op} = (0.5 |U_s| U_s - U_s c \dot{\theta}_s) \cdot \Delta t \quad (1.4)$$

where $U_s c \dot{\theta}_s$ accounts for the motion of the separation point relative to the flow velocity prevailing at the separation point. The strength of the secondary vortex is calculated from,

$$\Gamma_{os} = 0.5 |U_s| U_s \cdot \Delta t \quad (1.5)$$

In other words, the effect of the relative motion of the secondary separation point on Γ_o is ignored.

- (5) The nascent vortices are placed at a distance ϵ along the radial lines passing through the separation points, i.e., at $z_n = (1 + \epsilon) \exp(i \theta_s)$. The value of ϵ which satisfies the Kutta condition is given by (see e.g., Sarpkaya & Shoaff 1979)

$$\epsilon = \frac{1 + (|\Gamma_o| / 2 \pi U_s)}{1 - (|\Gamma_o| / 2 \pi U_s)} - 1 \quad (1.6)$$

- (6) The velocity at any point $r < r^*$ is calculated using the exact solution of the Navier-Stokes equations for a single rectilinear viscous vortex (Lamb 1932), i.e., $-u + iv = (\Gamma / 2\pi r) [1 - \exp(-r^2 / 4\nu t)] e^{-i\theta}$ and at any point $r > r^*$ using the point vortex relation ($-u - iv = d w / dz$). The radius r is measured from the center of the vortex and θ is taken plus in the CCW direction from the x axis. The core radius r^* at which the tangential velocity is maximum is given by $r^* = \sqrt{1.26 \nu t}$ where t is the age of the vortex since its inception. Then the vortices are convected through the use of a simple Eulerian scheme for a time interval $\Delta t = 0.125 c U_m T$

- (7) The vortices which come closer than a distance of $0.05c$ to the cylinder surface as well as those which have a strength smaller than 0.005 are removed from the field.
- (8) Oppositely signed vortices are combined when their separation distance is less than 0.1 . Furthermore, the secondary vortices are combined at suitable intervals with the primary vortices to reduce the number of the vortices and hence the computation time.
- (9) The pressure and tangential velocity distributions and the force acting on the cylinder (both through the integration of pressure and the rate of change of impulse, given by Eq. (1.3)) are calculated.
- (10) At the end of the foregoing calculations, plots of the vortex positions, tangential velocity, total pressure, and stagnation and separation points are produced.

Two additional details of the model need to be described: The introduction of asymmetry and the circulation dissipation. Any flow started impulsively from rest remains symmetrical (at least in its numerical simulations) if not disturbed for a short time period at or near the beginning of its inception. Sarpkaya and Shoaff (1979) have investigated the methods of asymmetry introduction and found that the displacement of the vortices in one shear layer for a short time interval is much more suitable than any of the methods previously used. In the present calculations, a similar method was used. The only difference was that asymmetry was introduced during roughly the first quarter cycle of flow ($0.1 < t/T < 0.3$) in order to allow the asymmetry to take effect in a reasonable time period.

The previous investigations by Sarpkaya & Shoaff (1979) and others (e.g., Kiya & Arie 1977) have shown that the incorporation of dissipation into a discrete vortex model resulted in a reduction of lift and drag force magnitudes, but did not significantly affect the flow kinematics. In the present work, sample calculations with or without dissipation have shown also that the results differ only in the magnitude of the force coefficients and that the kinematics of the flow is not affected by dissipation. It is in view of this fact that in the results presented herein it was decided to avoid a relatively subjective dissipation mechanism.

4. Discussion of Results

The numerical calculations were carried out for a Keulegan-Carpenter number of $K = 10$. This value of K was chosen primarily because of the fact that some of the

most important phenomena take place in the range $8 < K < 15$ (Sarpkaya 1985; Bearman 1985; Williamson 1985). The most important of these phenomena is the occurrence of a transverse half Karman vortex street on one side of the cylinder.

A series of flow visualization experiments at $K = 10$ was conducted in a water table. Figures 1.1 and 1.2 show a time sequence from a representative run. In these experiments the cylinder ($D = 1.5$ inches) was oscillated in the water table using a period of $T = 3$ seconds ($Re = 12,800$ and $Re:K = \beta = 1280$). The end of the plexiglass cylinder was within 1/16 inch of the bottom of the water table, so that the end effects were minimal. It can be seen that the vortex shedding is indeed on the same side (i.e., left) of the cylinder. The numerical simulation of this phenomenon through the use of the discrete vortex model became a challenge to numerous workers (Sawaragi & Nakamura 1979; Ikeda & Himeno 1981; Stansby 1977, 1979, 1981; and Stansby & Dixon 1982, 1983). However, none of these investigators has been able to simulate the half Karman vortex street for a number of reasons described in the Introduction. The present simulation has removed the shortcomings of the previous analyses, discovered physically and theoretically realistic methods to deal with the separation points, eliminated the ad-hoc assumptions, and produced the results presented herein.

Figures 1.3 through 1.7 show, at times $T^* = t/T = 0.2, 0.4875, 0.6063, 0.7625,$ and 0.8625 the position of the discrete vortices, the tangential velocity distribution and the total pressure distribution. The arrow in each circle shows the direction and the magnitude of the ambient velocity. The vortices of opposite circulation are shown with different symbols. These figures will be used to familiarize the reader with the essential elements of the analysis. Subsequently, the evolution of the transverse vortex street, characteristics of the shear layers, and the normalized drag and lift forces will be presented.

As the ambient velocity starts from rest and nears its maximum value (Fig. 1.3), the vortices grow nearly symmetrically on the downstream side of the cylinder, reminiscent of an impulsively started flow about a cylinder. This is a consequence of the spiralling of the primary shear layers (SL-1 and SL-2), emanating from the primary separation points (SP-1 and SP-2). The primary vortices give rise to secondary boundary layers on the downstream side of the cylinder. These, in turn, separate and give rise to two additional shear layers (called the secondary shear layers, denoted by SL-3 and SL-4). As time increases and the ambient velocity decreases (Fig. 1.4), the

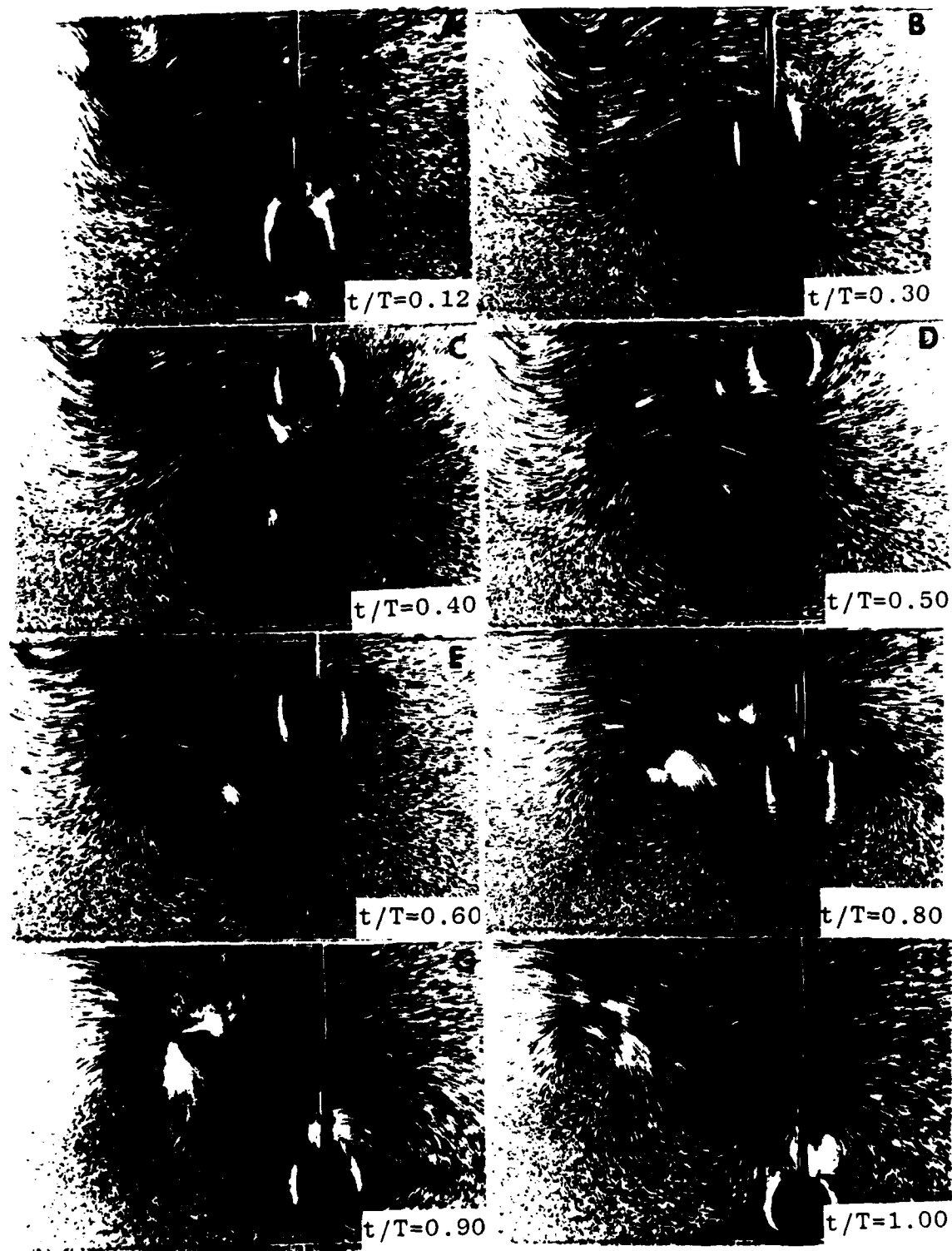


Figure 1.1 Time sequence from flow visualization experiments ($0.12 < T^* < 1.00$).

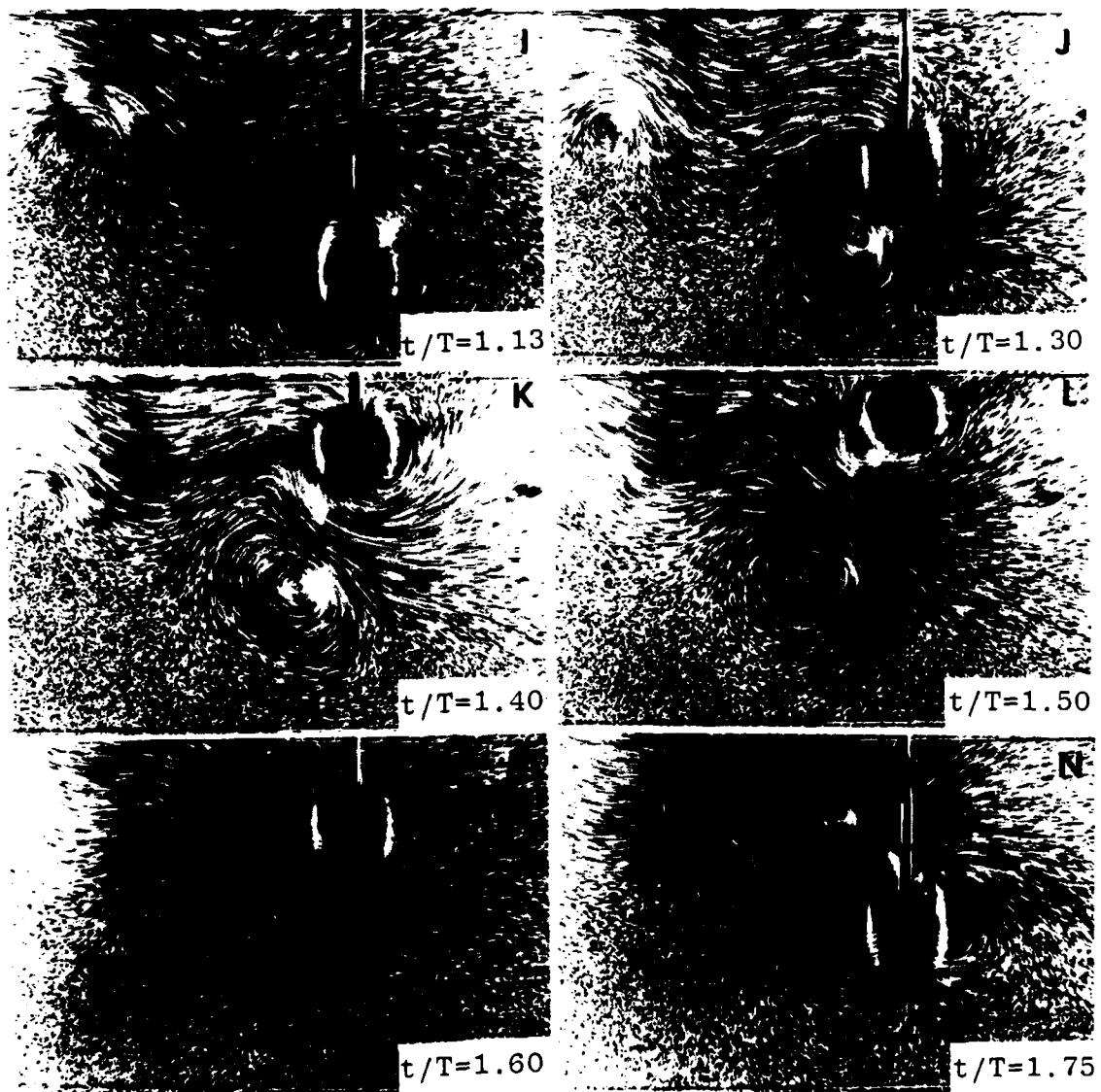


Figure 1.2 Time sequence from flow visualization experiments ($1.13 < T^* < 1.75$).

first vortex sheds from the upper right hand side of the cylinder. This leads to the rapid growth of the vortex in the lower right hand side. The tangential velocity around the cylinder is now primarily due to that induced by the vortices. The spikes in the velocity and pressure distributions are a consequence of the disproportionately large influence of a few vortices in the vicinity of the cylinder. They are most prevalent at times of very small ambient velocity.

For $T^* > 0.5$, the ambient flow reverses its direction, the flow separates on the left side of the cylinder, and the previously shed vortices are convected towards left (Figs. 1.5 and 1.6) partly due to the ambient flow and partly due to the mutual induction of all the vortices and their images. The reversal of the flow has two major consequences. First, the convection of the previously shed vortex over the shoulder of the cylinder precipitates earlier separation and establishes, by its sense of rotation, a preferred position for the next dominant vortex. Second, the reversal of flow gives rise to additional primary and secondary separation points (Fig. 1.6). However, at a given time there are at most four shear layers, i.e., some of the separation points disappear and some new ones come into existence as the flow reverses. Subsequently, the vortical structure at the upper left side of the cylinder moves further downstream and the vortex on the lower left side of the cylinder (Fig. 1.7) grows rapidly (in a manner similar to that shown in Fig. 1.4). It begins to move towards the top of the cylinder, partly due to the mutual induction velocity of the aforementioned vortical structure and partly due to that of its image. The events just described more or less repeat themselves in the subsequent cycles (see Figs. A.1 through A.17 in Appendix A). More or less, because no two cycles can be expected to be exactly alike due to the ever increasing number of vortices or, in other words, due to the transient nature of the flow (for an experimental confirmation of this fact see Sarpkaya 1986). Many more cycles of calculations will have to be carried out in order to reach a quasi-periodic state. However, this is nearly impossible and hardly necessary, partly because of the computer-time limitations and partly because the calculations over a period of three cycles are more than sufficient to delineate the fundamental characteristics of the flow. The reason for the latter is provided by the mechanism of vortex shedding during each half cycle of flow. As noted in the course of the discussion of Figs. 1.3 through 1.7, the flow in each half cycle behaves as if it started more or less anew, the single convected vortex over the shoulder of the cylinder precipitating earlier separation and dictating the side from which the next dominant vortex is to be shed. In numerical

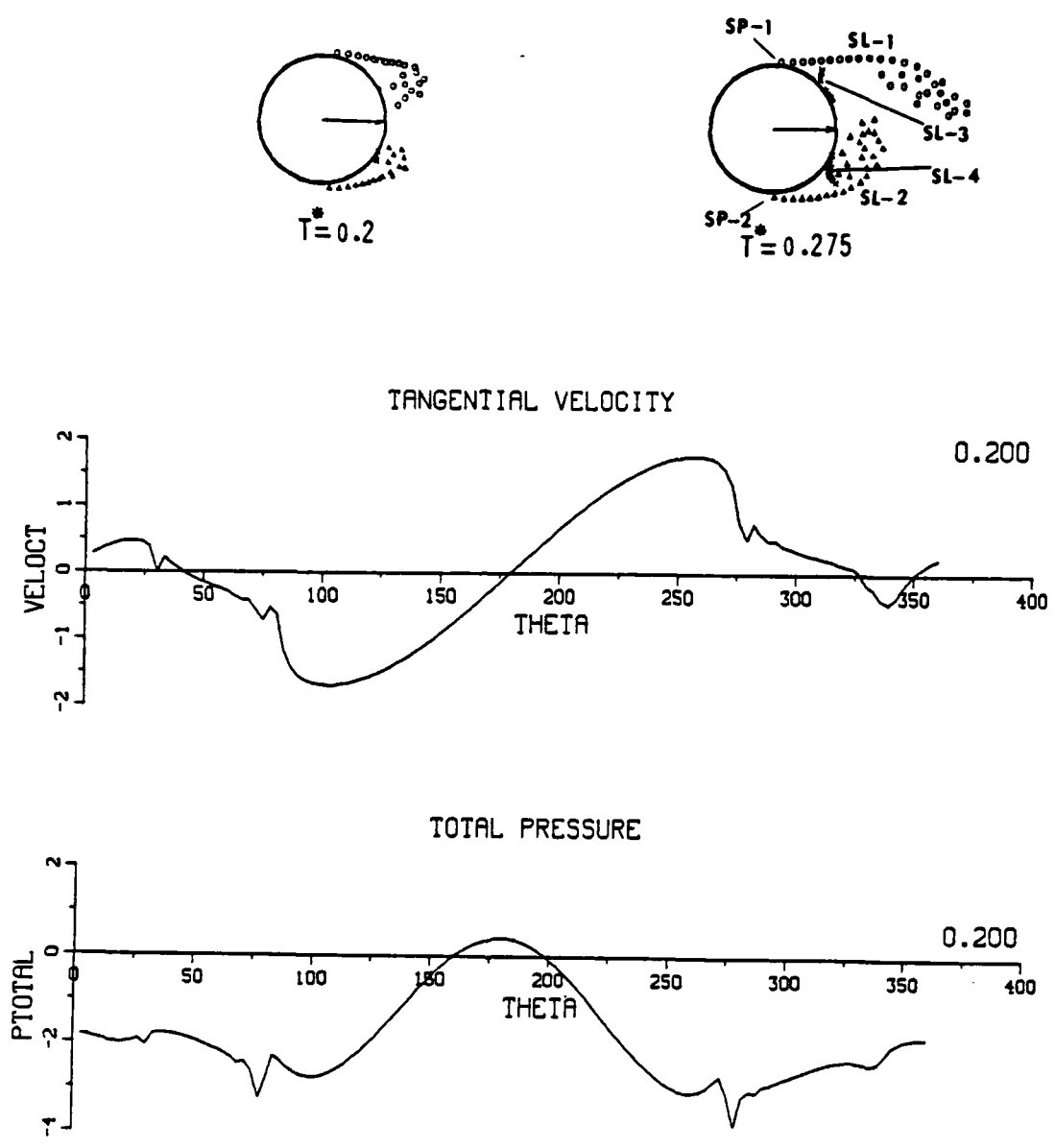


Figure 1.3 Position of vortices, velocity and pressure distributions at $T^* = 0.200$.

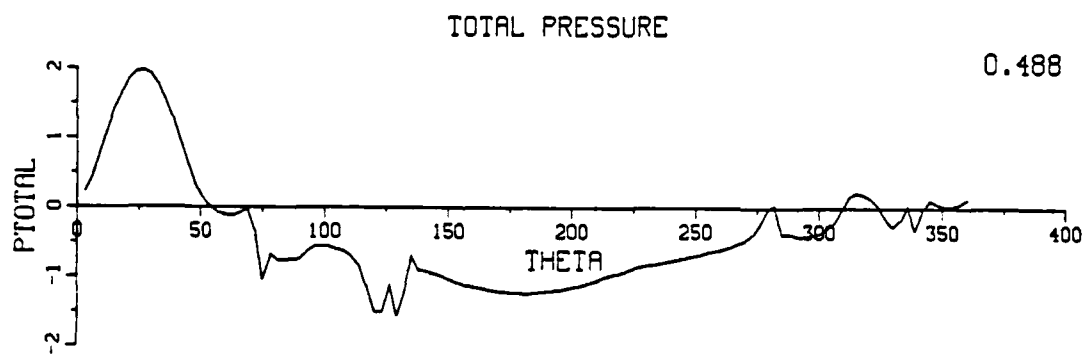
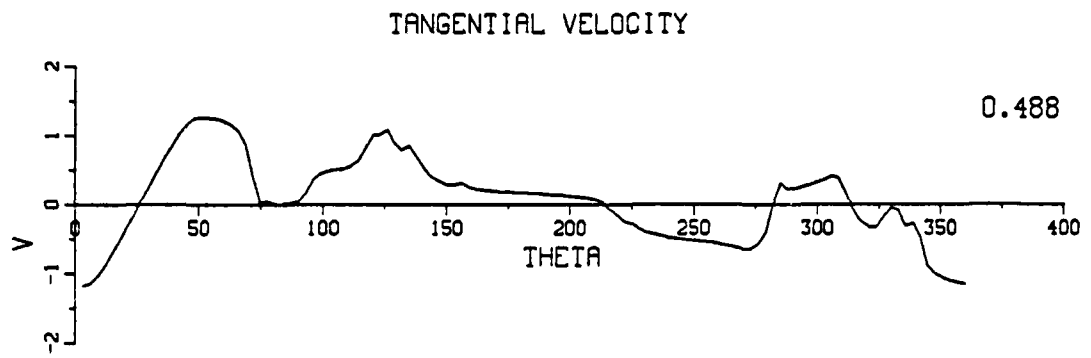
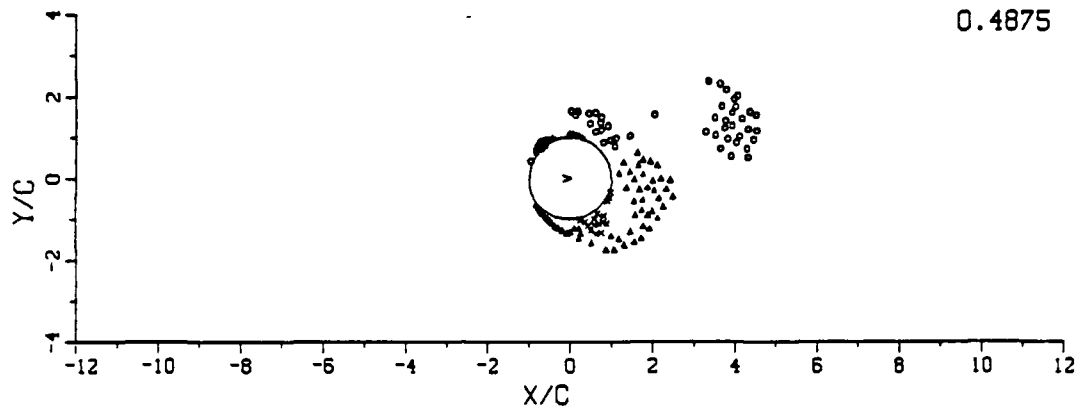


Figure 1.4 Position of vortices, velocity and pressure distributions at $T^* = 0.4875$.

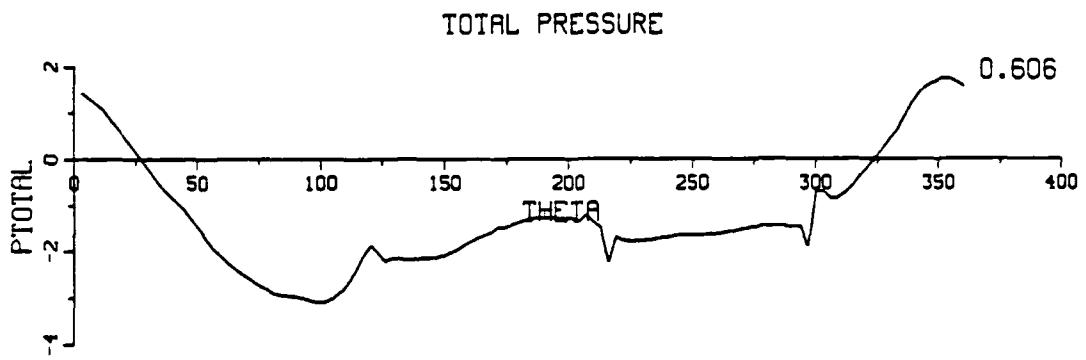
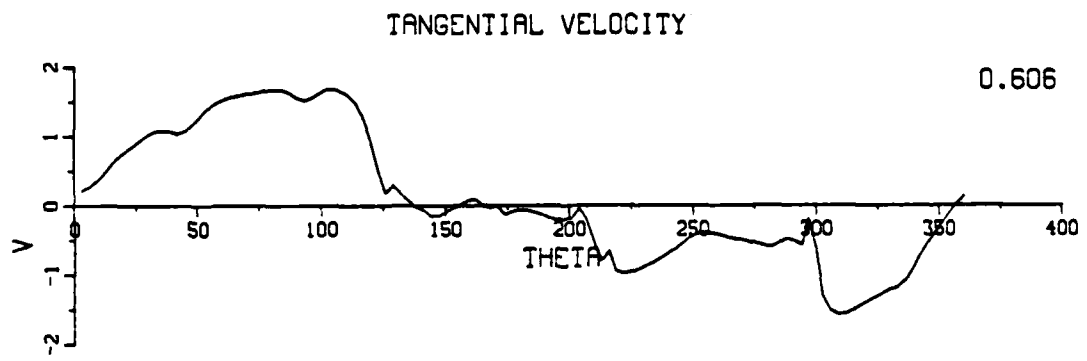
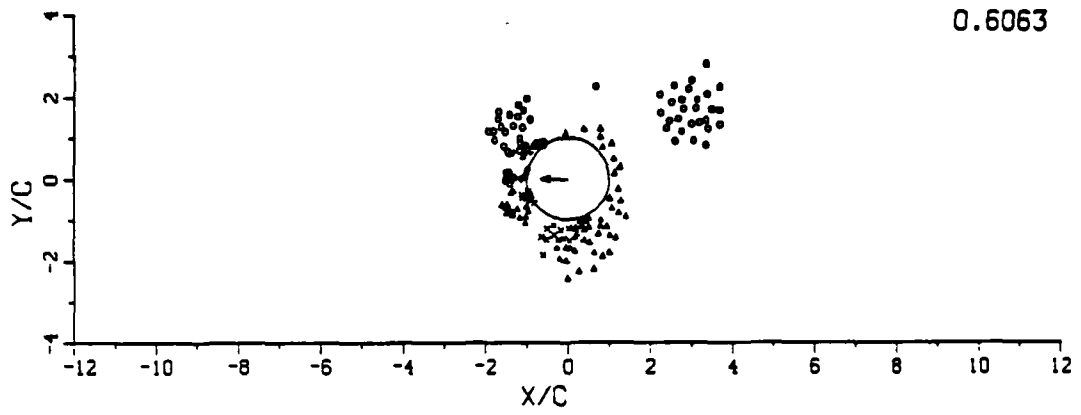


Figure 1.5 Position of vortices, velocity and pressure distributions at $T^* = 0.6063$.

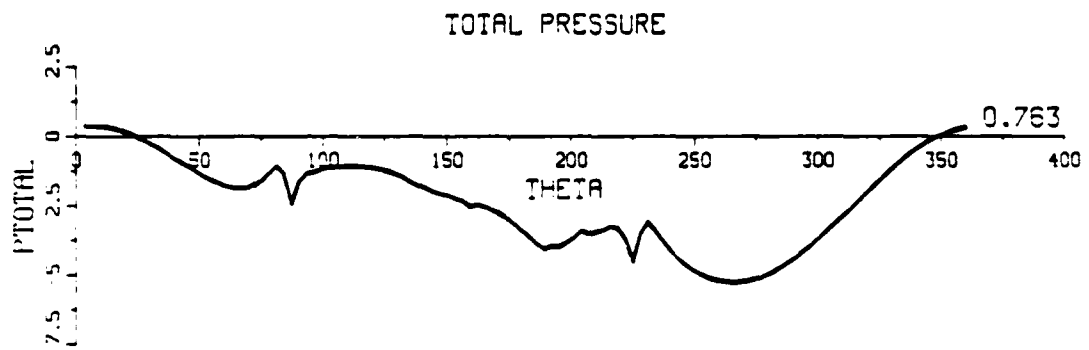
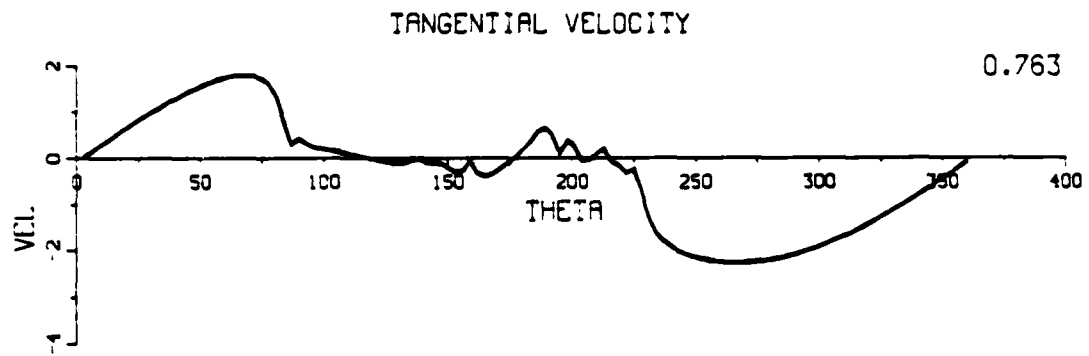
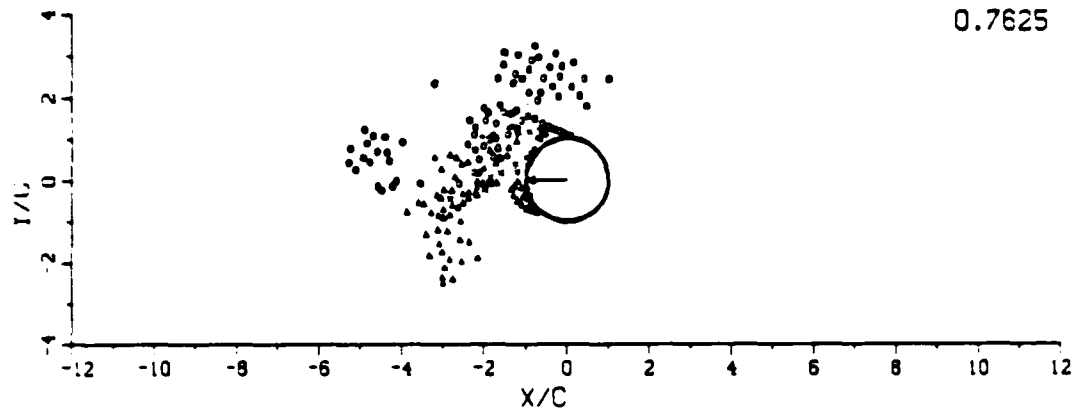


Figure 1.6 Position of vortices, velocity and pressure distributions at $T^* = 0.7625$.

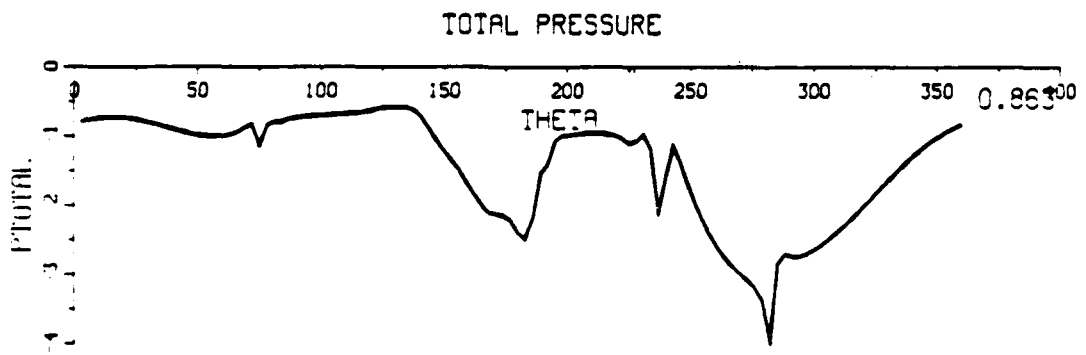
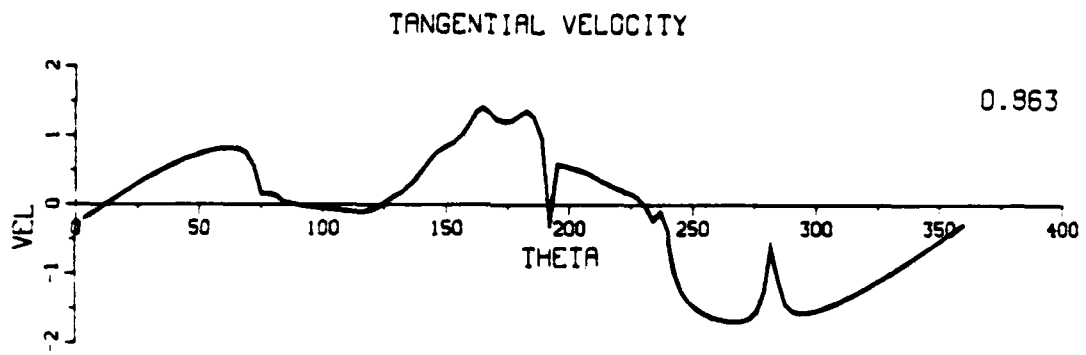
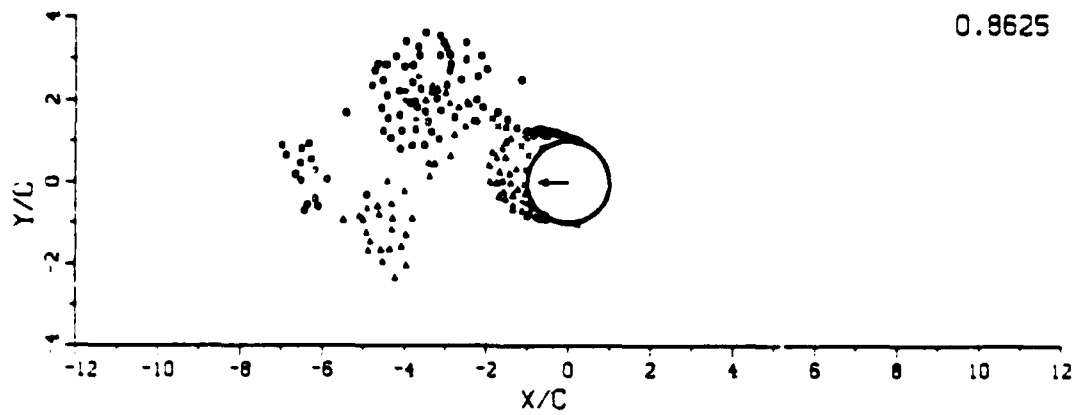


Figure 1.7 Position of vortices, velocity and pressure distributions at $T^* = 0.8625$.

calculations the vortices do not dissipate and, therefore, begin to cover the entire flow field. The real vortices decay rapidly under the influence of viscosity (no vortex in the far field survives more than a few cycles). The purpose of the numerical calculations was not to simulate the effects of viscosity but rather to show that the behavior of flow (e.g., the evolution of the transverse vortex street) is primarily an inviscid phenomenon, dependent on the relative amplitude of the flow or the Keulegan-Carpenter number. The results show that the effect of viscosity is important in bringing about the separation and in decaying the vortices but not in bringing about the particular vortical structure.

The vortex motion about the cylinder is better illustrated through the use of the vector plots of the velocity field. Figures 1.8 through 1.20 show the velocity field at suitable time intervals over one and one-half cycles, starting at $T^* = 0.5$. At the end of the first half cycle (Fig. 1.8), two large vortices are separated by a strong current between them. As the flow reverses (Fig. 1.9) and the ambient velocity reaches a value of $U = 0.707$, the vortex adjacent to the cylinder splits into two unequal parts as it moves to the left, partly over the top and partly over the bottom of the cylinder. The vortex to the right of the current in Fig. 1.8 is simply convected towards the left of the cylinder. At $T^* = 0.75$ ($U = 1$), the vortices convected over the top of the cylinder give rise to earlier separation on the upper left side of the cylinder. Furthermore, the new vortex growing on the lower left side of the cylinder is pulled towards the top of the cylinder. Figures 1.11 ($U = 0.707$) and 1.12 ($U = 0$) show the development of two large vortices, again separated by a strong current (compare Figs. 1.8 and 1.12). Figure 1.13 ($U = 0.707$) shows that the vortex adjacent to the left side of the cylinder remains nearly intact and is convected towards right over the top of the cylinder. Figures 1.14 ($T^* = 1.25$, $U = 1$) and 1.14 ($T^* = 1.375$, $U = 0.707$), show that the separation of flow on the right side of the cylinder gives rise to new vortices, in a manner similar to that shown in Fig. 1.10. Subsequently, this leads to two large vortices (Fig. 1.16), separated by a current as in Fig. 1.8. Evidently, Figs. 1.8 and 1.16 are not expected to be identical in an ever evolving unsteady flow. Nevertheless, the essential features of the two flows (separated by a full cycle) are quite comparable. The secondary vortical structures seen in Fig. 1.16 are a consequence of the inviscid nature of the calculations. As noted earlier, they do not survive the effects of viscosity and turbulence in physical experiments. Figures 1.17 through 1.20 show the evolution of the flow for an additional half cycle. Clearly, the flow pattern repeats itself with minor differences (compare Figs. 1.8 and 1.16 and Figs. 1.12 and 1.20).

It is evident from the foregoing that the reason for the occurrence of the transverse vortex street in the range $8 < K < 13$ (corresponding to the amplitude-to-diameter ratios of $A/D = 1.27$ to 2) is, as expected, the formation of two asymmetric vortices during a given half cycle and the effect of the returning vortices on the formation of the new vortices.

The vortical structures and the transverse current shown in Figs. 1.8 through 1.20 cannot be directly compared at an arbitrary time T^* with those shown in Fig. 1.1 since the streaklines of an oscillating flow about a stationary cylinder are not the same as those of an oscillating cylinder in a fluid otherwise at rest. Nevertheless, a comparison of Figs. 1.1D and 1.1L with Figs. 1.12 and 1.20 (at times of zero ambient velocity or zero cylinder velocity) has shown that the radial and the angular positions of the vortices are predicted with surprising accuracy. In Figs. 1.1D and 1.1L, the vortex to the left of the current is located at $r/c = 5.45$ and θ (from the vertical) = 17° degrees. The position of the same vortex in Figs. 1.12 and 1.20 is $r/c = 5.42$ and θ (from the x axis) = 15° degrees. It should be noted in passing that the side from which the dominant vortex sheds may become switched by the action of random disturbances in the flow or by stopping and restarting the flow. In the numerical calculations the direction of the transverse flow depends on the side at which the asymmetry is introduced into the flow. Had the asymmetry been introduced on the lower side of the cylinder, the transverse flow would have occurred on the lower side of the cylinder.

The creation, shedding and backward convection of the dominant vortex in a flow field, where there are only a few vortices, strongly affect the pressure distribution about the cylinder. Thus, it would have been desirable to compare the measured and predicted pressure distributions. However, no such data is available at $K = 10$ or at any other K value. Wilson (1983) measured the differential pressure between two diametrically opposed points on a cylinder and provided differential pressure distributions at suitable times. Calculations have been performed with the numerical model to obtain similar differential pressure data. Figure 1.21 shows two comparisons of the measured and calculated differential pressure distributions. Even though the magnitudes differ somewhat, the general shape of the two C_p curves are remarkably similar. The reason for the difference in their magnitude is directly related to the strength of the vortices. Previous investigations (see e.g., Sarpkaya 1973) have shown that the calculated vortex strengths are somewhat larger than those obtained experimentally. An additional loss of vorticity could have been introduced into the

model in a manner similar to that used by Sarpkaya and Shoaff (1979) in order to bring the strengths of the shed vortices, and thereby the differential pressure distributions, into closer agreement with those obtained experimentally. However, it was decided to avoid a relatively subjective dissipation mechanism. It appears that the kinematics of the flow does not strongly depend on the strength of the shed vortices. This is in conformity with the previous applications of the discrete vortex model (Sarpkaya & Shoaff 1979).

Figures 1.22 and 1.23 show the calculated drag and lift coefficients as a function of time. The effect of the passage of a vortex over the shoulder of the cylinder is exhibited in these figures in two ways. First, it brings sharp changes in C_d near its maximum. Second, it gives rise to a net transverse force on the cylinder. Evidently, the lift force is very sensitive to the flow asymmetry and depends strongly on the proximity to the cylinder of the vortex passing over the cylinder. The calculations will have to be carried out over many more cycles in order to obtain a root-mean-square value of the lift coefficient for comparison with that obtained experimentally. This has not been done in the present study for the reasons cited earlier.

A comparison of the measured and calculated drag force is shown in Fig. 1.24. The agreement is not as good as expected primarily due to the fact that the strength of the calculated vortices is somewhat larger than those encountered in the experiments. A 5 to 10 percent decrease in circulation could have brought the measured and calculated forces into much closer agreement. As noted earlier, however, this was not the purpose of the present investigation.

The attention will now be directed to the motion of the stagnation and separation points and to the vorticity fed into the shear layers. Figures 1.25 and 1.26 show the motion of the upstream (primary) and downstream (secondary) stagnation points, respectively. Here upstream means the side of the cylinder facing the ambient flow. The primary and secondary stagnation points are approximately 180 degrees apart, as would be expected. For example, at $T^* = 0.5$ the primary stagnation point jumps to nearly zero and the secondary stagnation point jumps to approximately 180 degrees. The spurious oscillations in Figs. 1.25 and 1.26, particularly in the position of the secondary stagnation point, are due to the disproportionately large influence of the proximity to the cylinder of a few point vortices.

Figures 1.27 and 1.28 show the motion of the primary and secondary separation points (see also Fig. 1.3). Aside from the spurious secondary oscillations

(due to the reasons cited earlier), Fig. 1.27 shows in general that the primary separation angle increases rapidly as the velocity of the ambient flow increases from zero (e.g., at $T^* = 1$, see Fig. 1.12) to an average value of about 110 degrees at $T^* = 1.5$ (see Fig. 1.16). Then it decreases rapidly to zero as T^* approaches 2 (see Fig. 1.20). A comparison of Figs. 1.27 and 1.28 shows that there is a phase shift of one half of a cycle between the positions of the primary and secondary separation points, as would be expected. There is, at present, no separation point data for comparison with those obtained experimentally.

Finally, Fig. 1.29 shows the vorticity fed into each shear layer. The first and second shear layers have relatively large and oppositely-signed vorticity. They are not each other's mirror image due to the asymmetry of the flow. The vorticity in the third and fourth shear layers is about 25 to 30 percent of that in the primary shear layers. Clearly, the vorticity fed into the primary shear layers (particularly that fed into the first shear layer) has a sinusoidal character to it. This is because the vorticity is related to the ambient flow velocity ($\sin \omega t$) through the velocity U_s at the separation point. The flow variables such as vorticity cannot be measured directly. Thus, the accuracy of its magnitude and time-dependence can only be inferred indirectly through the comparison of the measured and calculated forces and pressure distributions. It appears, on the basis of such comparisons that, the calculated vorticity is about 10 percent larger than that prevailing in physical experiments. The reasons for this are partly the diffusion of vorticity by viscosity and turbulence and partly the three-dimensional nature of the physical experiments.

D. CONCLUDING REMARKS ON OSCILLATING FLOW ABOUT CYLINDERS

The discrete vortex model used in the present investigation avoids many of the problems associated with the Eulerian finite difference and finite element methods but is subject to some of its own. Chief among these is the excessive computer time needed for the calculation of the convection of vortices and the difficulty to account for the effects of viscosity and turbulence.

In the present simulation the discrete vortex model has been combined with the boundary layer calculations and the positions of the separation and stagnation points have been calculated for a Keulegan-Carpenter number of $K = 10$. The results have accurately predicted the formation of a half Karman vortex street in the transverse direction. The calculated positions of the vortices were found to be in good agreement

with those obtained experimentally. The measured and calculated drag force and the differential pressure distributions showed reasonably good agreement. The measured in-line force was somewhat smaller primarily due to the fact that the vorticity fed into the shear layers has not been artificially reduced to bring the measured and calculated forces into closer agreement. The results have also shown that the effect of the backward convection of a large vortex over one side of the cylinder is indeed very pronounced on all the measured and computed characteristics of the flow. This is one of the most important reasons as to why the Morison's equation (see e.g., Sarpkaya & Isaacson 1981) fails to represent the in-line force acting on the cylinder with reasonable accuracy, particularly in the range $8 < K < 13$.

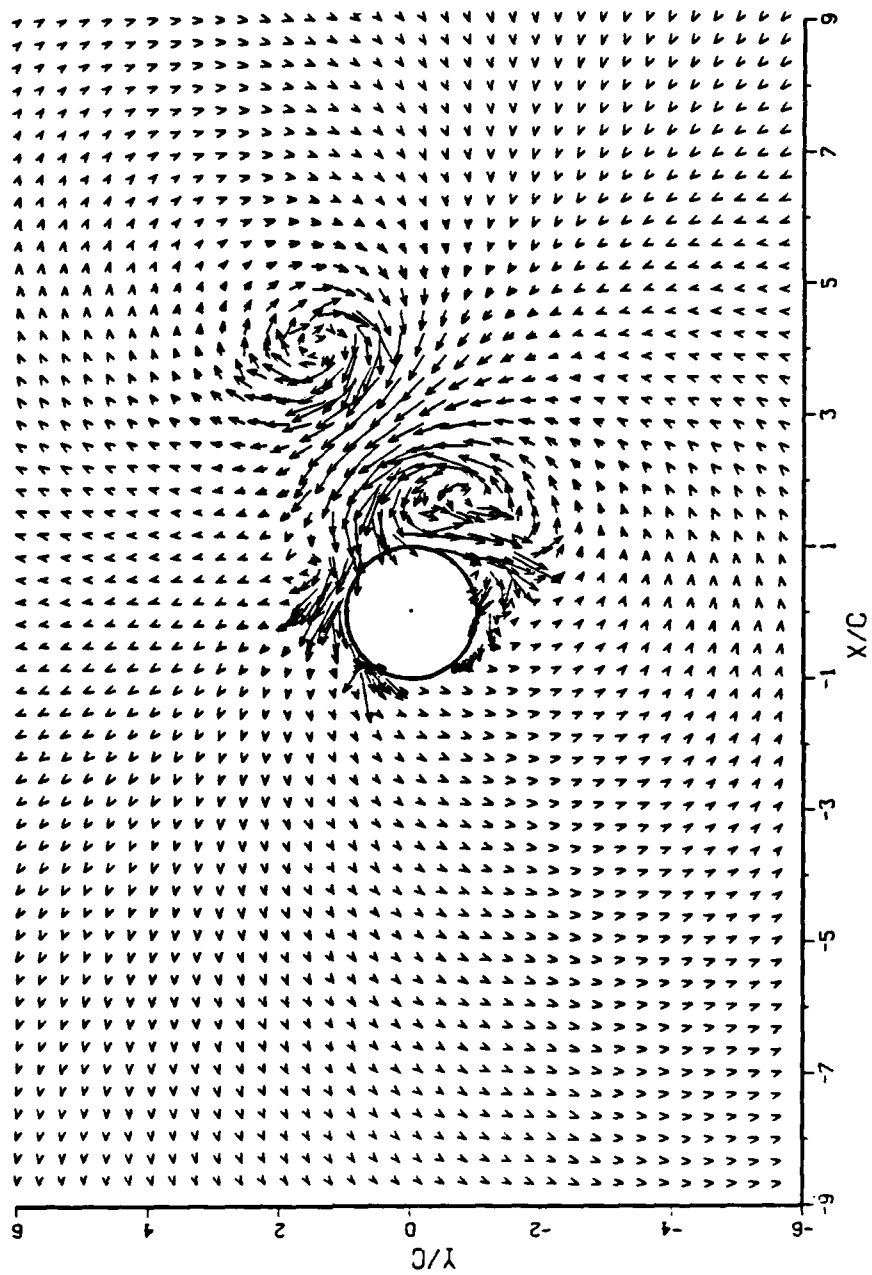


Figure 1.8 Flow field at $T^* = 0.500$.

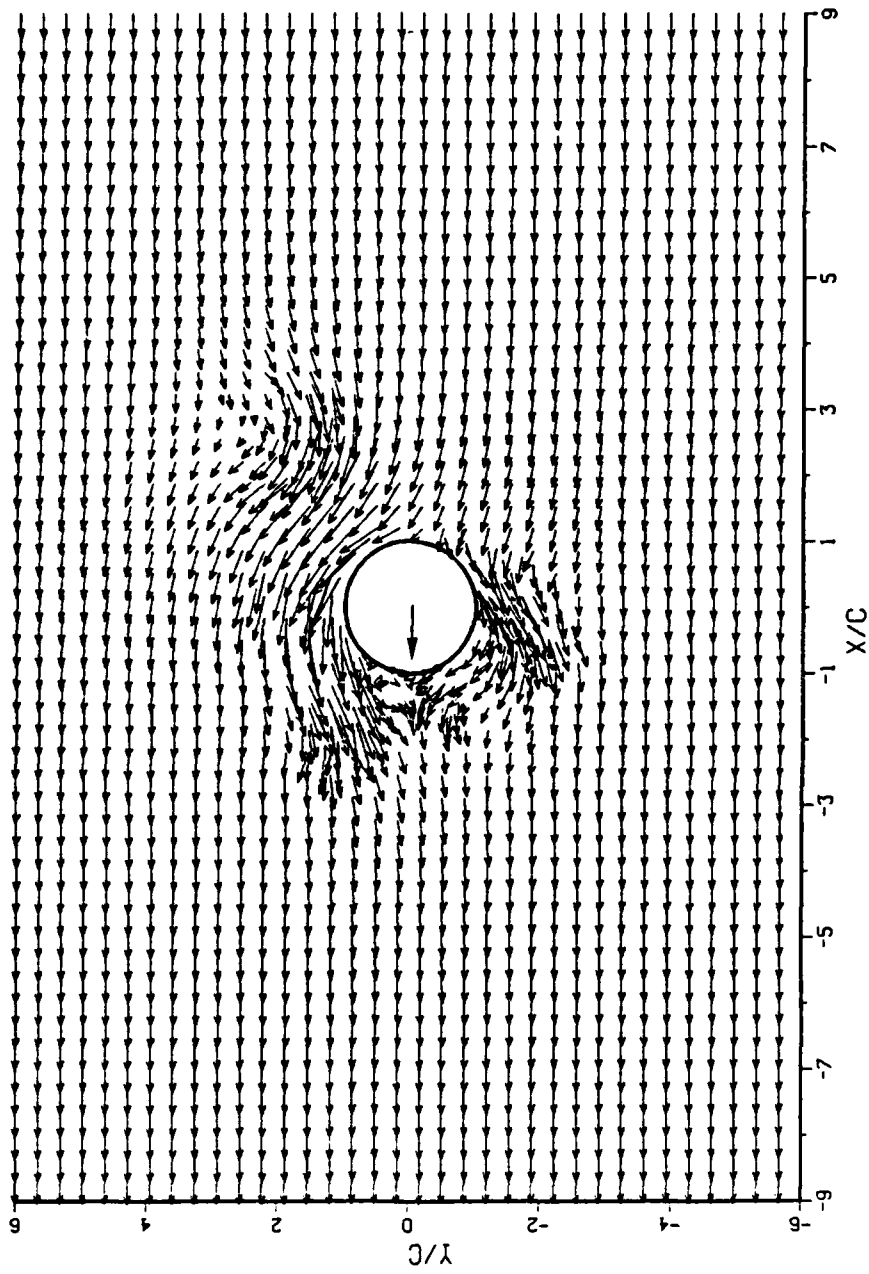


Figure 1.9 Flow field at $T^* = 0.625$.

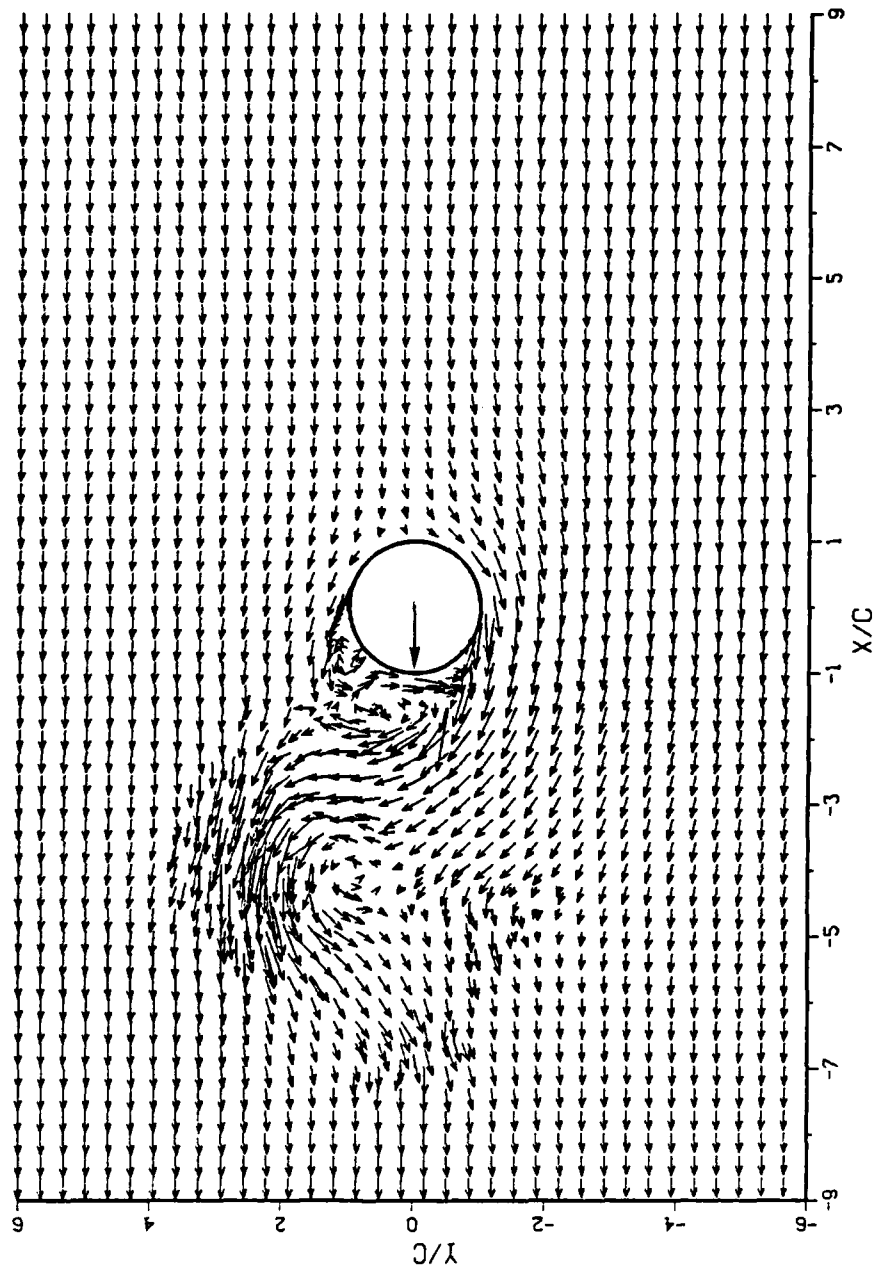


Figure 1.10 Flow field at $T^* = 0.750$.

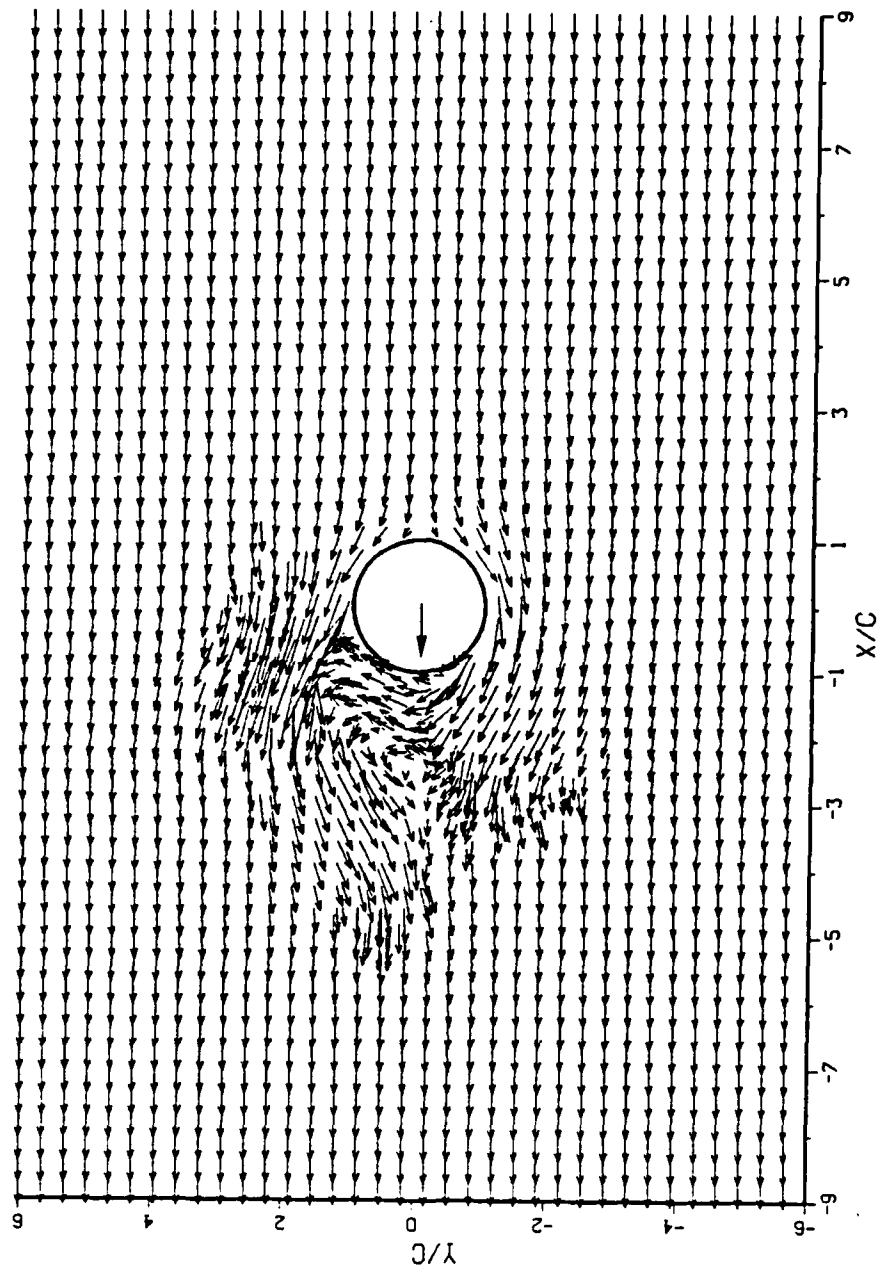


Figure 1.11 Flow field at $T^* = 0.875$.

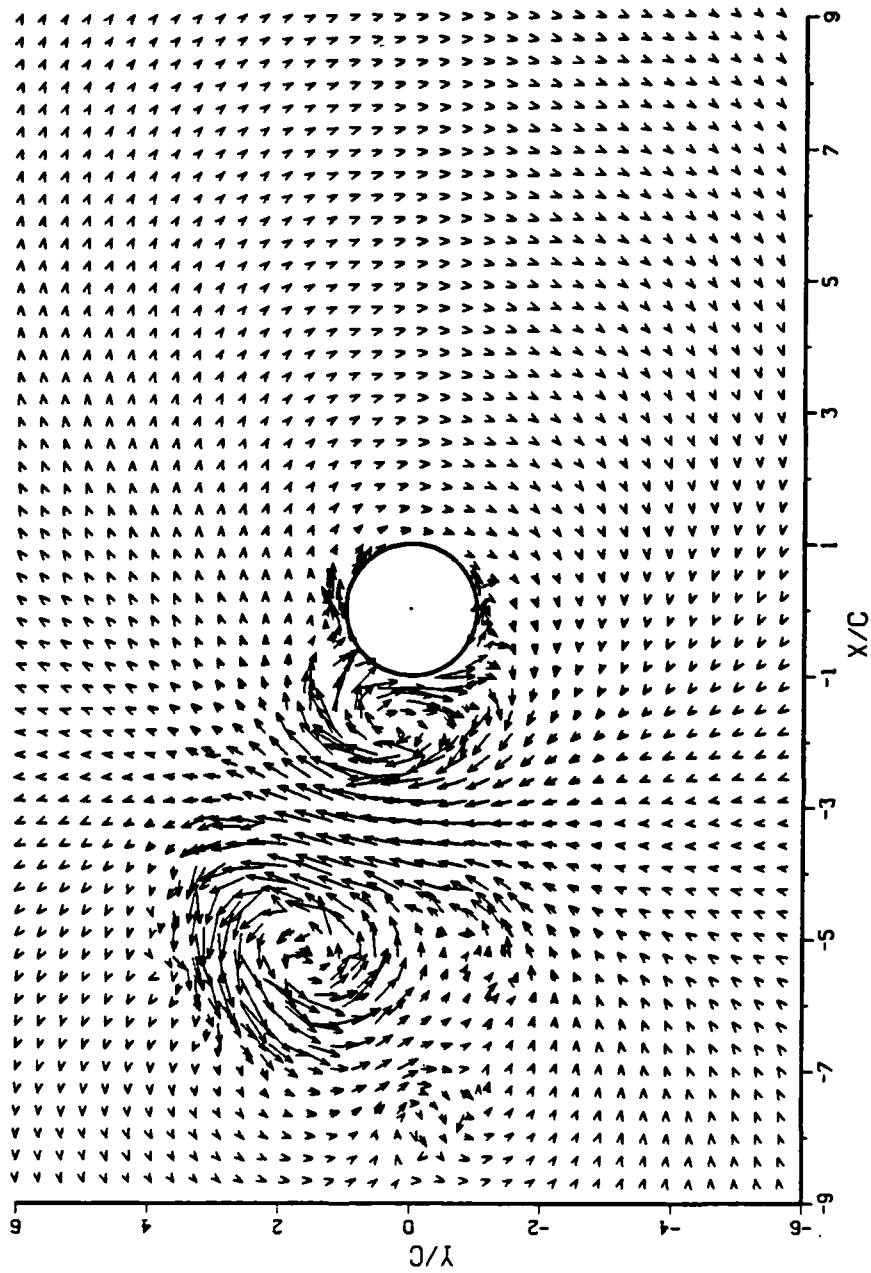


Figure 1.12 Flow field at $T^* = 1.00$.

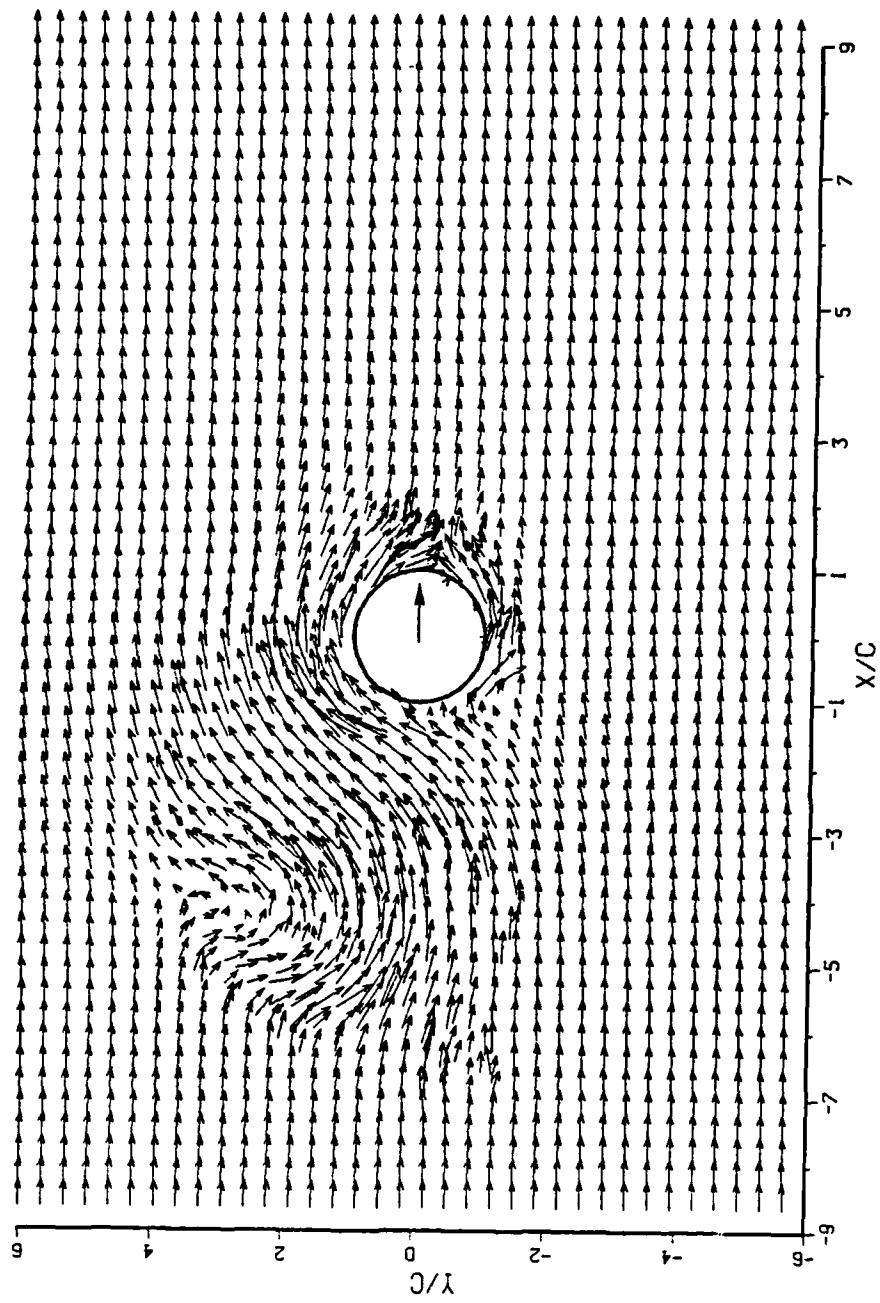


Figure 1.13 Flow field at $T^* = 1.125$.

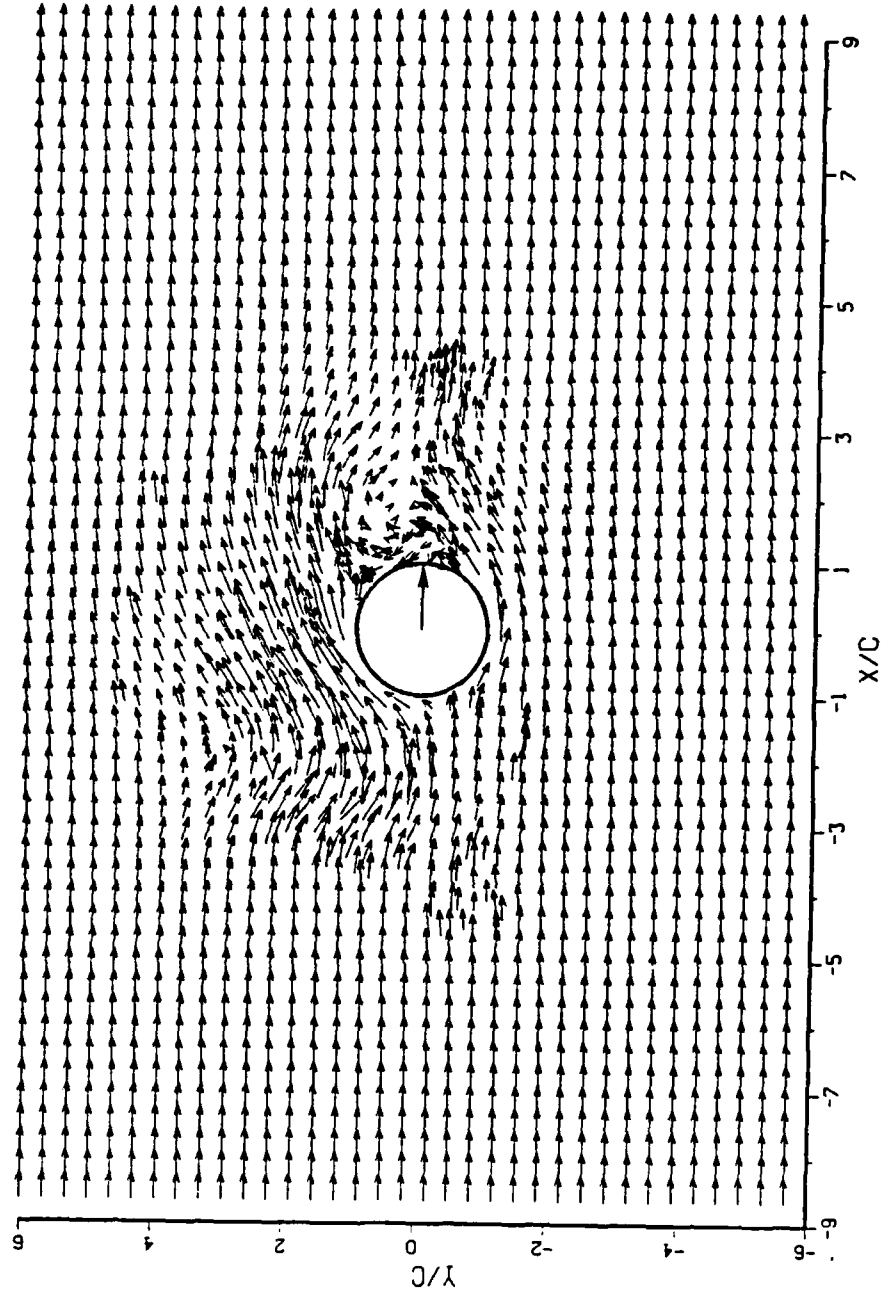


Figure 1.14 Flow field at $T^* = 1.250$.

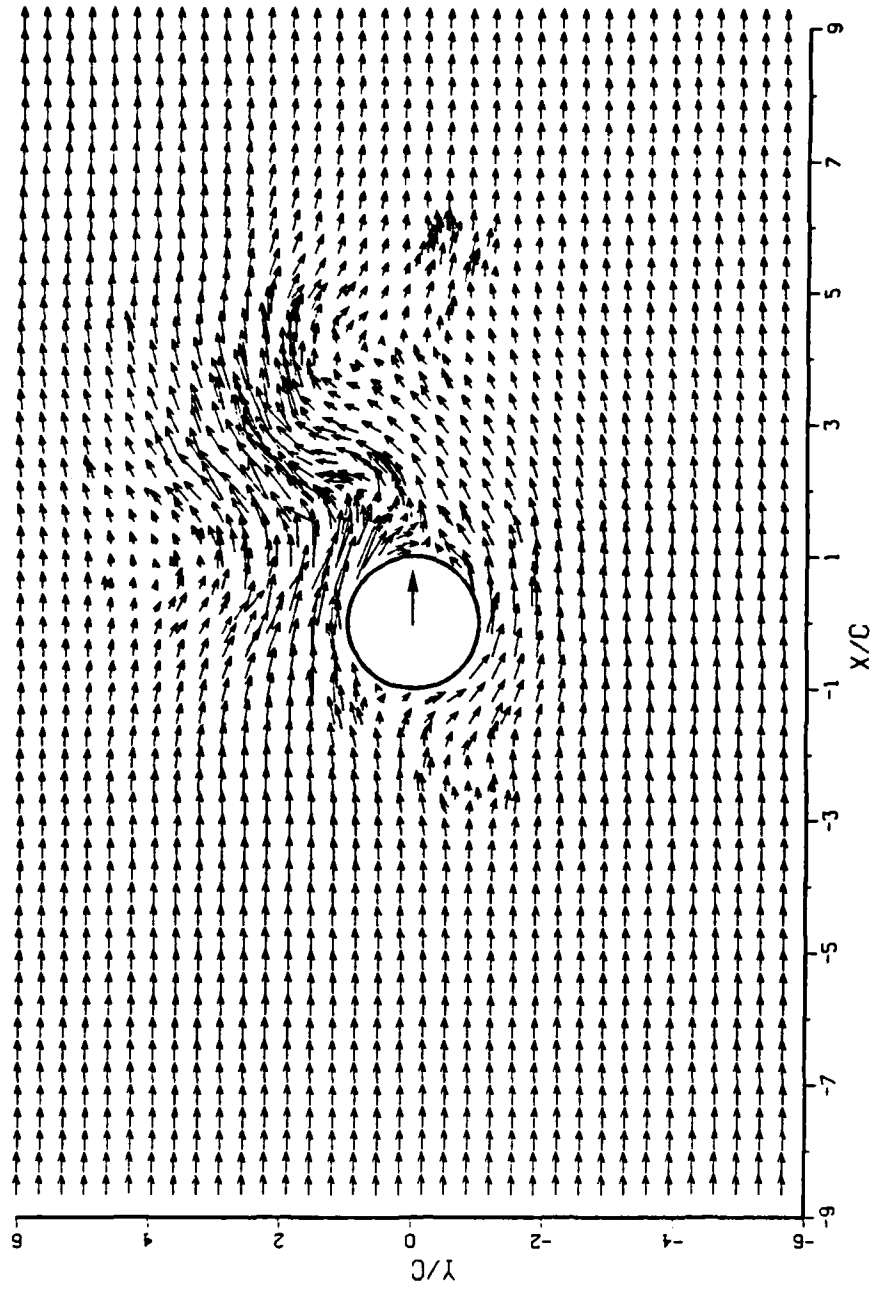


Figure 1.15 Flow field at $T^* = 1.375$.

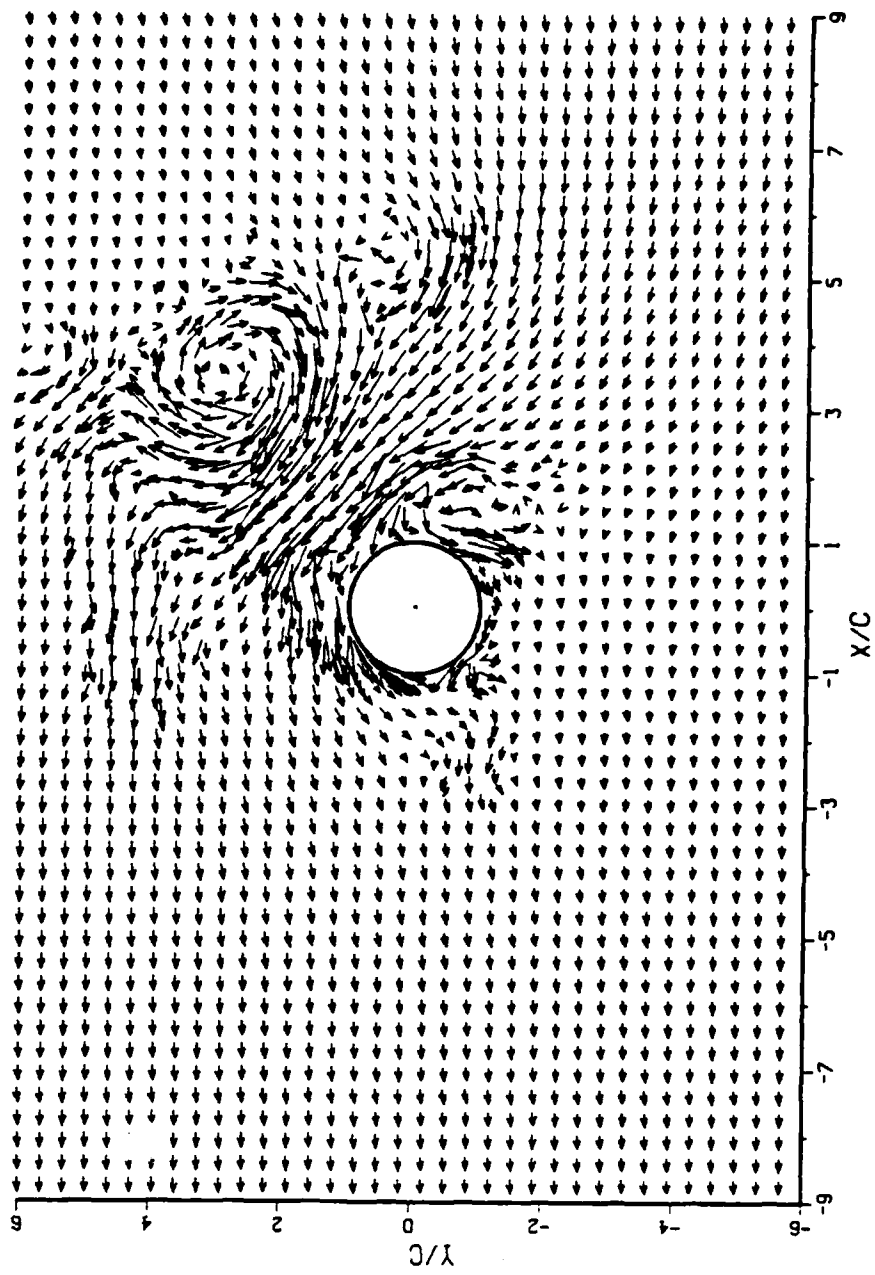


Figure 1.16 Flow field at $T^* = 1.500$.

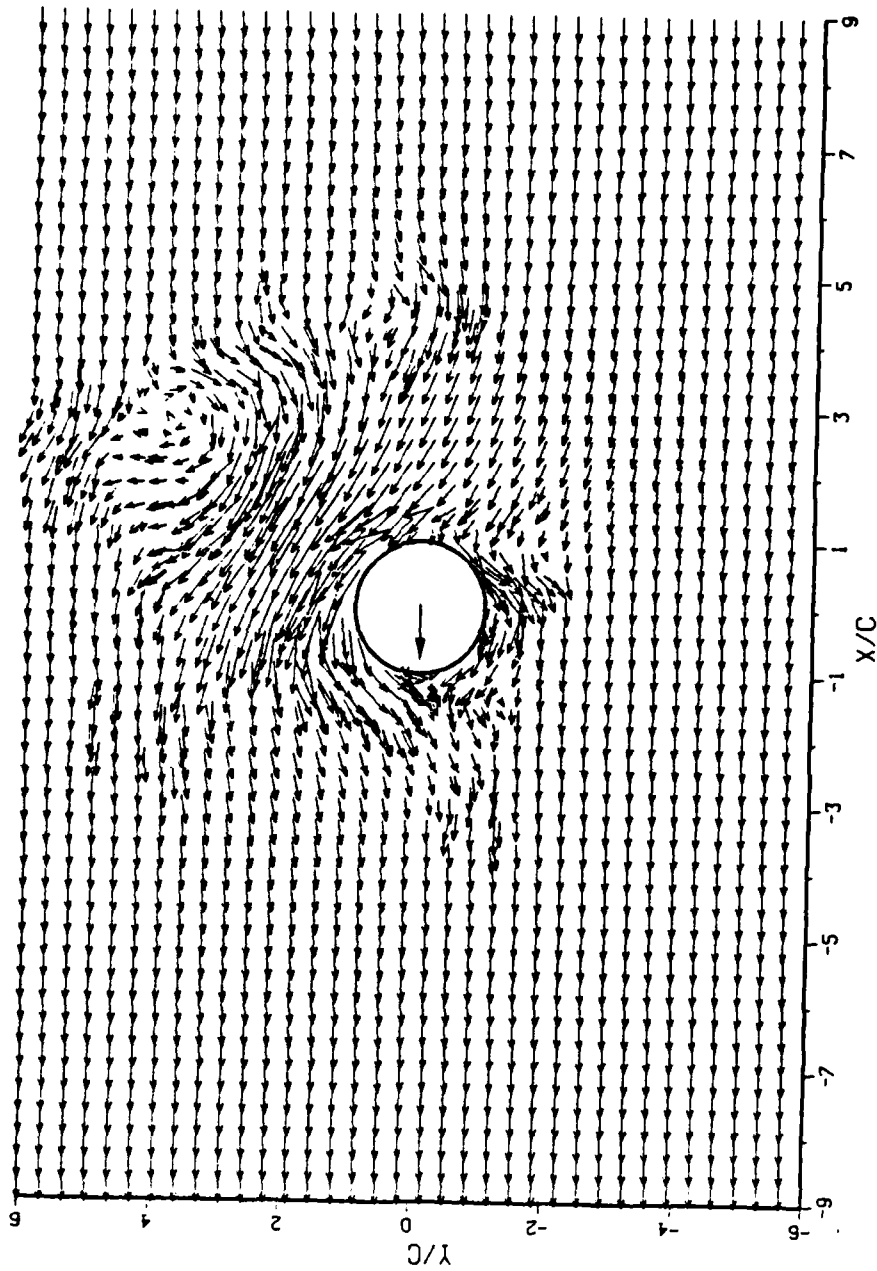


Figure 1.17 Flow field at $T^* = 1.625$.

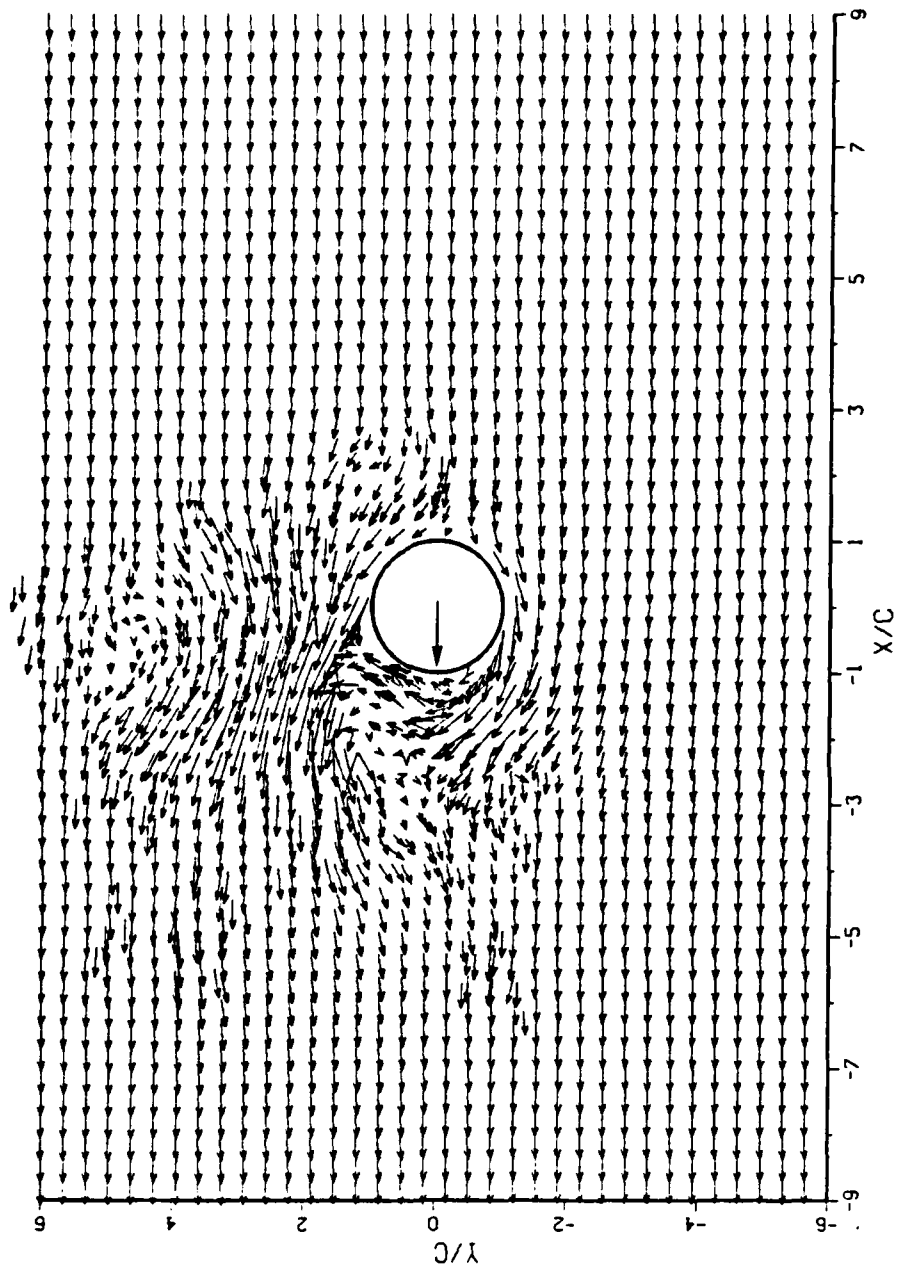


Figure 1.18 Flow field at $T^* = 1.750$.

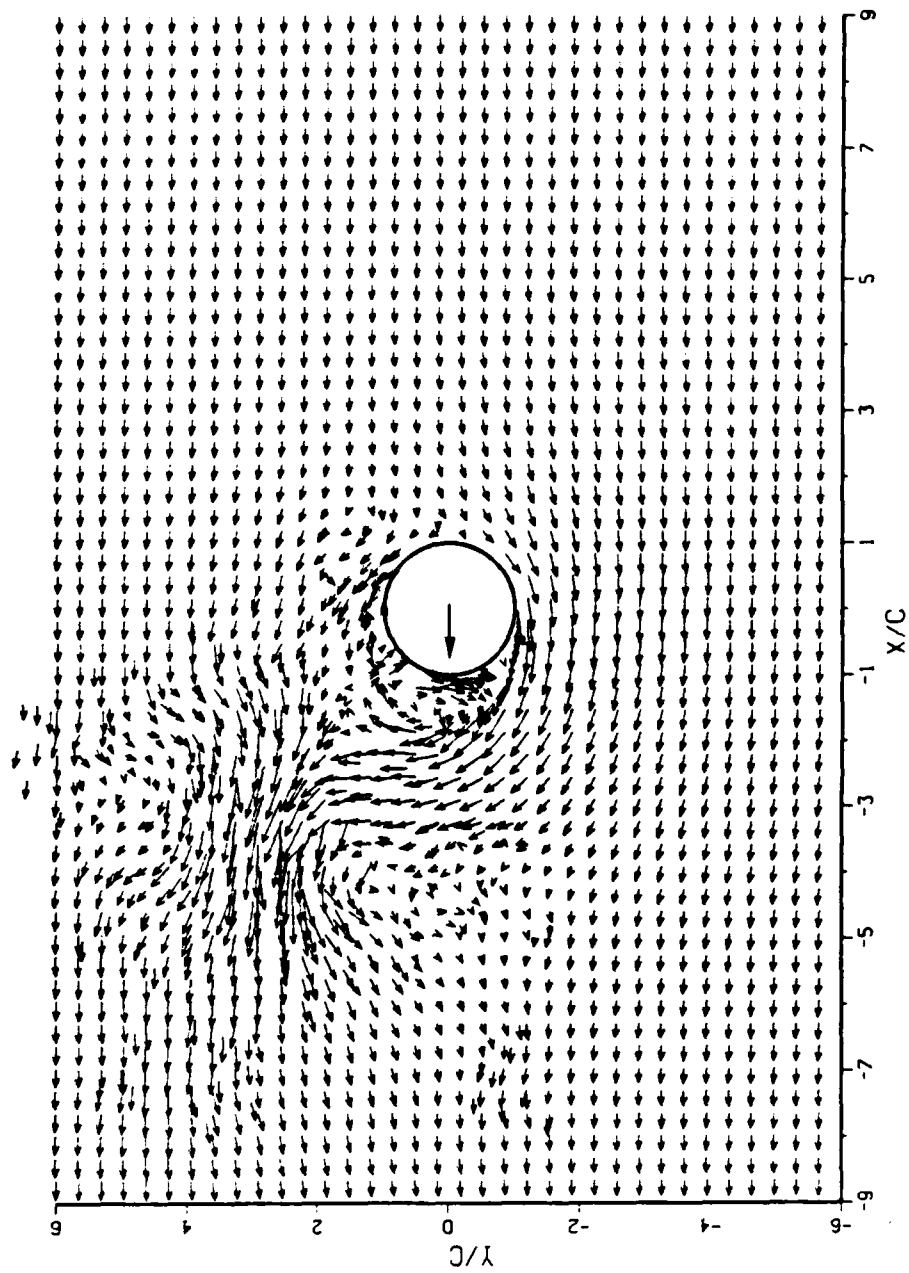


Figure 1.19 Flow field at $T^* = 1.875$.

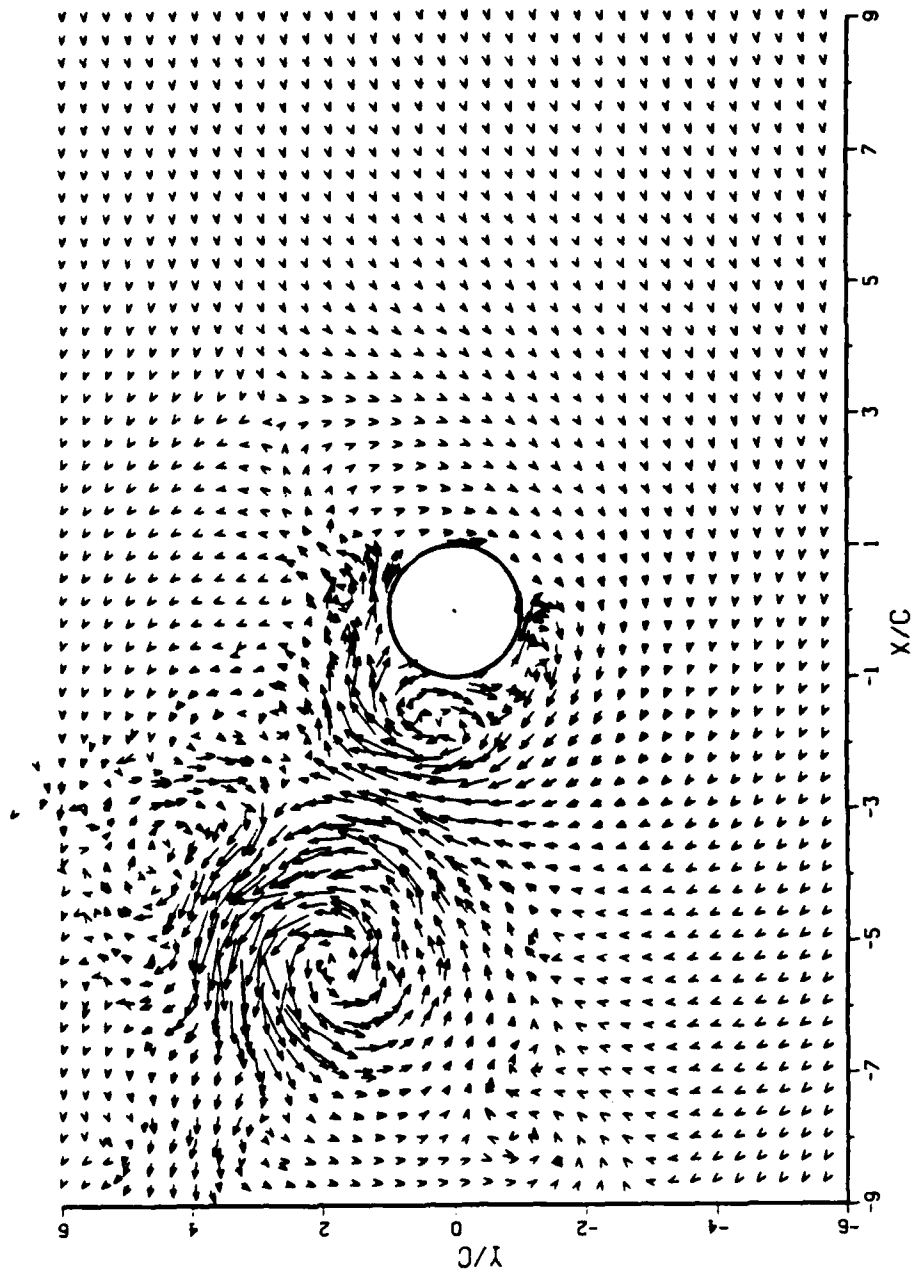


Figure 1.20 Flow field at $T^* = 2.00$.

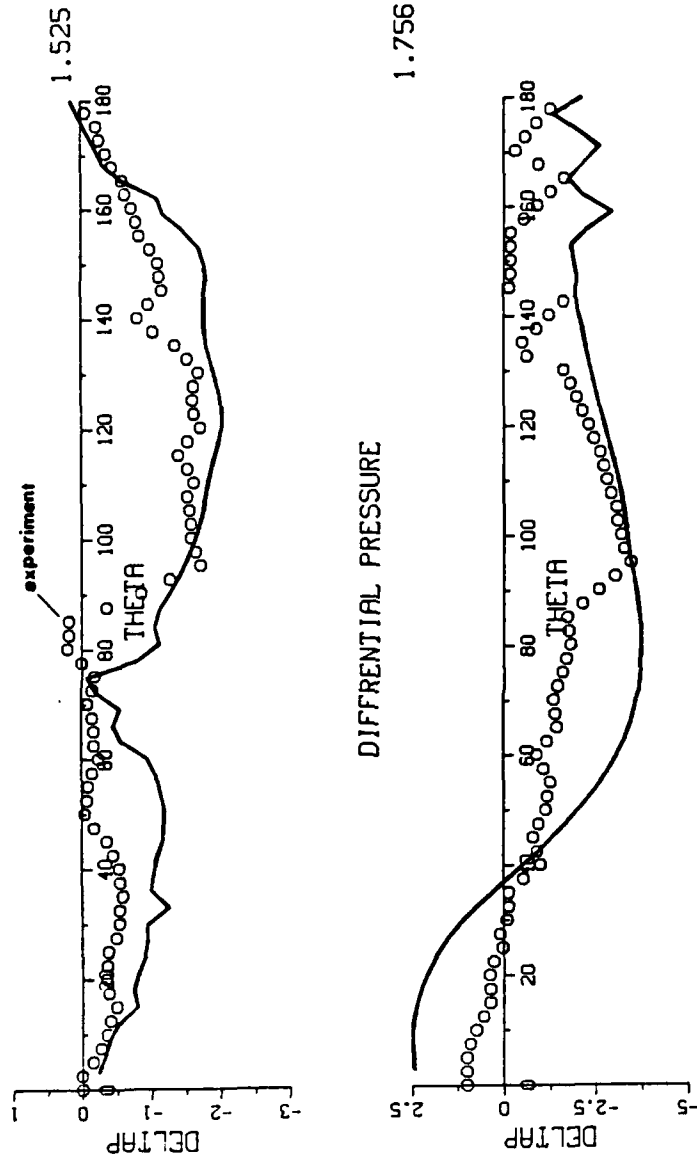


Figure 1.21 Comparison of numerical and experimental differential pressures.

OSCILLATING FLOW

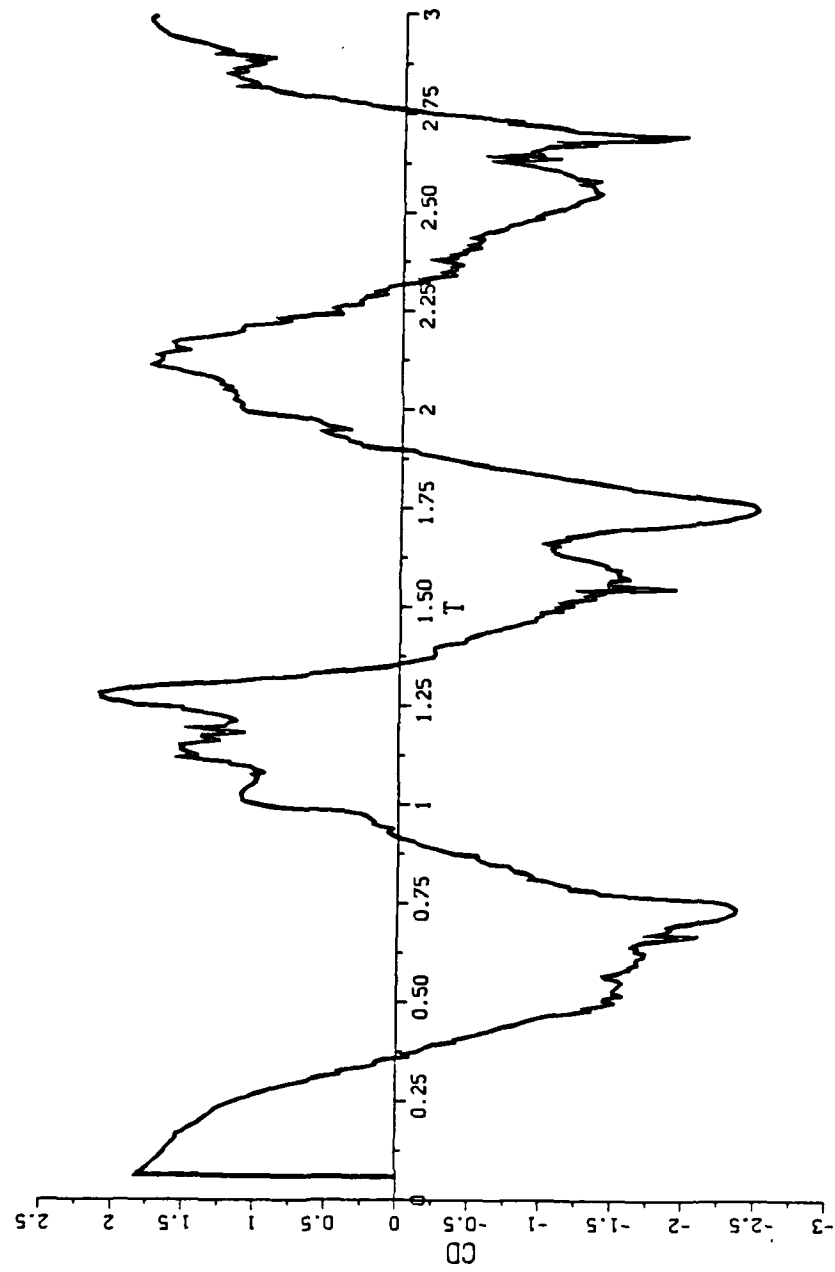


Figure 1.22 The calculated drag coefficient.

OSCILLATING FLOW

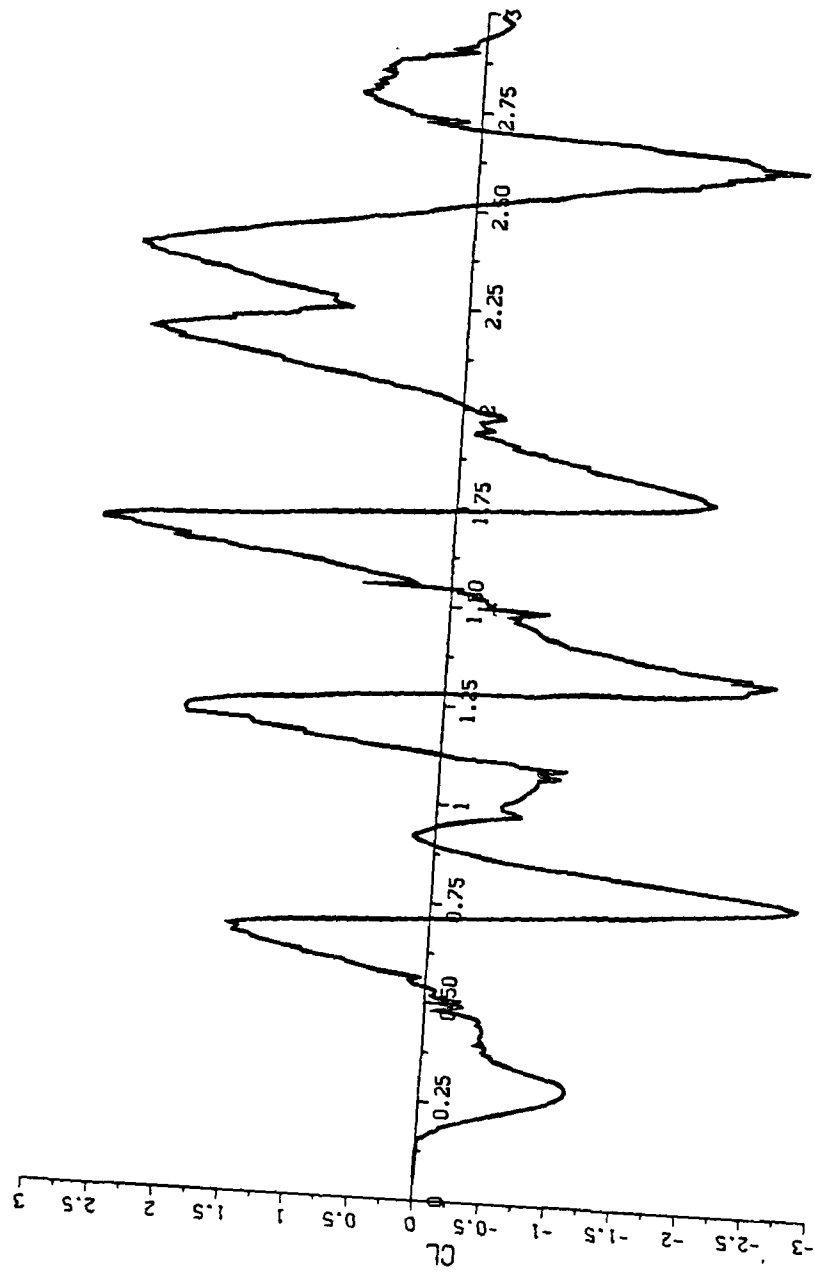


Figure 1.23 The calculated lift coefficient.

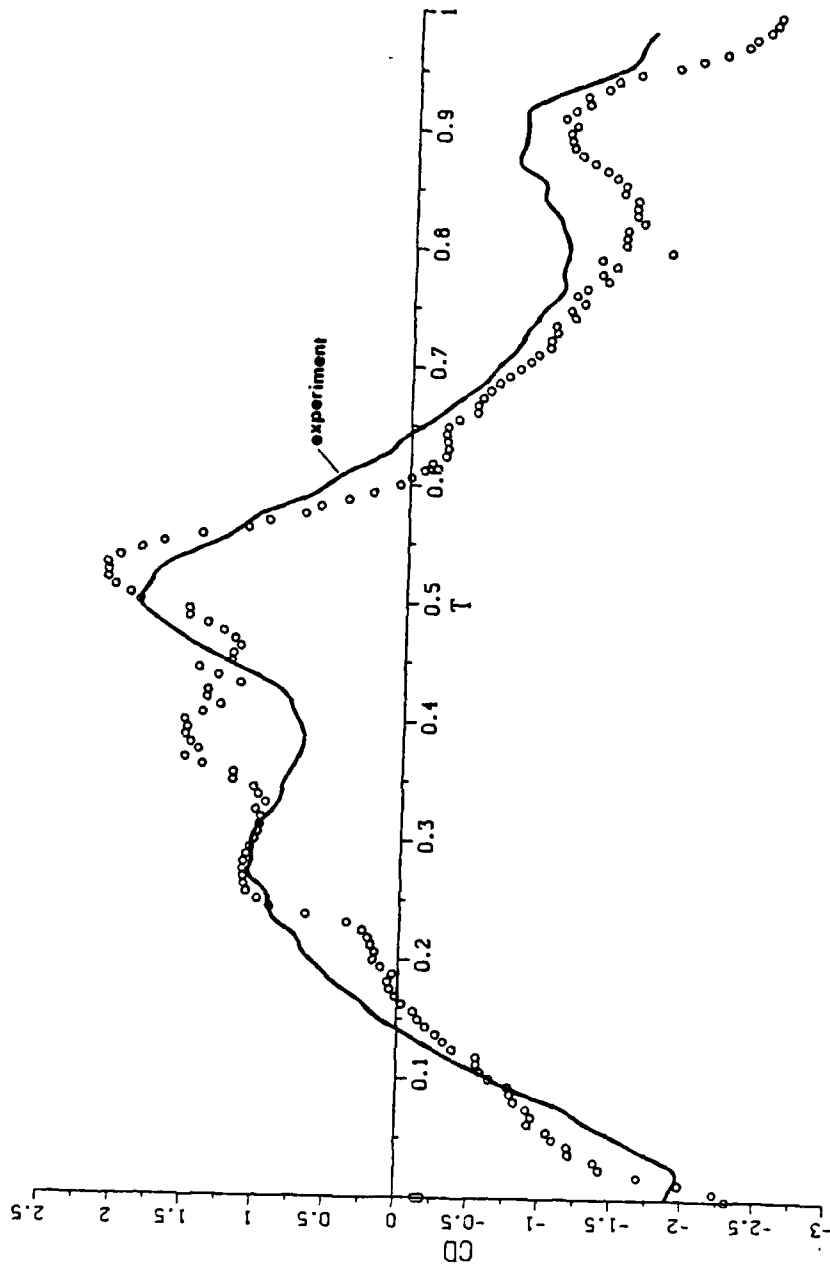


Figure 1.24 Measured and calculated drag force.

OSCILLATING FLOW

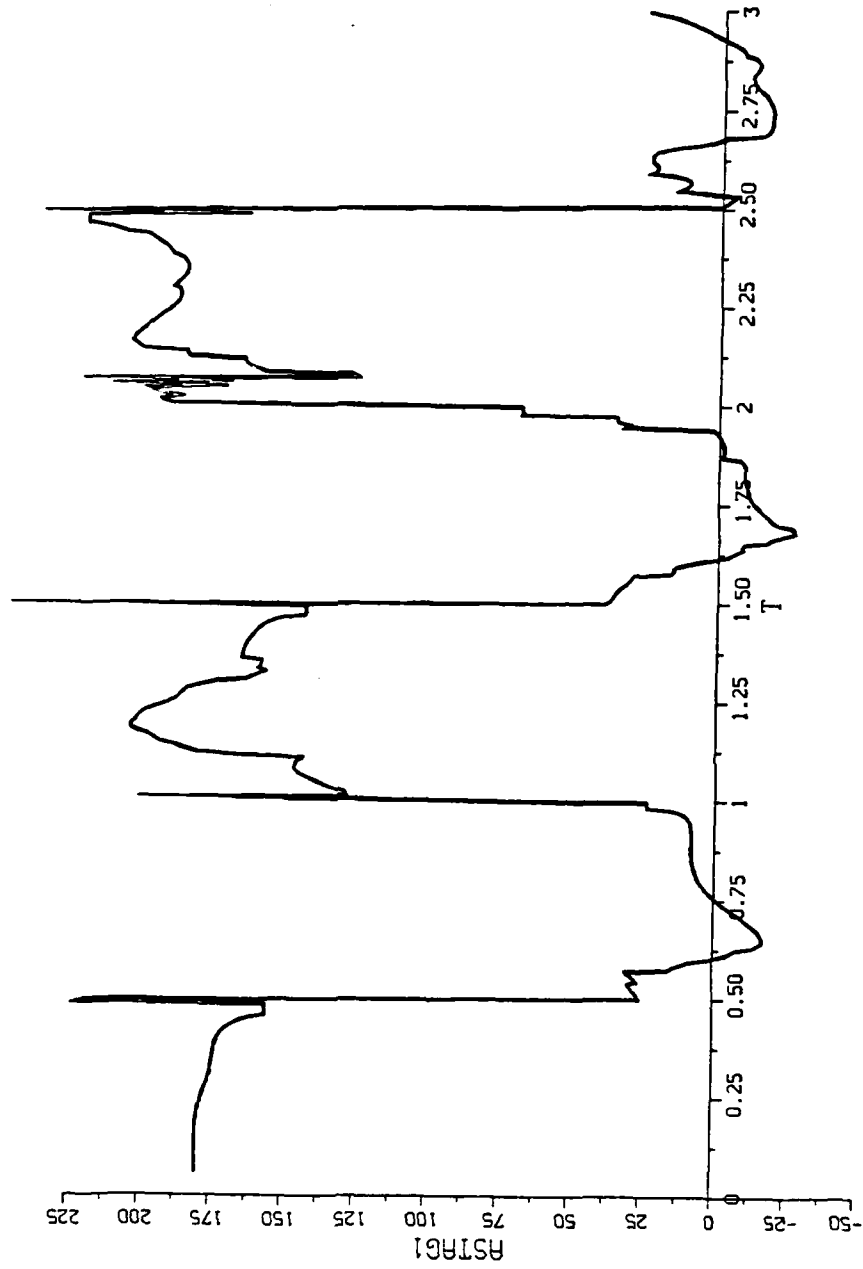


Figure 1.25 Upstream stagnation point.

OSCILLATING FLOW

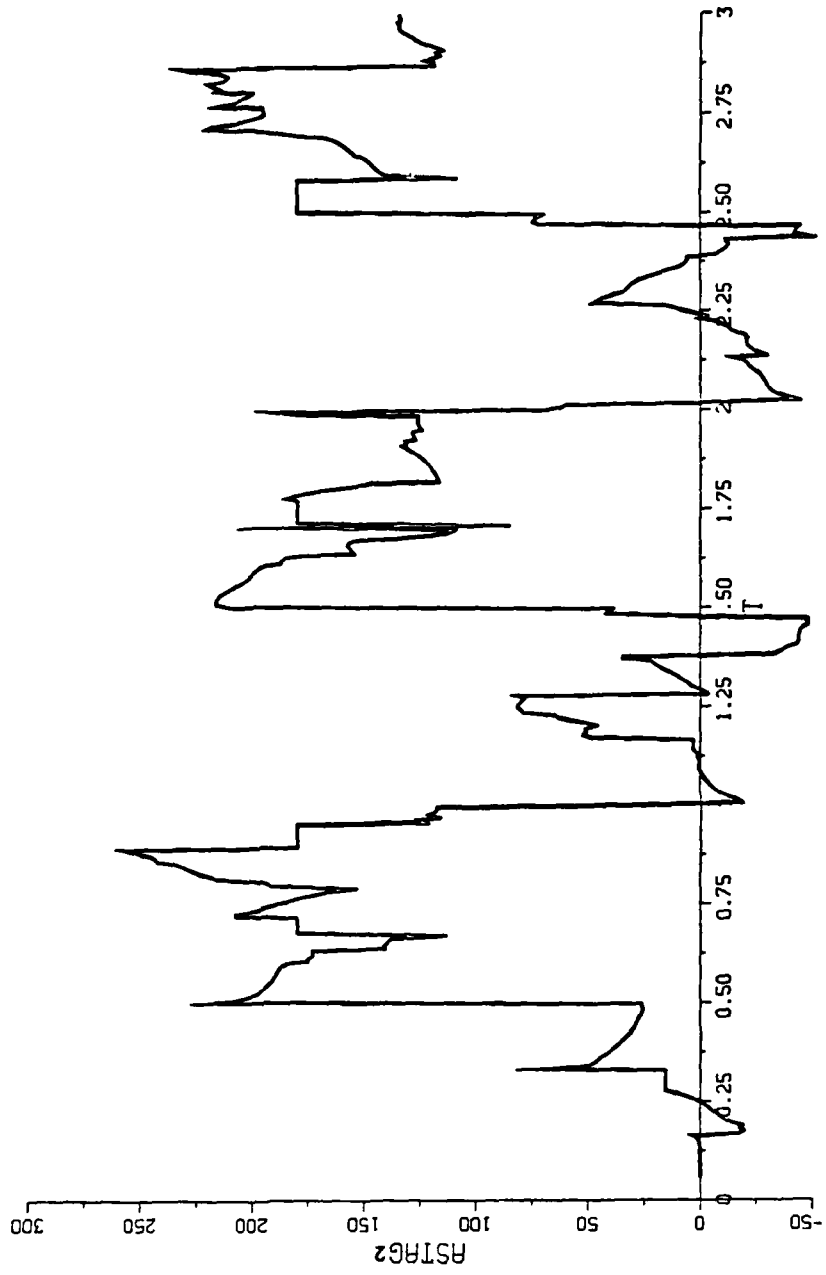


Figure 1.26 Downstream stagnation point.

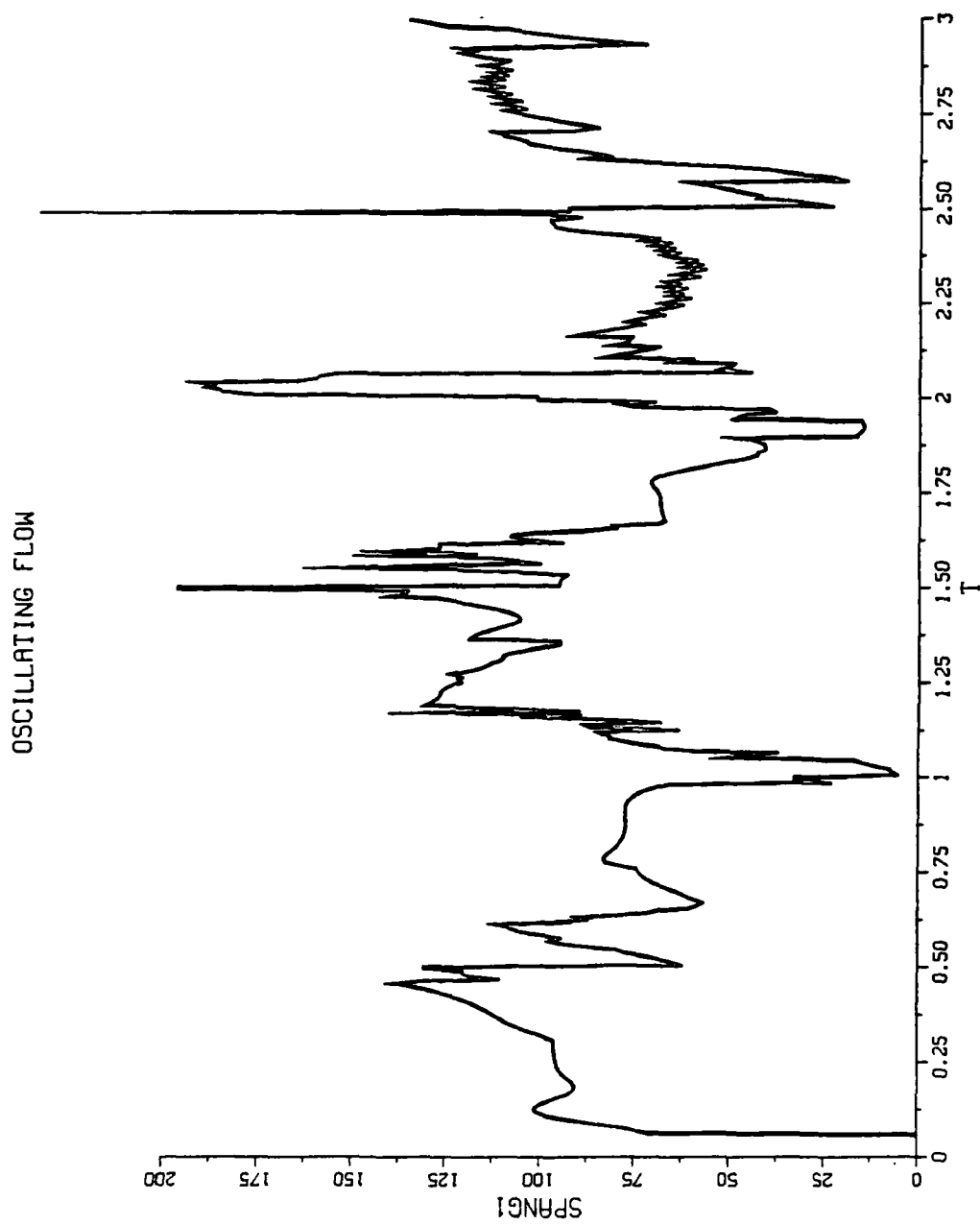


Figure 1.27 Primary separation points.

OSCILLATING FLOW

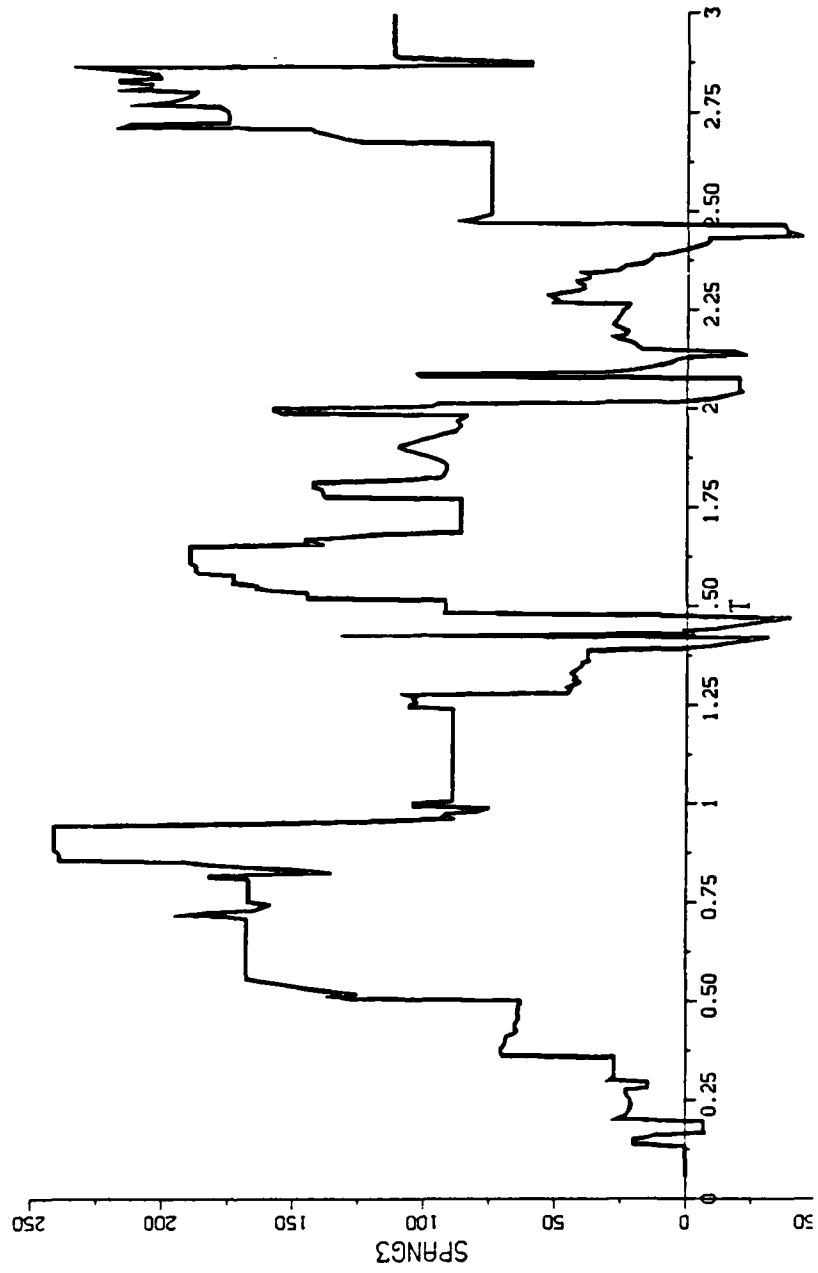


Figure 1.28 Secondary separation points.

OSCILLATING FLOW

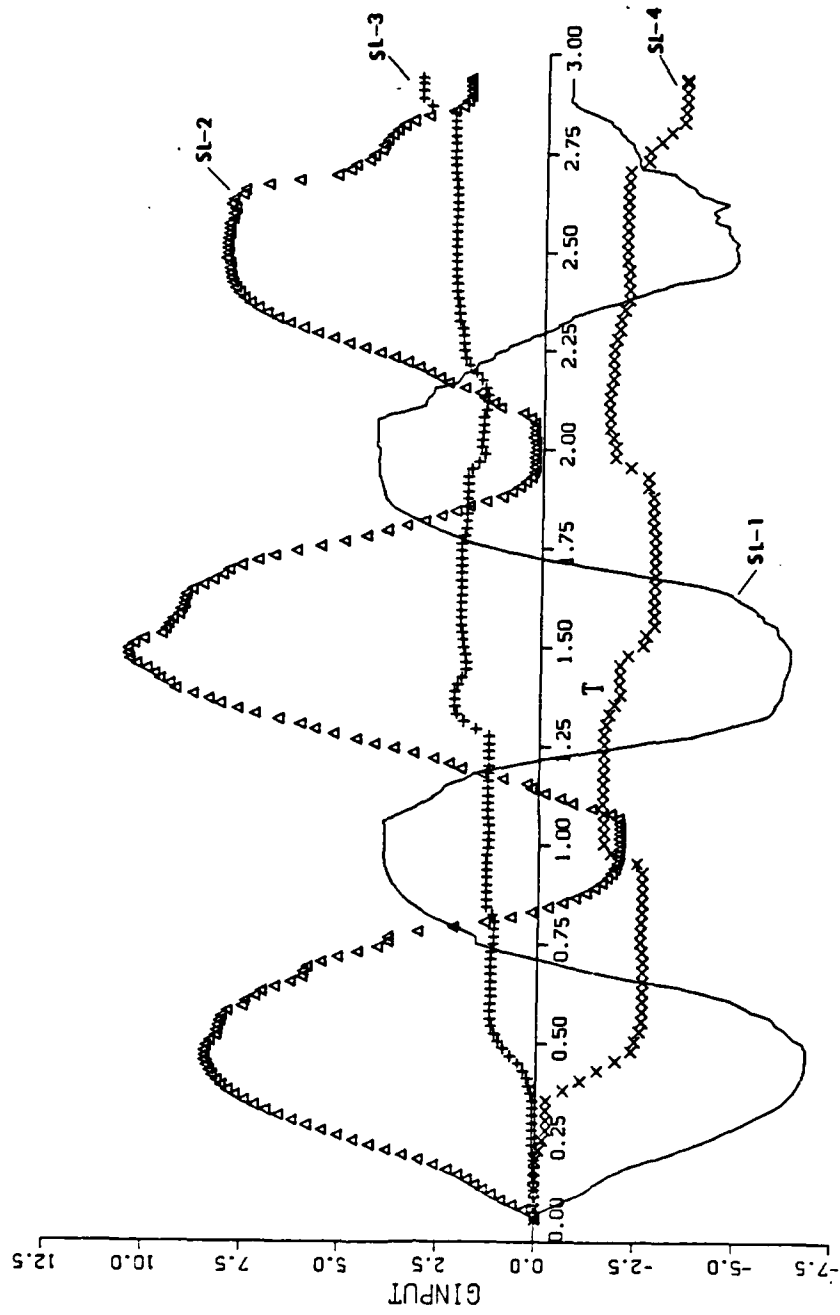


Figure 1.29 Vorticity fed into the flow field.

II. DISCRETE VORTEX ANALYSIS OF UNSTEADY FLOW ABOUT CAMBERED PLATES

A. INTRODUCTION

The determination of the deployment sequence of an axisymmetric porous parachute and the unsteady aerodynamic loads acting on it present a very complex coupled problem. The development of an analytical or numerical model which takes into account the effects of porosity, gaps, and variable opening schemes would allow numerical experiments on a large class of parachutes, reduce the number of expensive field tests to a few judiciously selected ones, and enable the designer to calculate the time history of the fall of the parachute and the strength required to survive the aerodynamic loads. However, the development of such a model is hampered by a number of difficulties.

The previous models for parachute loads are based by and large on empirical assumptions (see e.g., Heinrich and Saari 1987; Mcwey 1972). They rely on the observation that families of parachutes open in a characteristic length and seem to have aerodynamic properties that relate well to the projected area of the parachute. The apparent mass is assumed to be a function of the projected area only and is not a function of the prevailing flow characteristics. The vortex sheet analysis was used by Klimas (1977) to derive the acceleration-independent apparent mass coefficient for arbitrary-shaped axisymmetric surfaces. Muramoto and Garrard (1984) used a continuous-source model to predict the steady-state drag of ribbon parachutes. The analyses did not, however, deal with the evolution of the unsteady wake and its interaction with the canopy.

It is in view of the foregoing that a fundamental study of the separated time-dependent flow about two-dimensional rigid cambered plates was undertaken. Clearly, the flow about a rigid cambered plate is considerably simpler than that about a porous, axisymmetric, and flexible parachute and the results, regardless of the degree of their agreement with corresponding experiments, may not have direct relevance to the practical problem under consideration. But the object of this investigation was the understanding of the evolution of the wake under controlled conditions rather than to provide a design tool. It is hoped that an investigation of this type will reveal the underlying physics of the phenomenon (particularly that of the parachute collapse).

help to interpret the full-scale results and will provide inspiration for the development of more general vortex models with which the dynamics of axisymmetric, porous, and flexible parachute canopies can be investigated. Efforts directed towards the development of a general numerical model, driven by the ever-present pressures of practical considerations, are deemed somewhat premature. Such efforts will have to face not only the problem itself but also the deficiencies of the vortex models and attempt to address to both of them simultaneously. The model presented herein removes the ambiguities associated with the use of the discrete vortex model and provides results which are in excellent agreement with those obtained experimentally.

III. ANALYSIS

A. TRANSFORMATIONS AND THE COMPLEX VELOCITY POTENTIAL

The calculation of the velocity of any one of the vortices and the force acting on the body requires a conformal transformation (in which the camber becomes a circle), a complex-velocity potential representing the vortices, their images, and the two-dimensional irrotational flow around the body, and the use of the generalized Blasius theorem.

The flow in the circle plane may be transformed to that about a cambered plate through the use of two successive transformations, one from ζ plane to the ζ° plane and the other from the ζ° plan to the z plane. These are given by (see Fig. 3.1)

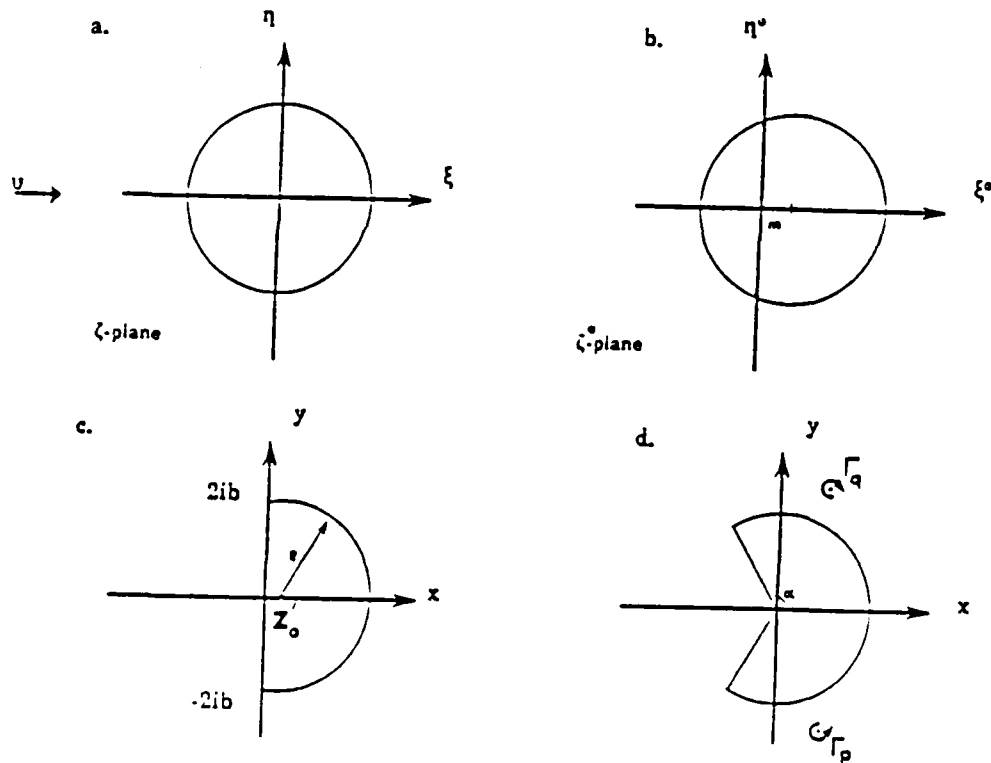


Figure 3.1 Circle and physical planes.

$$z = \zeta^{\circ} - \frac{b^2}{\zeta^{\circ}} \quad \text{and} \quad \zeta^{\circ} = \zeta + m \quad (3.1)$$

Combining the two, one has a direct transformation from the ζ plane to the z plane as

$$z = \zeta + m - \frac{b^2}{\zeta + m} \quad (3.2)$$

It is easy to show that the camber in the z plane is a circular arc.

The y -axis in the z plane passes through the tips of the camber. It is advantageous to locate the origin of the coordinate axes at the geometric center of the camber, i.e., at the center of the circle part of which represents the camber. This is easily accomplished by shifting the origin of the coordinate axes by

$$z'_0 = \frac{2m^2 - 1}{m} \quad (3.3)$$

where z'_0 is the x coordinate of the origin of the circle in the z plan. Thus, one has

$$z = \zeta + m - \frac{b^2}{\zeta + m} + z'_0 \quad \text{with} \quad z'_0 = -z_0 \quad (3.4)$$

which transforms the circle in Fig. 3.1a to the physical plane in Fig. 3.1d. Table 1 summarizes the relationship between m , z'_0 , the included angle of the camber, b , and the radius of the camber.

TABLE 1
SUMMARY OF THE PARAMETRIC RELATIONSHIP

m	z'_0	2α	b	$R = 1/m$
$\cos 60 = .5$	-1	120	.866	2
$\cos 45 = .707$	0.	180	.707	$\sqrt{2}$
$\cos 30 = .866$	$1/\sqrt{3}$	240	.5	$2\sqrt{3}$

The complex potential function W in the circle plane (see Fig. 3.1a) which describes a uniform flow U (assumed to be time-dependent) with a doublet at the origin to simulate the cylinder, Γ_{kq} clockwise-rotating vortices (called q-vortices), Γ_{kp} counter-clockwise rotating vortices (called p-vortices), and the images of all the p-and q-vortices in the circle plane may be written as

$$\begin{aligned}
 W = & -U\left(\zeta + \frac{c^2}{\zeta}\right) + \frac{i\Gamma_{0p}}{2\pi} \text{Ln}(\zeta - \zeta_{0p}) - \frac{i\Gamma_{0p}}{2\pi} \text{Ln}\left(\zeta - \frac{c^2}{\zeta_{0p}}\right) \\
 & + \sum_{k=1}^m \frac{i\Gamma_{kp}}{2\pi} \text{Ln}(\zeta - \zeta_{kp}) - \sum_{k=1}^m \frac{i\Gamma_{kp}}{2\pi} \text{Ln}\left(\zeta - \frac{c^2}{\zeta_{kp}}\right) - \frac{i\Gamma_{0q}}{2\pi} \text{Ln}(\zeta - \zeta_{0q}) \\
 & + \frac{i\Gamma_{0q}}{2\pi} \text{Ln}\left(\zeta - \frac{c^2}{\zeta_{0q}}\right) - \sum_{k=1}^m \frac{i\Gamma_{kq}}{2\pi} \text{Ln}(\zeta - \zeta_{kq}) + \sum_{k=1}^m \frac{i\Gamma_{kq}}{2\pi} \text{Ln}\left(\zeta - \frac{c^2}{\zeta_{kq}}\right) \quad (3.5)
 \end{aligned}$$

in which Γ_{kp} and ζ_{kp} represent respectively the strength and location of the k -th p-vortex, Γ_{kq} and ζ_{kq} the strength and location of the k -th q-vortex, and c the radius of the cylinder; an overbar indicates a complex conjugate. The need for the separate identification of the p-and q-vortices and for the singling out of one of the vortices in each shear layer (namely Γ_{0p} and Γ_{0q} , nascent vortices) will become apparent later.

B. COMPLEX VELOCITIES OF VORTICES

The convection of the vortices and the calculation of the forces acting on the body require the evaluation of the velocities at the vortex centers. For the velocities in the circle plane this reduces to subtracting from Eq. (3.5) the complex potential corresponding to the vortex for which the velocity components are to be determined and evaluating the derivative of the remaining terms at $\zeta = \zeta_k$. To determine the velocities in the physical plane, however, one has to subtract $(i\Gamma_k / 2\pi) \text{Ln}(z - z_k)$ from Eq. (3.5) or, in terms of ζ , the terms (see e.g., Sarpkaya 1967, 1975)

$$\frac{i\Gamma_k}{2\pi} \text{Ln}(\zeta - \zeta_k) + \frac{i\Gamma_k}{2\pi} \text{Ln}\left[1 + \frac{b^2}{(\zeta + m)(\zeta_k + m)}\right] \quad (3.6)$$

It should be noted that the first term in Eq. (3.6) is the complex function corresponding to the k -th vortex in the ζ plane. The second term appears merely as a consequence of the transformation used.

The above procedure may be generalized as follows. Consider the potential function for a single vortex in the physical plane and ignore, for the time being, the multiplier in front of the logarithmic term (i.e., $i\Gamma_k/2\pi$). Then one has

$$\text{Ln}(z - z_v) = \text{Ln}[f(\zeta) - f(\zeta_v)] \quad \text{with } z = f(\zeta) \quad (3.7)$$

equation (3.7) may be written as

$$\text{Ln}(z - z_v) = \text{Ln}(\zeta - \zeta_v) + \text{Ln} \frac{f(\zeta) - f(\zeta_v)}{\zeta - \zeta_v} \quad (3.8)$$

Evidently, the first term on the right hand side of Eq. (3.8) represents the vortex in the circle plane. Let us now examine the derivative of the second term with respect to z . One has,

$$\frac{dW}{dz}^p = \left[\frac{d}{d\zeta} \left(\frac{f(\zeta) - f(\zeta_v)}{\zeta - \zeta_v} \right) \right] \left(\frac{f(\zeta) - f(\zeta_v)}{\zeta - \zeta_v} \right)^{-1} \frac{d\zeta}{dz} \quad (3.9)$$

where $dz/d\zeta = f'(\zeta)$. In the neighborhood of ζ_v the function $f(\zeta)$ may be expanded as,

$$f(\zeta) - f(\zeta_v) = (\zeta - \zeta_v)f'(\zeta_v) + \frac{(\zeta - \zeta_v)^2}{2} f''(\zeta_v) + \dots \quad (3.10)$$

Thus, one has

$$\frac{dW}{dz}^p = \lim_{\zeta \rightarrow \zeta_v} \left[\frac{1/2 f''(\zeta_v)}{f(\zeta) - f(\zeta_v)} \right] \frac{1}{f'(\zeta)} \quad (3.11)$$

or

$$\frac{dW}{dz} \Big|_p = \frac{f'(\zeta_v)}{2f'^2(\zeta_v)} \quad (3.12)$$

Thus, the complex velocity in the physical plane reduces to

$$-u_x + iv_y = \frac{d}{d\zeta} \left[W(\zeta) - \frac{i\Gamma}{2\pi} \text{Ln}(\zeta - \zeta_v) \right] \Big|_{\zeta = \zeta_v} - \frac{i\Gamma}{4\pi} \frac{f'(\zeta_v)}{f'^2(\zeta_v)} \quad (3.13)$$

in which for a p-vortex

$$f'(\zeta_{kp}) = 1 + \frac{b^2}{(\zeta_{kp} + m)^2} \quad (3.14)$$

and

$$f''(\zeta_{kp}) = -\frac{2b^2}{(\zeta_{kp} + m)^3} \quad (3.15)$$

the last term in Eq. (3.13) reduces to

$$-\frac{i\Gamma_{kp}}{2\pi} \frac{(-b^2)(\zeta_{kp} + m)}{[(\zeta_{kp} + m)^2 + b^2]^2} \quad (3.16)$$

This result could have been deduced directly from Eq. (3.6). However, the generalization of the method enables one to apply Eq. (3.13) to any vortex for any transformation between the circle and the physical plane.

C. KUTTA CONDITION

The fact that the flow separates tangentially with a finite velocity at the edges of the plate (Kutta condition) may be expressed by requiring

$$\frac{dW}{d\zeta} = 0 \quad \text{at } \zeta = \zeta_t = -m \pm ib \quad (3.17)$$

Thus, inserting Eq. (3.5) in Eq. (3.17) one has

$$\begin{aligned}
 & + \frac{i\Gamma_{0p}}{2\pi} \left(\frac{1}{\zeta_t - \zeta_{0p}} - \frac{1}{\zeta_t - \frac{c^2}{\bar{\zeta}_{0p}}} \right) - \frac{i\Gamma_{0q}}{2\pi} \left(\frac{1}{\zeta_t - \zeta_{0q}} - \frac{1}{\zeta_t - \frac{c^2}{\bar{\zeta}_{0q}}} \right) \\
 & + \sum_{k=1}^m \frac{i\Gamma_{kp}}{2\pi} \left(\frac{1}{\zeta_t - \zeta_{kp}} - \frac{1}{\zeta_t - \frac{c^2}{\bar{\zeta}_{kp}}} \right) - \sum_{k=1}^m \frac{i\Gamma_{kq}}{2\pi} \left(\frac{1}{\zeta_t - \zeta_{kq}} - \frac{1}{\zeta_t - \frac{c^2}{\bar{\zeta}_{kq}}} \right) \\
 & - U \left(1 - \frac{c^2}{\zeta_t^2} \right) = 0.
 \end{aligned} \tag{3.18}$$

Equation (3.18) may be decomposed into two parts as

$$\begin{aligned}
 & + \frac{i\Gamma_{0p}}{2\pi} \left(\frac{1}{\zeta_t - \zeta_{0p}} - \frac{1}{\zeta_t - \frac{c^2}{\bar{\zeta}_{0p}}} \right) - \frac{i\Gamma_{0q}}{2\pi} \left(\frac{1}{\zeta_t - \zeta_{0q}} - \frac{1}{\zeta_t - \frac{c^2}{\bar{\zeta}_{0q}}} \right) \\
 & + (-u_o + iv_o) = 0.
 \end{aligned} \tag{3.19}$$

where the terms containing the strength of the nascent vortices represent the velocity induced at the tip of the camber by the nascent vortices and the term in parenthesis the velocity at the tip due to all other vortices (and their images), the doublet at the center of the circle in the ζ plane and the ambient velocity.

Equation (3.19) represents two coupled equations for the strengths and positions of the nascent vortices. Thus, the solution of the said quantities does, in general, require an iteration. However, this iteration may be avoided by noting that the velocity induced by a nascent vortex at the opposite tip is very small and certainly negligible. Thus, Eq. (3.19) for one of the nascent vortices may be reduced to

$$- \frac{i\Gamma_{0q}}{2\pi} \left(\frac{1}{\zeta_t - \zeta_{0q}} - \frac{1}{\zeta_t - \frac{c^2}{\bar{\zeta}_{0q}}} \right) + (-u_o + iv_o) = 0 \tag{3.20}$$

A similar expression may be written for the other nascent vortex. The use of the Kutta condition, as expressed by Eq. (3.20), will be further explained following the discussion of the tip velocity. It suffices to note that all nascent vortices satisfying the Kutta condition do not yield either the same tip velocity or the same velocity distribution in the neighborhood of the tip. There are, in fact, certain preferred positions for the nascent vortices which yield physically realistic velocity distributions near the tips of the cambered plate. These nascent vortex positions will be discussed later.

D. TIP VELOCITY

According to the Kutta condition the tangential velocity at the tip is finite. The purpose of the following is to determine this finite velocity. It may be determined either through the use of l'Hopital's rule or through the use of a more general expression which is valid for all other transformations.

The velocity at the tip is given by

$$\frac{dW}{dz} = \frac{dW}{d\zeta} \cdot \frac{d\zeta}{dz} \quad \text{at } z_t = z_0 \pm 2ib \quad (3.21)$$

For an arbitrary point z , Eq. (3.4) yields,

$$\frac{d\zeta}{dz} = \frac{1}{2} \pm \frac{\sqrt{ib}}{2\sqrt{z - z_t}} \quad (3.22)$$

In general, one may write Eq. (3.22) as

$$\frac{d\zeta}{dz} = \frac{1}{2} \pm \frac{(z - z_0)}{2\sqrt{(z - z_0)^2 + 4b^2}} \quad (3.23)$$

or multiplying both sides with $\sqrt{(z - z_t)}$, one has

$$\begin{aligned} f(z) &= (z - z_t)^{1/2} \frac{d\zeta}{dz} \\ &= \frac{1}{2} (z - z_t)^{1/2} \pm \frac{(z - z_0)}{2\sqrt{z - (z_0 \pm 2ib)}} \end{aligned} \quad (3.24)$$

Thus, as $z_t \rightarrow z_0 \pm 2ib$, one has

$$f(z_t) = (z - z_t)^{1/2} \frac{d\zeta}{dz} = \frac{1}{2} \sqrt{ib} \quad (3.25)$$

or

$$\frac{d\zeta}{dz} = \frac{\sqrt{ib}}{2\sqrt{(z-z_t)}} = \frac{2f^2(z_t)}{\zeta - \zeta_t} \quad (3.26)$$

Expanding $dW/d\zeta$ in the neighborhood of ζ_t one has

$$\frac{dW}{d\zeta} = (\zeta - \zeta_t) W''(\zeta_t) + \dots \quad (3.27)$$

Combining Eqs. (3.26) and (3.27) one finally has

$$\left. \frac{dW}{dz} \right|_{z=z_t} = 2 \frac{d^2W}{d\zeta^2} f^2(z_t) \quad (3.28)$$

Noting that for the case under consideration $f^2(z_t) = ib/4$, one has

$$\left. \frac{dW}{dz} \right|_{z=z_t} = \frac{d^2W}{d\zeta^2} \cdot \left(\frac{ib}{2} \right) \quad (3.29)$$

Equation (3.29) yields the desired finite tip velocities. It is easy to show that it may be obtained directly from Eq. (3.21) through the use of l'Hopital's rule.

E. TIME DEPENDENT-FORCES

The force acting on the body in the physical plane may be calculated either through the use of the pressure distribution or through the use of the rate of change of impulse.

Bernoulli's equation for unsteady flow is given by

$$\left(\frac{P_1}{\rho} + \frac{V_1^2}{2} \right) - \left(\frac{P_2}{\rho} + \frac{V_2^2}{2} \right) - \int_1^2 \frac{\partial V}{\partial t} ds = f(t) \quad (3.30)$$

where the indices indicate two points on the body in the physical plane. Since there is no pressure drop across the shear layer and since the integral term in Eq. (3.30) is zero at the tip (i.e., $ds=0$), one has

$$f(t) = \frac{V_{t1}^2}{2} - \frac{V_{t2}^2}{2} \quad (3.31)$$

where V_{t1} and V_{t2} represent the tangential velocities on the upstream and downstream faces of the tip. It is important to note that $f(t)$ in Eq. (3.31) is also the time rate of change of circulation, i.e., the rate at which vorticity is shed into the wake from the tip of the cambered plate.

The normalized form of Bernoulli's equation between any two points m and n then becomes

$$\frac{P_m - P_n}{\rho U_o^2} = \frac{V_{t1}^2 - V_{t2}^2}{U_o^2} + \frac{V_n^2 - V_m^2}{U_o^2} + \frac{\partial}{\partial t} \int_m^n \frac{V}{U_o^2} ds \quad (3.32)$$

The integration of the differential pressure between the upstream and downstream faces of the camber yields the force components in the x and y directions, i.e., the drag and lift forces.

The force acting on the body can also be calculated through the rate of change of impulse. It is given by

$$F = 4\pi\rho c^2 \dot{U} \left(1 - \frac{m^2}{2c^2} \right) + \frac{\partial}{\partial t} [\Gamma_n (z_n - z_{ni})] \quad (3.33)$$

which may be written as

$$C_d + i C_L = \frac{F}{2\rho U_o^2 b} = 2\pi \left(\frac{c\dot{U}}{U_o^2} \right) \left(\frac{c}{b} \right) \left(1 - \frac{m^2}{2c^2} \right) + \frac{c}{2b} \frac{\partial}{\partial(U_o t/c)} \left\{ \frac{\Gamma_k}{U_o c} \left[f\left(\frac{\zeta_k}{c}\right) - f\left(\frac{c}{\zeta_k}\right) \right] \right\} \quad (3.34)$$

in which U_o is the reference velocity; \dot{U} , the rate of deceleration of flow and $z = f(\zeta_k)$, i.e., the transformation given by Eq. (3.4). Equation (3.34) may also be deduced directly from the generalized Blasius equation. It is important to note that the force calculated from Eq. (3.34) includes the effect of the rate of change of circulation between two successive time steps. Thus, it may be smaller or larger (depending on the sign of Γ) than the force calculated through the integration of the instantaneous differential pressure Eq. (3.32). This is because of the fact that the instantaneous pressure depends **only** on the prevailing flow conditions and does not account for the rate of change of total circulation between successive time steps. In the calculations to follow U_o and c are taken as unity for sake of simplicity.

F. METHOD OF CALCULATION

The methods used in the past in the determination of the vorticity flux from sharp-edged bodies may be roughly classified into two broad categories. The first of these involves the use of variable nascent vortex positions (see e.g., Sarpkaya 1968, 1975) and the second, the use of fixed nascent vortex positions (see e.g., Clements 1973-1975).

The method of fixed positions involves the selection of a suitable fixed point in the flow near the separation point and the use of the velocity U_s at that point to calculate the rate at which vorticity is shed into the wake from

$$\frac{\partial \Gamma}{\partial t} = \frac{1}{2} U_s^2 \quad (3.35)$$

In this method the positions of the nascent vortices are the crucial parameters. The previous applications of this method did not examine the effect of the position of the nascent vortices on the velocity distribution in the neighborhood of the separation

point. Only the distance of the fixed point to the body was varied and bracketed between two subjective limits by comparing the calculated results with those obtained experimentally. In this method no interaction is allowed between the shed vortices and the amplitude of oscillation of the point or the time of appearance of the nascent vortices. Furthermore, the time interval is chosen more or less arbitrarily (Kiya and Arie 1977) (repeating a few calculations with a single program with only the time step changed and also by referring to the results of the previous investigations). Thus, the velocities at the outer edges of the shear layers are only indirectly related to the strength of the nascent vortices and the fixed time interval. Evidently, the velocities in the inner and outer edges of the shear layers, the time interval, the strength and position of the nascent vortices, and the Kutta condition are interdependent and that both the position of the nascent vortices and the time interval cannot be chosen arbitrarily, even if they are chosen judiciously on the basis of previous experience and trial calculations.

Sarpkaya (1975) used the method of variable nascent vortex positions and determined the rate of shedding of vorticity from the relation

$$\frac{\partial \Gamma}{\partial t} = \frac{1}{2} U_{sh}^2 \quad (3.36)$$

where U_{sh} is interpreted as the velocity in the shear layers calculated by using the average of the transport velocities of the first four vortices in each shear layer. The positions of the nascent vortices are chosen so as to satisfy the Kutta condition at the edges of the body and thus they can move slightly with time. Thus, this method simulates in a satisfactory manner the mechanism of feedback from wake fluctuations to the fluctuations in the rate of circulation. The number of disposable parameters is reduced to a minimum and in this sense this method is superior to the method of fixed positions. However, the use of the average of the transport velocities of the first four vortices remained questionable.

It was often assumed that the vorticity flux could not be calculated, at each time interval, as it is applied to sharp-edged bodies, through the use of the mathematically finite velocity occurring at the sharp edges of the body. This assumption was based on the fact that the separation points are singularities of the transformation used and the numerical procedures may not be stable.

It is on the basis of the foregoing that an original study was undertaken to establish once and for all a method whereby the nascent vortices may be introduced into the flow without any ambiguities. The method finally arrived at will be explained through the use of a series of figures and velocity plots.

Figures 3.2a and 3.2b show the tip region in the circle and physical planes, respectively. The regions A and B in Fig. 3.2a were discretized through the use of a suitable grid and a single vortex was placed at a grid point. The strength of the vortex was determined from the Kutta condition Eq. (3.20). Then the velocity normal to the radial line OZ in the physical plane (Fig. 3.2b) was calculated in the vicinity of the tip through the use of the complex velocity potential.

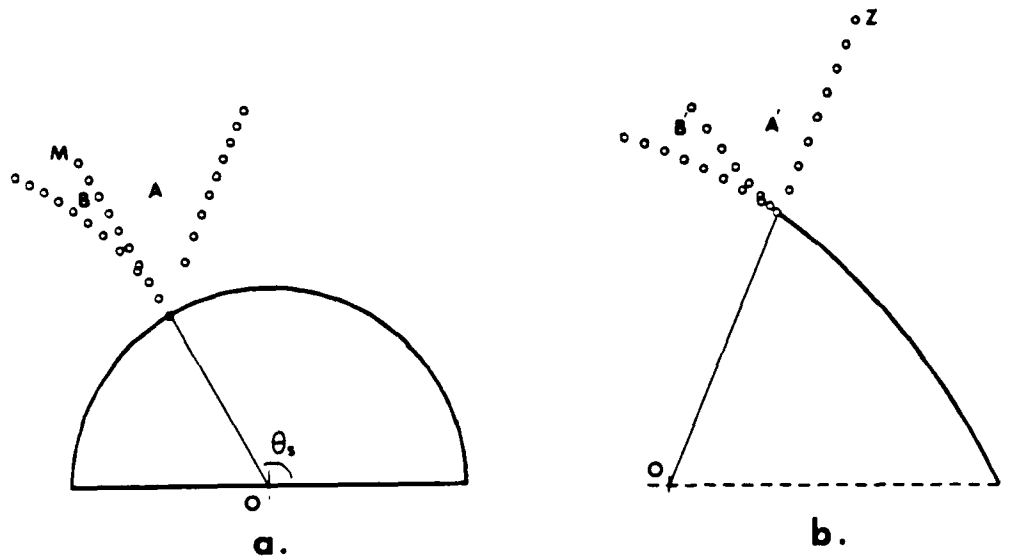


Figure 3.2 Tip region in the circle and physical planes.

Placing the vortex along the radial line OM (in the ζ plane) yields a single valued tip velocity independent of the strength and the position of the vortex and dependent only on the plate geometry, i.e., b and θ_s . It is easy to show that the velocity at the edge of the plate reduces to $q_t = \pm (ib/2) e^{-3i\theta_s} (-1 - e^{-2i\theta_s})$. For the case of a 120-degree camber this gives an absolute value of 0.433 with a velocity direction opposite to that expected at the edge of the plate (Fig. 3.3).

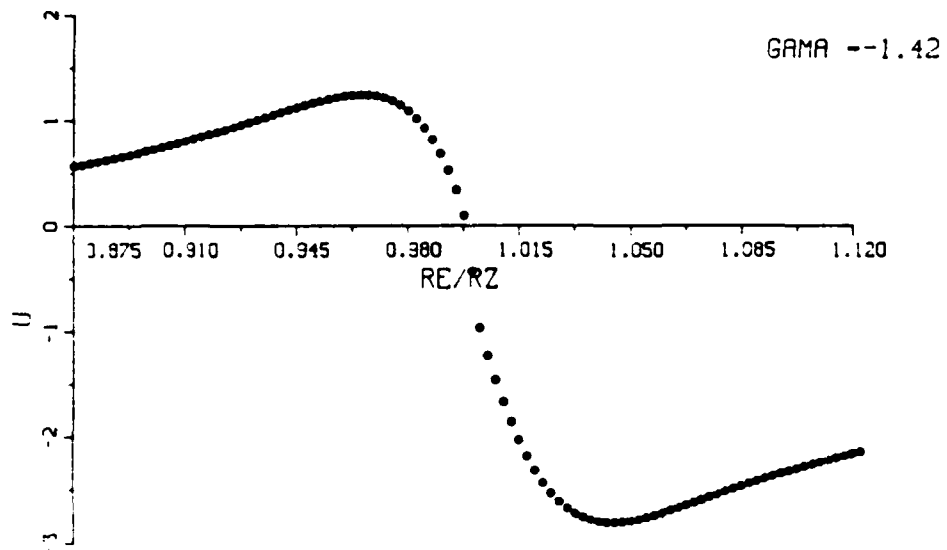


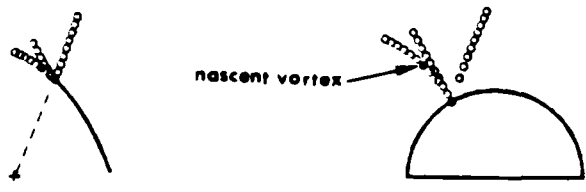
Figure 3.3 Velocity profile along the radial line (nascent vortex on OM).

Placing the nascent vortex to the right of the radial line OM in the circle plane (or along the circular arc in the physical plane) always requires a stronger vortex to satisfy the Kutta condition and results in a tip velocity which is unrealistic both in magnitude and direction (Fig. 3.4).

Placing the nascent vortex along the radial line OZ in the physical plane or outside the region A shifts the point of maximum velocity away from the edge of the plate (towards the downstream side). This, in turn, results in a leakage of fluid through the shear layer and requires a stronger vortex to satisfy the Kutta condition (Fig. 3.5).

The entire region A enclosed by the transformation of the radial line OZ in the physical plane and the radial line OM in the ζ plane, is examined to determine the most appropriate positions of the nascent vortex. Figures 3.6 through 3.8 show a three-dimensional plot and the contour lines of Γ , $U(\max)$, $U(\text{tip})$, and $U(\text{tip})$ as a function of the radial positions R and the angular positions $R\theta$ for those locations of the nascent vortex for which $\Gamma < 1$, $U(\max) U(\text{tip}) < 6$, and $U(\text{tip}) < 6$.

Figures 3.9 through 3.11 show three representative velocity profiles for three different positions of the nascent vortices in the region defined above. The most striking feature of these figures is that the maximum velocity near the tip can exceed considerably and unrealistically the velocity **at the tip** and that only for certain vortex positions does the maximum velocity (the velocity on the inner face of the camber at the tip) approach smoothly the finite tip velocity. These calculations have shown that there is, in fact, a finite region in which the nascent vortices may be introduced in order to produce a tip velocity which is nearly equal to the maximum velocity in the vicinity of the tip. Clearly, it is only for unique combinations of the radial distance R and the angular position $R\theta$ that the said velocity ratio is equal to unity.



GAMA --2.28

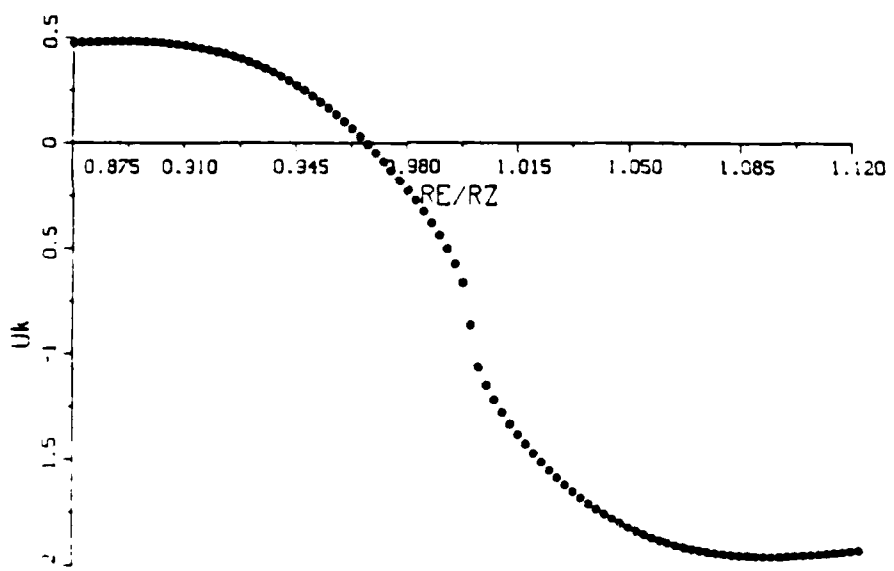


Figure 3.4 Velocity profile along the radial line (nascent vortex to the right of OM).

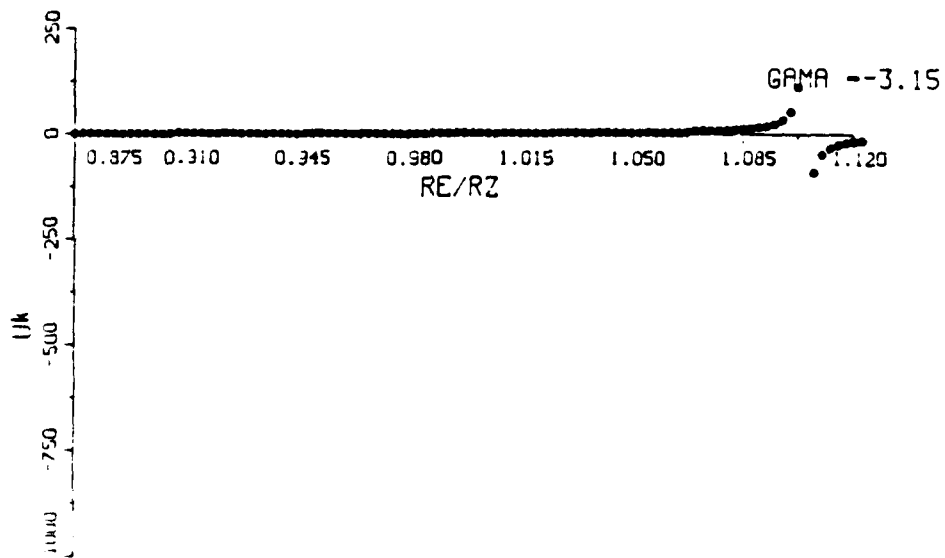


Figure 3.5 Velocity profile along the radial line (nascent vortex on OZ).

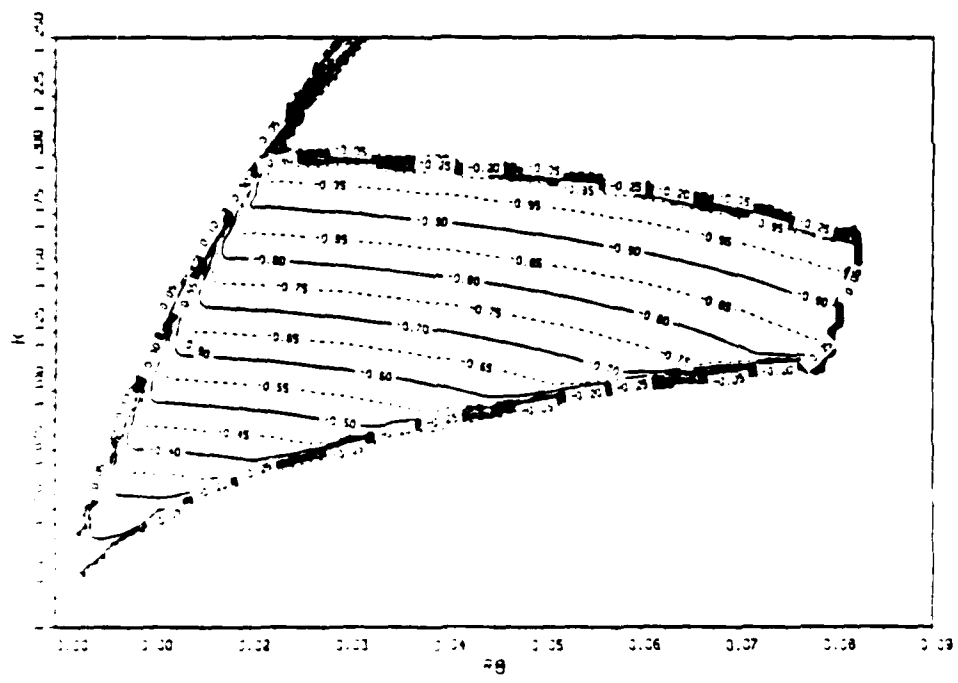
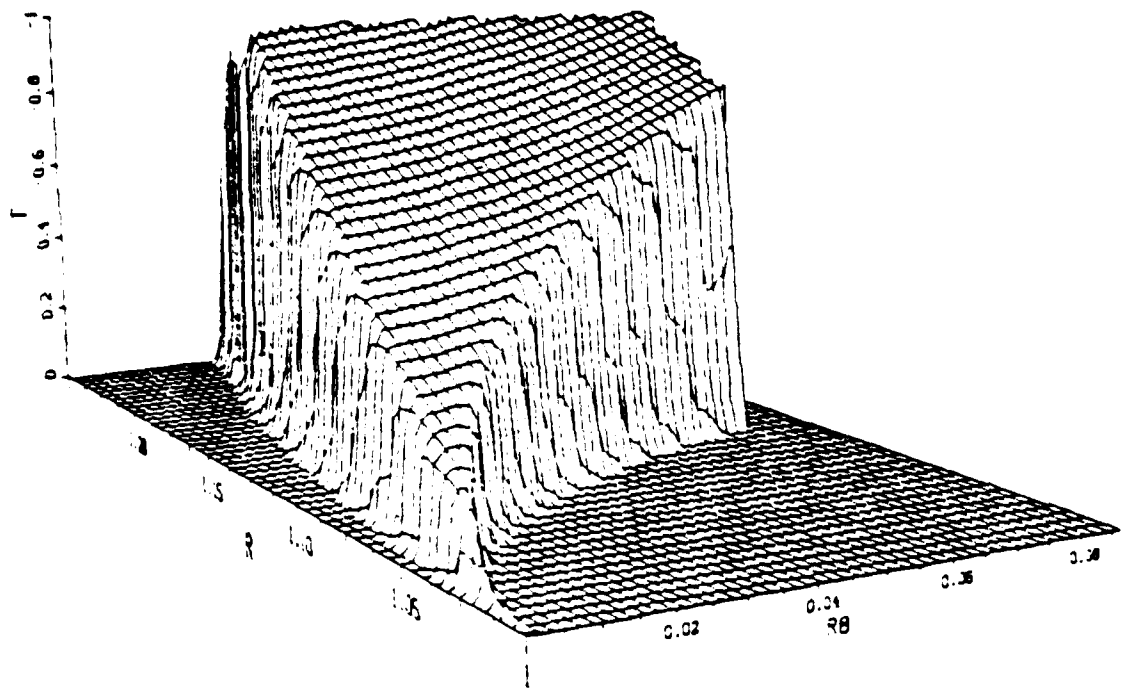


Figure 3.6 Three-dimensional plot of and the contour lines for Γ distribution.

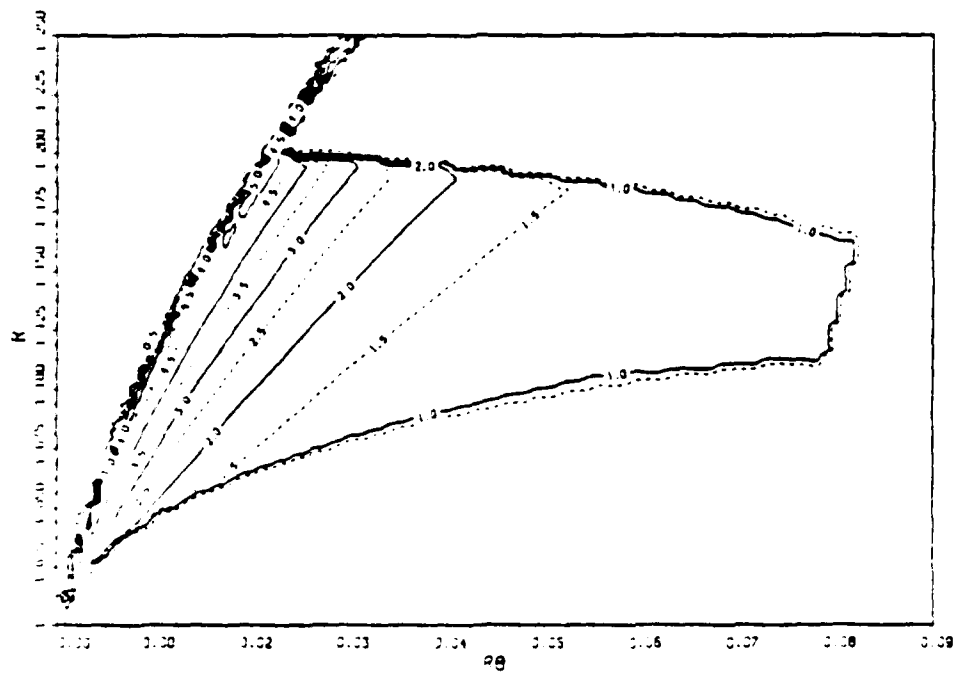
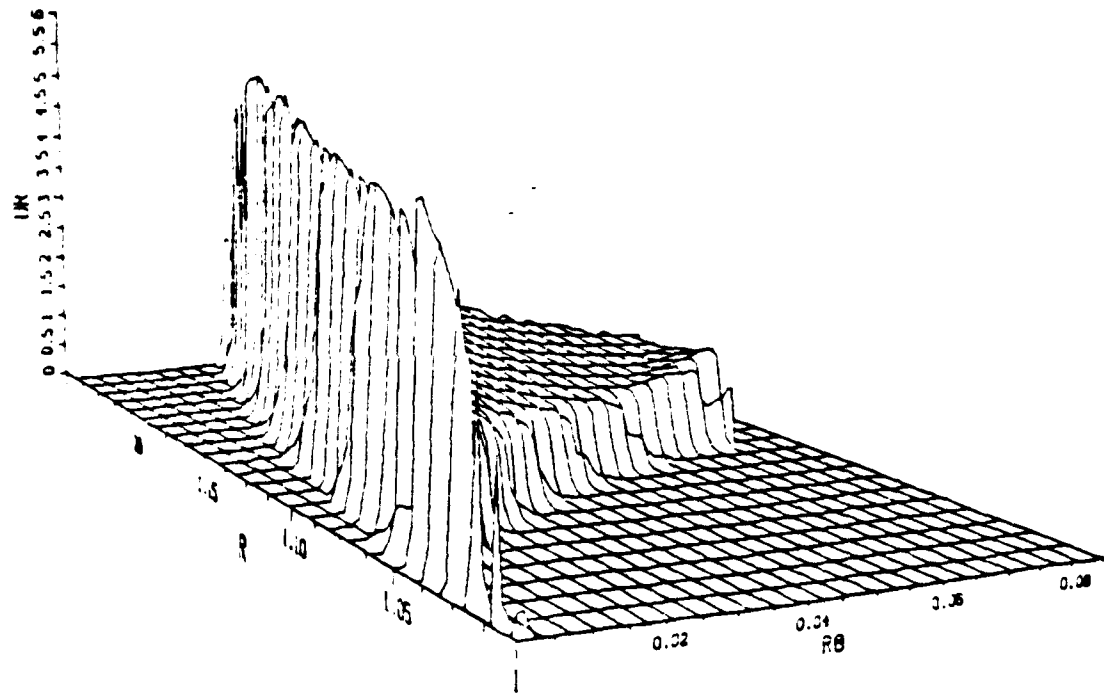


Figure 3.7 Three-dimensional plot of the velocity ratio.

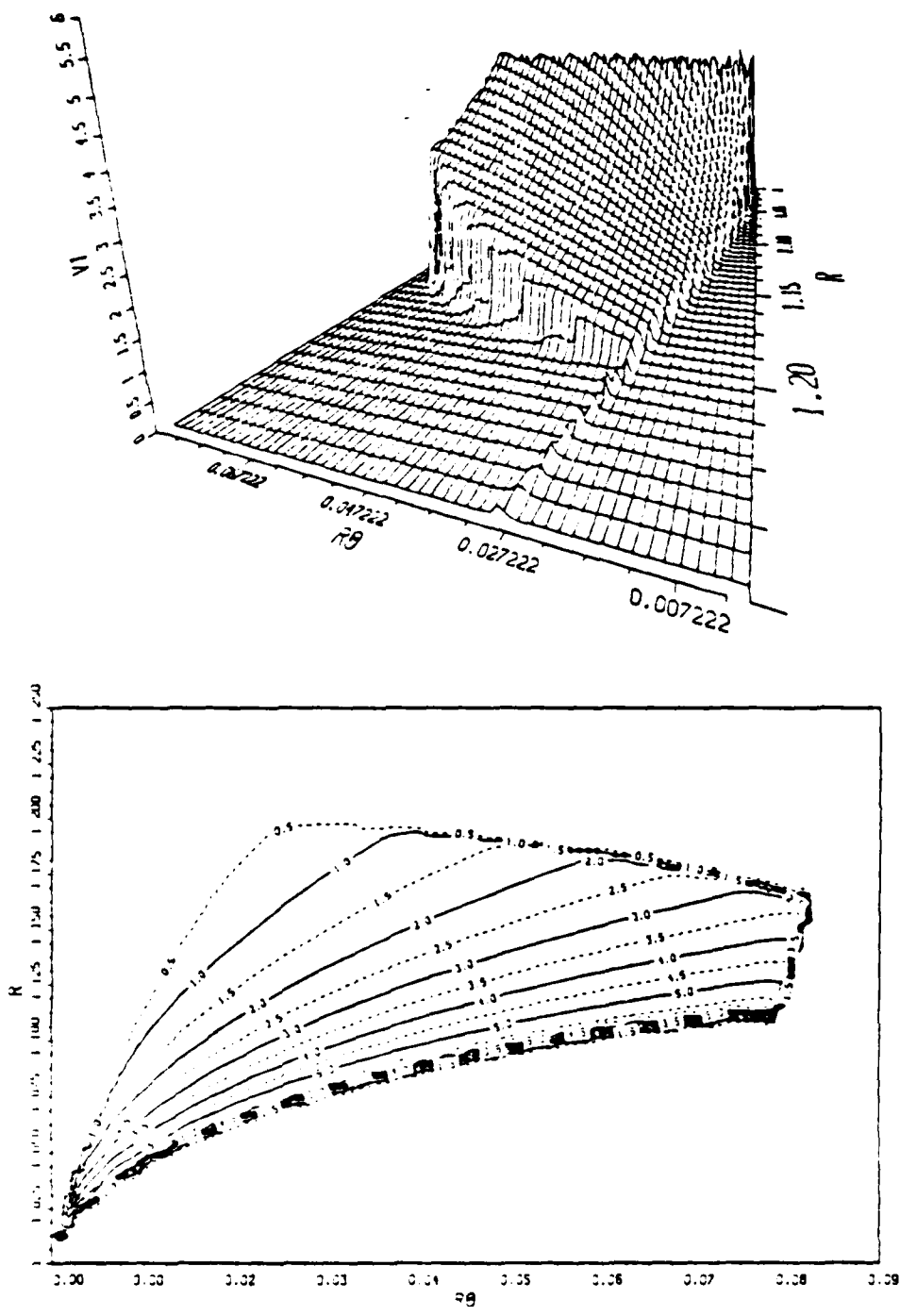


Figure 3.8 Three-dimensional plot of the tip velocity.

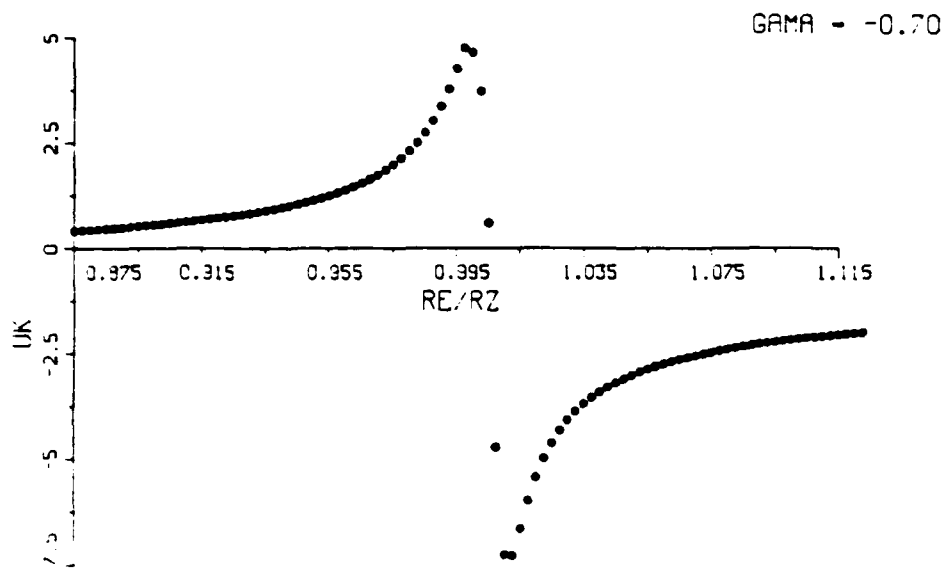
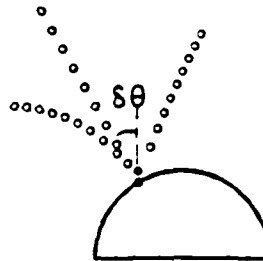
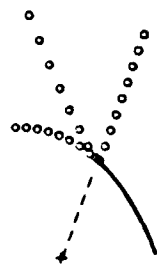


Figure 3.9 Velocity profile along the radial line (nascent vortex at $\epsilon = 0.05$, $\delta\theta = 25.0^\circ$).

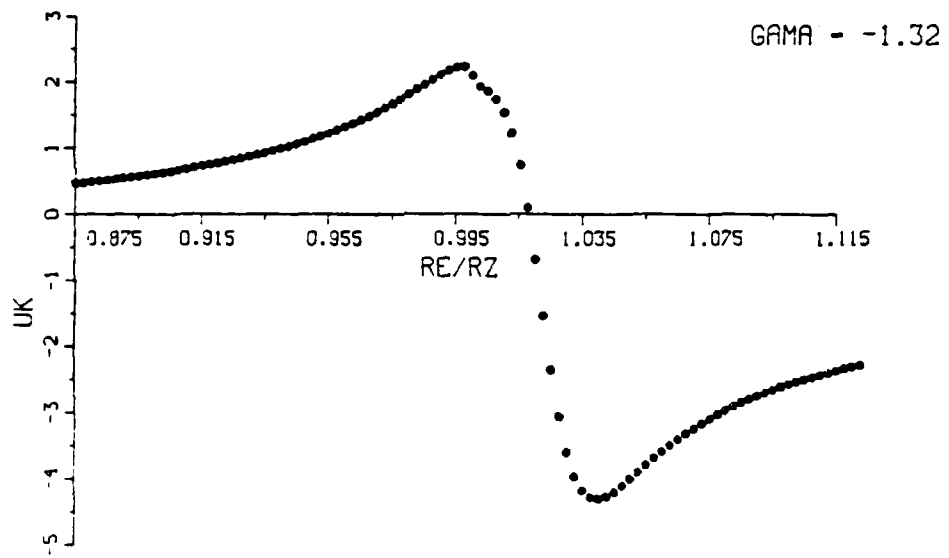
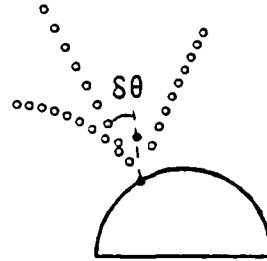
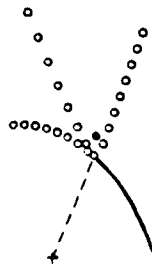


Figure 3.10 Velocity profile along the radial line (nascent vortex at $\epsilon = 0.10$, $\delta\theta = 25.0^\circ$).



GAMA - -2.35

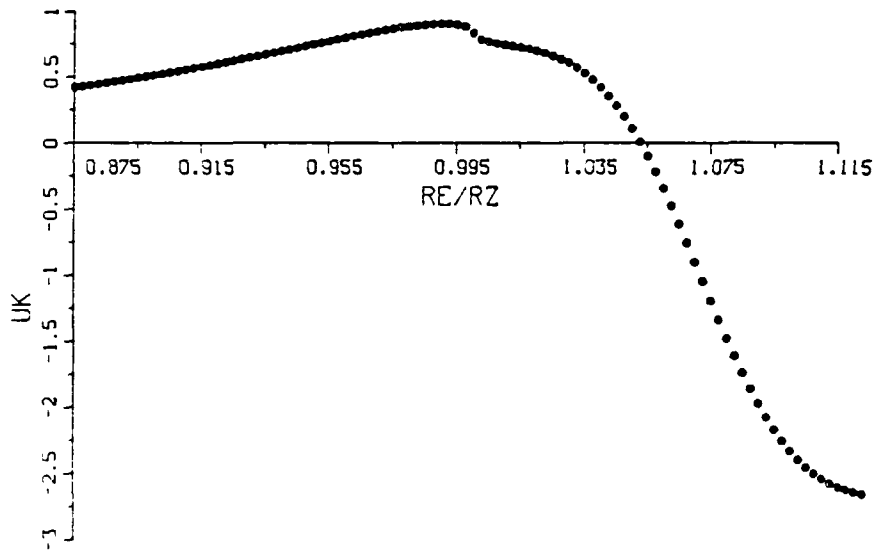


Figure 3.11 Velocity profile along the radial line (nascent vortex at $\epsilon = 0.20$, $\delta\theta = 25.0^\circ$).

Figure 3.6 shows the required vortex strength as a function of a R and $R\theta$. Even though these calculations have been carried out with a single vortex, the subsequent calculations with larger number of vortices have shown that the relationship between the maximum velocity and the tip velocity remains practically invariant as long as the nascent vortices are always introduced at the fixed point which produces $U(\max)/U(\text{tip}) \sim 1$ for the single vortex. The reason for this is that the said velocity ratio is primarily dictated by the nascent vortex and the complex potential used in Eq. (3.29), to calculate the tip velocity, encompasses the effect of all the vortices in the flow field. In other words, it does not make any difference whether the velocity q_0 , i.e., $(u_0 - iv_0)$ in Eq. (3.20) is produced by the ambient velocity or by a large number of vortices in the field.

The fact emerging from the foregoing analysis is that the nascent vortex **cannot** be placed arbitrarily (e.g., along the radial line in the circle plane or along the extension of the camber in the physical plane). Otherwise, the velocity distribution in the vicinity of the tip becomes unrealistic and unrepresentative of the evolution of the shear layers on either side of the camber. Furthermore, one is then forced to make arbitrary assumptions regarding the strength and the convection of the nascent vortices.

The foregoing extensive analysis led to the conclusion that the nascent vortices should be introduced at $r = 1.0925$ and $\theta = \theta_s \pm 2.08^\circ$, for the case of the 120-degree camber. To be more precise, the two nascent vortices are placed at the angular positions $\theta_p = \theta_{s1} - 2.08$, and $\theta_q = \theta_{s2} + 2.08$, during the period for which $V_1 - V_2 > 0.2$. For $V_2 > V_1$, the positions of the two nascent vortices are switched to their corresponding images with respect to the radial line OM, i.e., they are placed at $\theta_{pi} = \theta_{s1} - 2.08$ and $\theta_{qi} = \theta_{s2} - 2.08$. The evolution of the very early stages of the flow in the immediate vicinity of the tips of the camber is shown in Fig. 3.12.

In Fig. 3.12a the velocity field is a consequence of the first two nascent vortices introduced at the points noted above. Figures 3.12b through 3.12d show the development of the flow field and the starting tip vortex subsequent to the introduction of the 4th, 8th, and 11th nascent vortex, respectively.

There is not a unique procedure for relating the rate at which vorticity is shed into the wake, the Kutta condition, the velocity with which the nascent vortices are convected, and the time interval for the convection, all of which help to simulate the experimentally observed features of the free shear layers. Fage and Johansen (1928), through quite ingenious experiments with steady flow about various bluff bodies, have

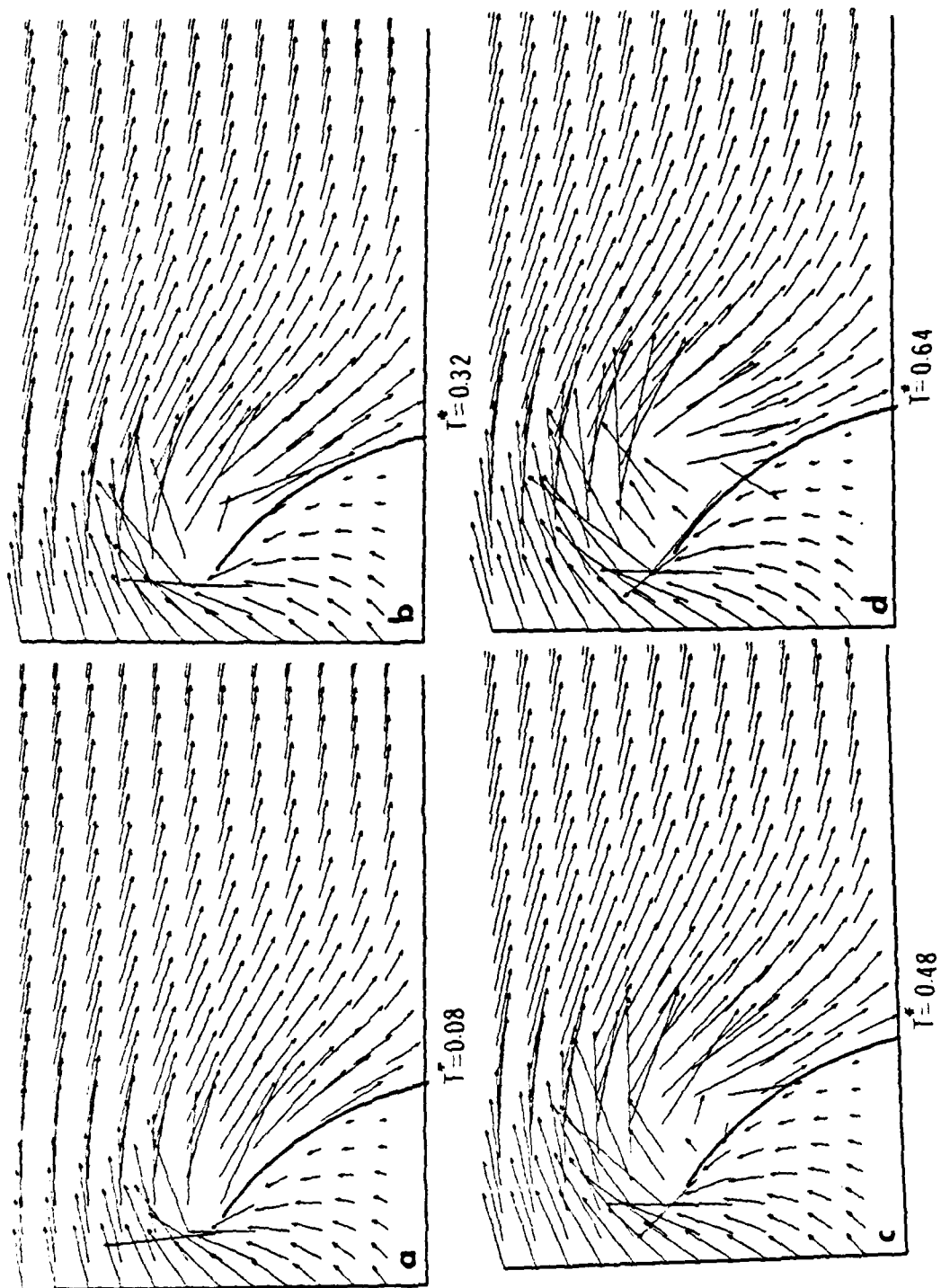


Figure 3.12 Velocity field in the vicinity of the tip.

shown that vorticity is shed from the two sides of an axisymmetric body (a circular cylinder) or a sharp-edged body (a plate normal to the flow) at the same rate; that the motion in a sheet is steady near the body, except possibly near the inner edge of the shear layers; that fluid flows into a sheet through both edges, but at a greater rate through the outer edge; that at each section of the sheet the velocity rises from a small value to a well-marked maximum value (approximately $V_1 U = 1.45$) and then very slowly decreases to about 1.35 within a distance of approximately $y \sim 2c$, where the breadth of the sheet reaches a value of $\Delta \sim c$; and finally, that the velocity V_1 at the outer edge of the sheet is much larger than the velocity V_2 at the inner edge (except during the deceleration period of the flow) and V_2^2 may be ignored in calculating the vorticity flux from $\partial \Gamma / \partial t = 0.5 (V_1^2 - V_2^2)$.

In the present calculation the vortex strength, the velocities on either side of the shear layer, and the time interval are related by

$$\Gamma = 0.5 (V_1^2 - V_2^2) \cdot \Delta t \quad (3.37)$$

in which Γ is the strength of the nascent vortex, $V_1 = U(\text{tip})$ and V_2 is the velocity at the downstream face of the camber near the tip. The velocity V_2 can be calculated correctly in a number of ways, to be described later. Suffice it to note that in general V_2 is very small (for steady flow) and that the method of its calculation has very little or no influence on the strength of the nascent vortex or on the time interval to be used for a given vortex strength. The velocity V_2 becomes important only when the wake begins to move towards the camber (i.e., during the period of flow deceleration).

To explain the computational details of the method let us consider a particular time t after the start of the motion and assume t to be sufficiently large so that there are a number of vortices in the wake. Then the appearance and convection of the vortices proceed as follows:

- (1) Determine the strength of the nascent vortices from the Kutta condition .Eq. (3.20), in which ζ_0 is a known fixed position for each nascent vortex ;
- (2) Place the nascent vortices at ζ_{0p} and ζ_{0q} and calculate the velocity V_1 at the two edges of the plate ;
- (3) Calculate V_2 , representing the velocity at the inner boundary of the shear layer, as the average of the velocities at three points along the radial line OZ in the physical plane i.e., at $r = 1, 1.05, \text{ and } 1.1$;

- (4) Calculate the time interval, for each edge of the plate, from Eq. (3.37) using the known values of Γ and the velocities V_1 and V_2 . Store the average of the two time intervals for use in subsequent calculations;
- (5) Calculate the velocity induced at the center of all other vortices;
- (6) Convect the two nascent vortices with a velocity $0.5(V_1 + V_2)$ for an average time interval Δt (note that the vorticity is convected with the average velocity of the shear layer). If the distance travelled by a nascent vortex is not within 0.05 ± 0.01 , it is convected twice for a time interval Δt . The subsequent convections of the nascent vortices are made using the velocity induced at their center.
- (7) Convect all other vortices for the same time-interval Δt using a second order scheme given by

$$z(t + \Delta t) = z(t) + 0.5 [3\dot{z}(t) - \dot{z}(t - \Delta t)] \cdot \Delta t \quad (3.38)$$

in which $\dot{z} = u + iv$.

- (8) Remove the vortices from the calculation whenever they come nearer than 0.05 to the camber in the physical plane (except the first 20 vortices from the tip);
- (9) Coalesce the same sign vortices with a separation of less than 0.05 (in the physical plane, except the first 20 vortices);
- (10) Calculate the tangential velocities and pressures on the inner and outer faces of the camber. Determine the drag and lift forces through the integration of pressure and through the use of the rate of change of impulse. Make plots of suitable variables (e.g., velocity distribution near the tip, variation of nascent vortex circulation with time, evolution of the wake, etc.);
- (11) Check the flow conditions to determine the state of the calculations:
 - (a) If $V_1 - V_2 > 0.2$ repeat the foregoing steps;
 - (b) Stop the introduction of nascent vortices if $0 < V_1 - V_2 < 0.2$ and return to step No. 5;
 - (c) If $V_2 > V_1$ switch the angular positions of the nascent vortices to their image points. Calculate V_2 as the average of the three velocities, at the upstream side of the tip of the camber, at three radial locations (0.95, 0.9, and 0.85) and repeat the foregoing steps; and

- (12) Make plots of the variations of various flow parameters (e.g., tip velocity, nascent vortex circulation, evolution of the wake, force coefficients, etc.) and terminate the run.

The foregoing steps are quite general and can be used for any camber, provided that the optimum points of placement of the nascent vortices are determined through a similar analysis for the desired camber angle.

IV. DISCUSSION OF RESULTS

A. NUMERICAL AND PHYSICAL EXPERIMENTS

The calculations were carried out for a time-dependent normalized velocity given by

$$\frac{U}{U_0} = 1 \quad \text{for} \quad T^* = \frac{U_0 t}{c} \leq 8.65 \quad (4.1)$$

and

$$\frac{U}{U_0} = 1 - 0.1539(T^* - 8.65) + 0.00531(T^* - 8.65)^2 \quad (4.2)$$

which corresponds to that encountered in a series of experiments carried out in a vertical water tunnel. A detailed description of the equipment and procedures is given by Sarpkaya and Ihrig (1986) and will not be repeated here. Evidently, the calculations can be carried out for any specified variation of the velocity. For the case under consideration, the flow begins to decelerate at $T^* = 8.65$ and the velocity of the ambient flow reduces to zero at about $T^* = 19$, (see Fig. 4.1)

The computer program provided, at times specified, the positions of all the vortices, the rate of shedding of vorticity from the tips of the camber, the velocity distribution on the upstream and downstream faces of the camber, the total and differential pressure distributions, and the force coefficients.

Figures 4.2 through 4.4 show, at $T^* = U_0 t / c = 4.35$, the evolution of the wake, the tangential velocities at the upstream and downstream faces of the camber, the velocity profile along the radial line passing through the tip, and the total and differential pressure distributions (these plots are available at every time step but are not reproduced here for sake of brevity). These and other figures show that the characteristics of the flow develop symmetrically prior to the onset of deceleration ($T^* < 8.65$) and the differential pressure is positive everywhere (i.e., the pressure inside the camber is larger than that outside).

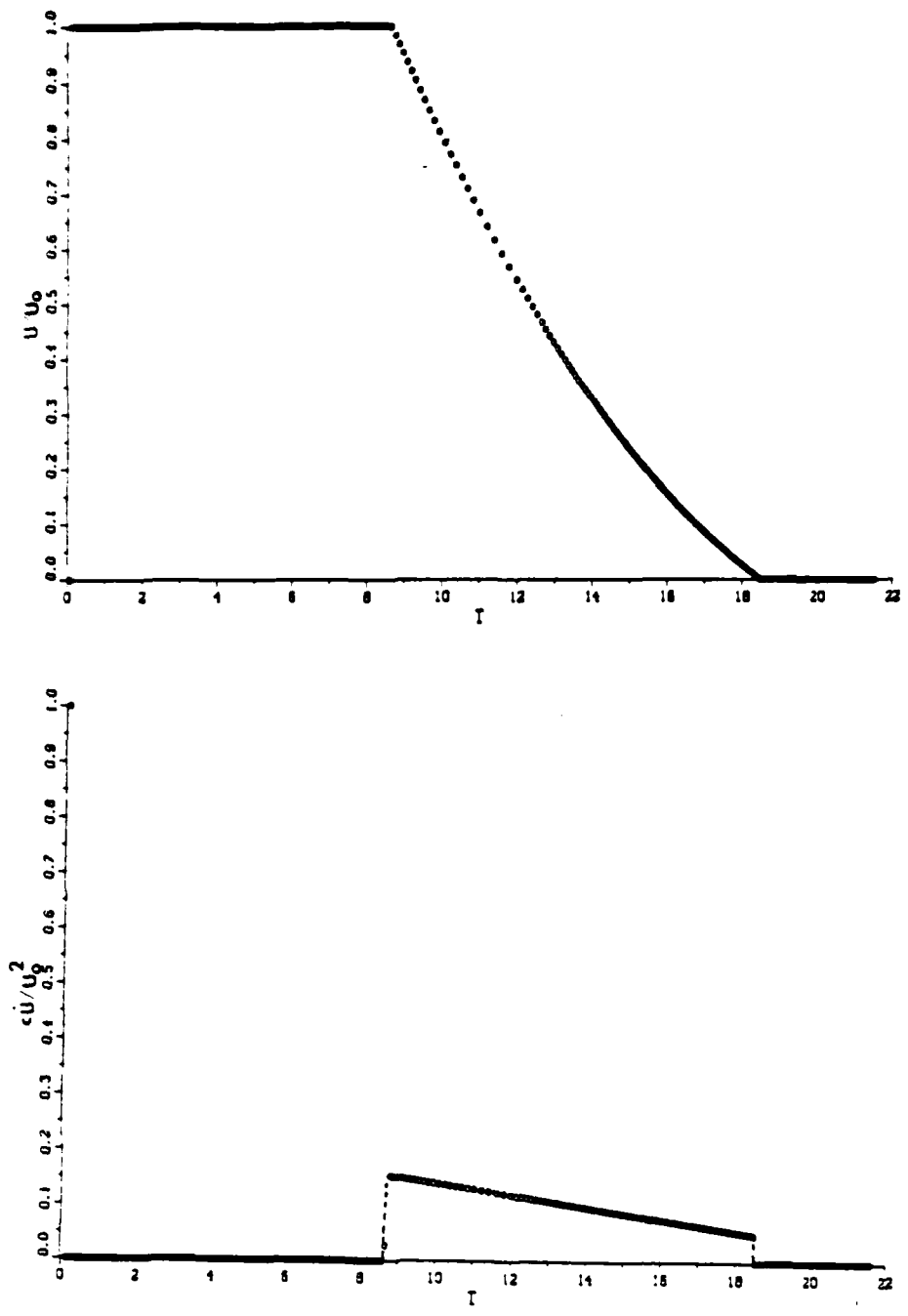
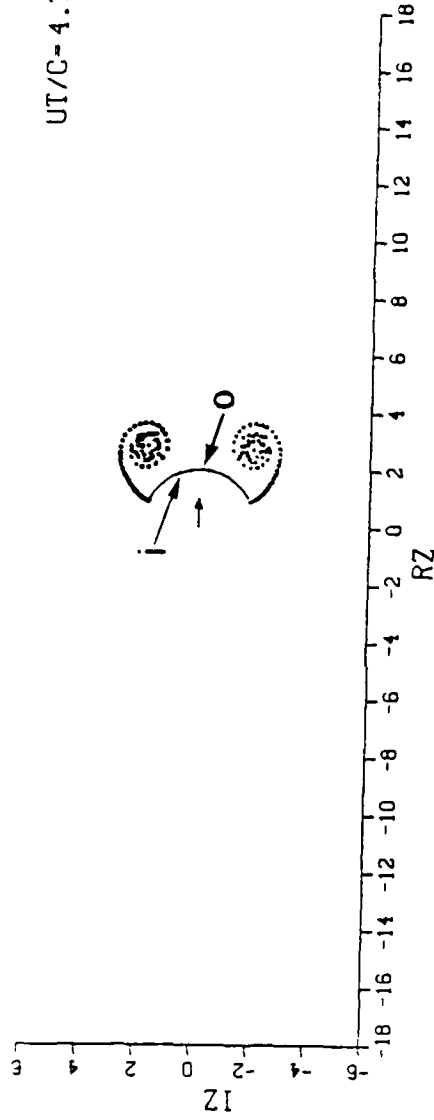


Figure 4.1 Variations of the velocity and the acceleration.

POSITION OF VORTICES

UT/C=4.35



TANGENTIAL VELOCITY

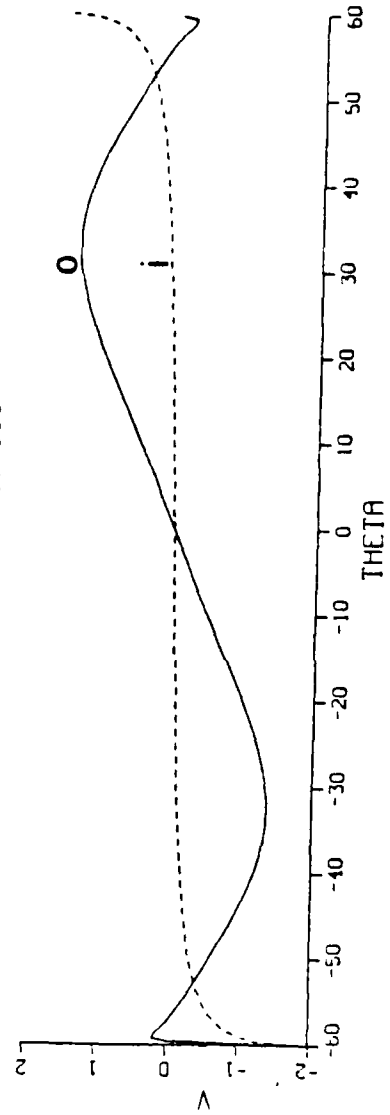


Figure 4.2 Position of vortices and tangential velocity distribution.

VELOCITY PROFILE ALONG RZ

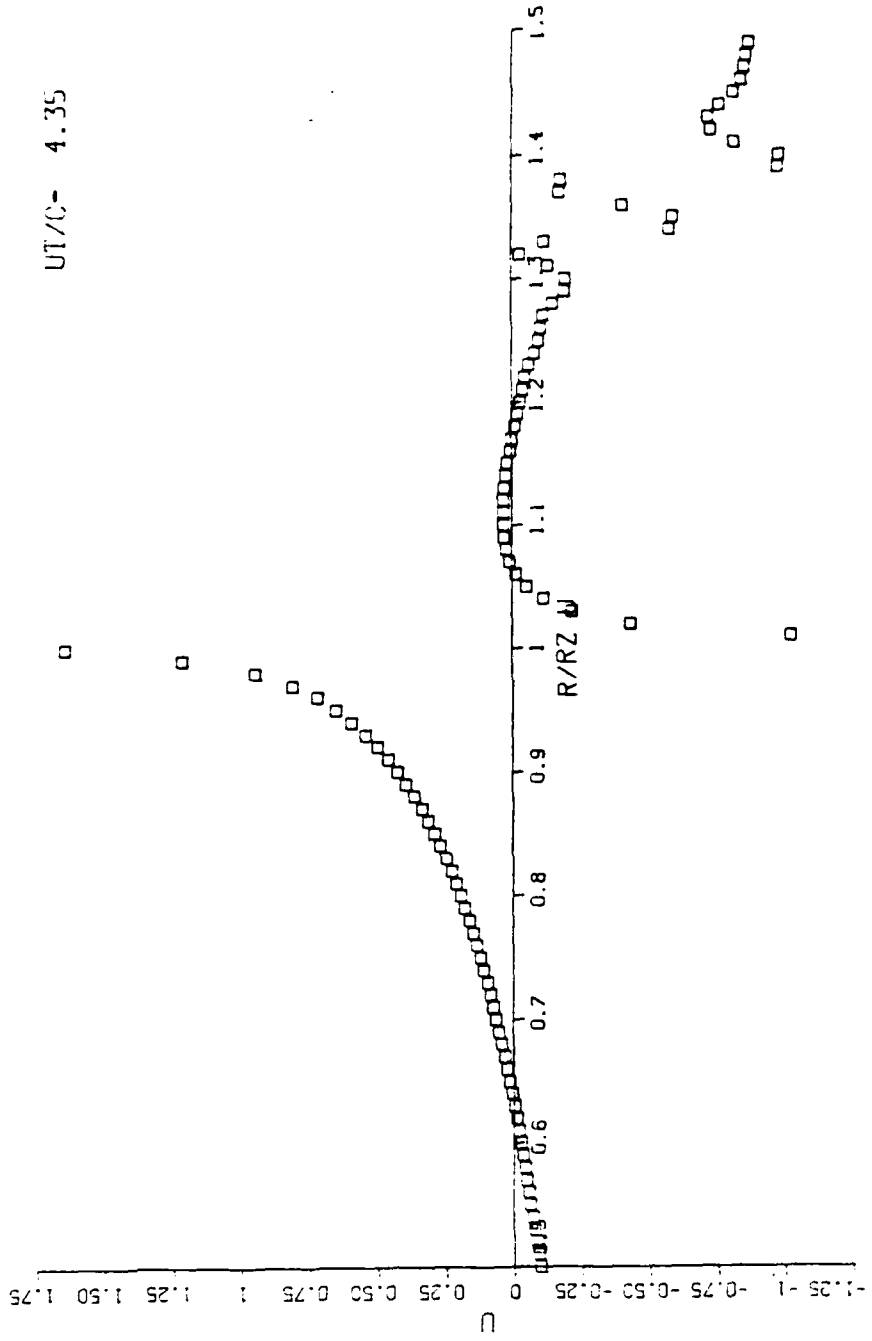
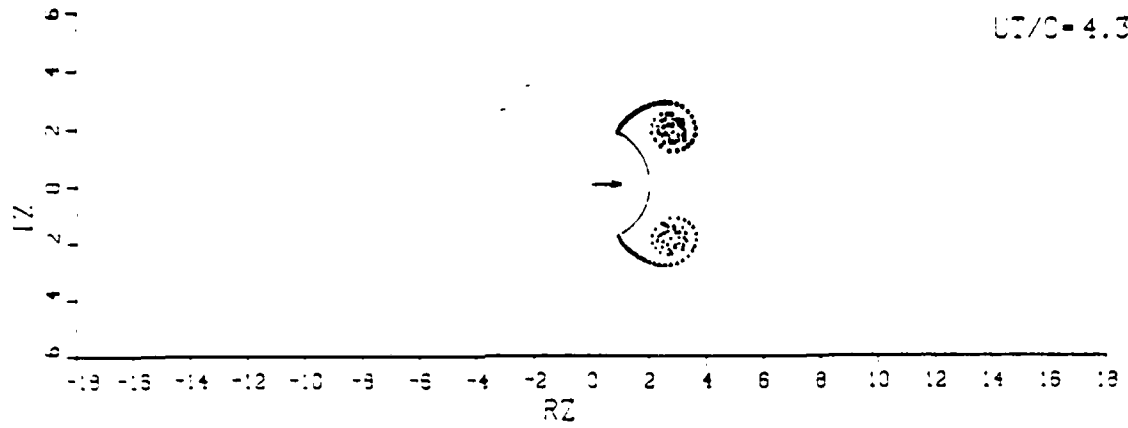


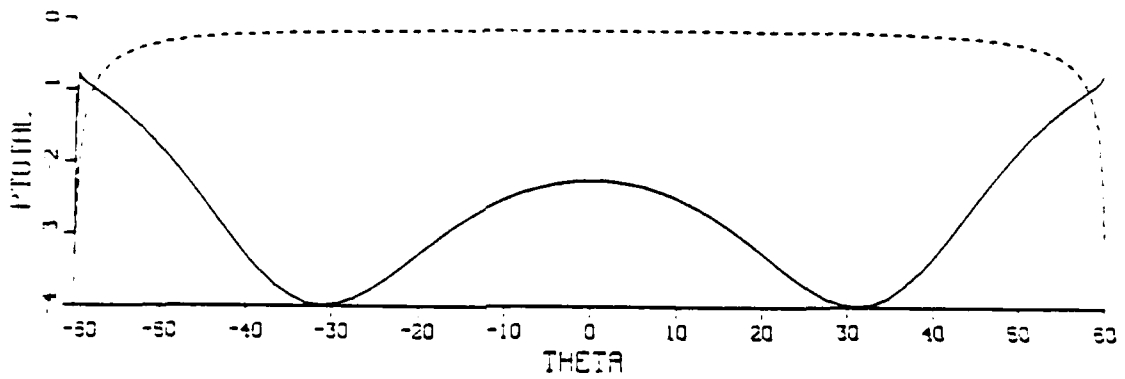
Figure 4.3 Velocity profile along the radial line passing through the tip.

POSITION OF VORTICES

UT/C=4.35



TOTAL PRESSURE



DIFFERENTIAL PRESSURE

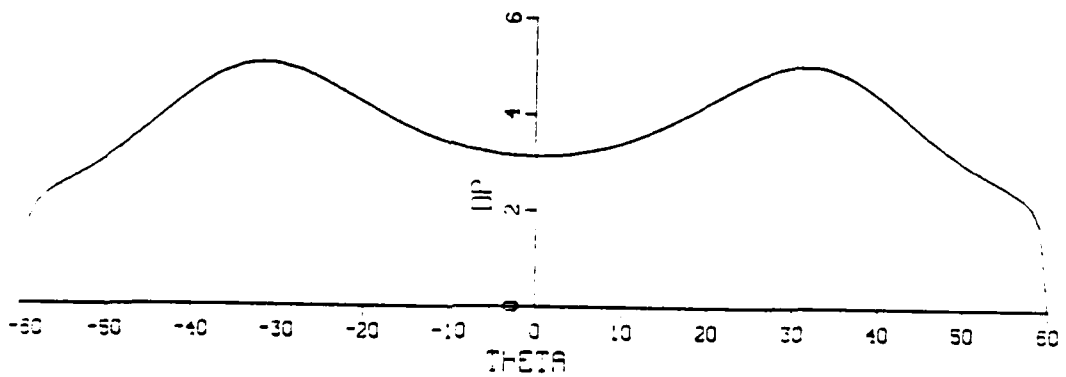


Figure 4.4 Pressure distribution on the upstream and downstream faces.

Following the onset of deceleration (see e.g., Figs. 4.5 through 4.7 at $T^* = 10.84$), the differential pressure near the axis of the camber becomes increasingly negative. The reason for this is that the deceleration of the flow brings the vortices closer to the camber. The significance of this result is that had the model been flexible (as in the case of a parachute) the central part of the camber would have collapsed as a result of the particular deceleration it is subjected to. Evidently the collapse phenomenon would not have remained symmetrical, as evidenced by field experiments with axisymmetric flexible parachute. Furthermore, it would have required the analysis of the flow about a flexible camber. It is because of this reason that in the present analysis the camber is assumed to remain rigid.

For T^* larger than about 13 (for the ambient flow under consideration), the velocities induced at the downstream edges of the camber by the large vortices moving sideways and towards the camber give rise to oppositely-signed vorticity. This, in turn, leads to the rapid growth of the secondary vortices (see e.g., Figs. 4.8 through 4.10 at $T^* = 17.86$). The secondary vortices are relatively weaker than the primary vortices partly because they have been in existence only for a short time and partly because the vorticity flux is not as large as that in the primary shear layers. Consequently, the centroid of the secondary vortices tends to orbit about the centroid of the primary vortices.

A comparison of Figs. 4.7 and 4.10 shows that the region of negative differential pressure grows with time and occupies a large central portion of the camber. In fact, the drag force acting on the camber becomes negative, as it will be seen shortly.

Figures 4.11 through 4.16 show, at suitable times, the velocity field about the camber. The rapid growth of the wake during the period of steady uniform flow is exhibited in Figs. 4.11 and 4.12. Figure 4.13 nearly corresponds to the time at which the deceleration is imposed on the flow. Figures 4.14 through 4.16 show clearly the backward motion of the primary vortices and the rapid growth of the secondary vortices. It is seen from Fig. 4.16 that the fluid motion is entirely due to the motion of the vortices in the flow field. The two vortices on each side of the camber form a counter-rotating couple and remove themselves rapidly from the field under the influence of their mutual induction velocity. Subsequently, the absolute value of the differential pressure begins to decrease. Eventually, the differential pressure reduces to zero everywhere on the camber as the conditions approach to that of a body in a fluid at rest.

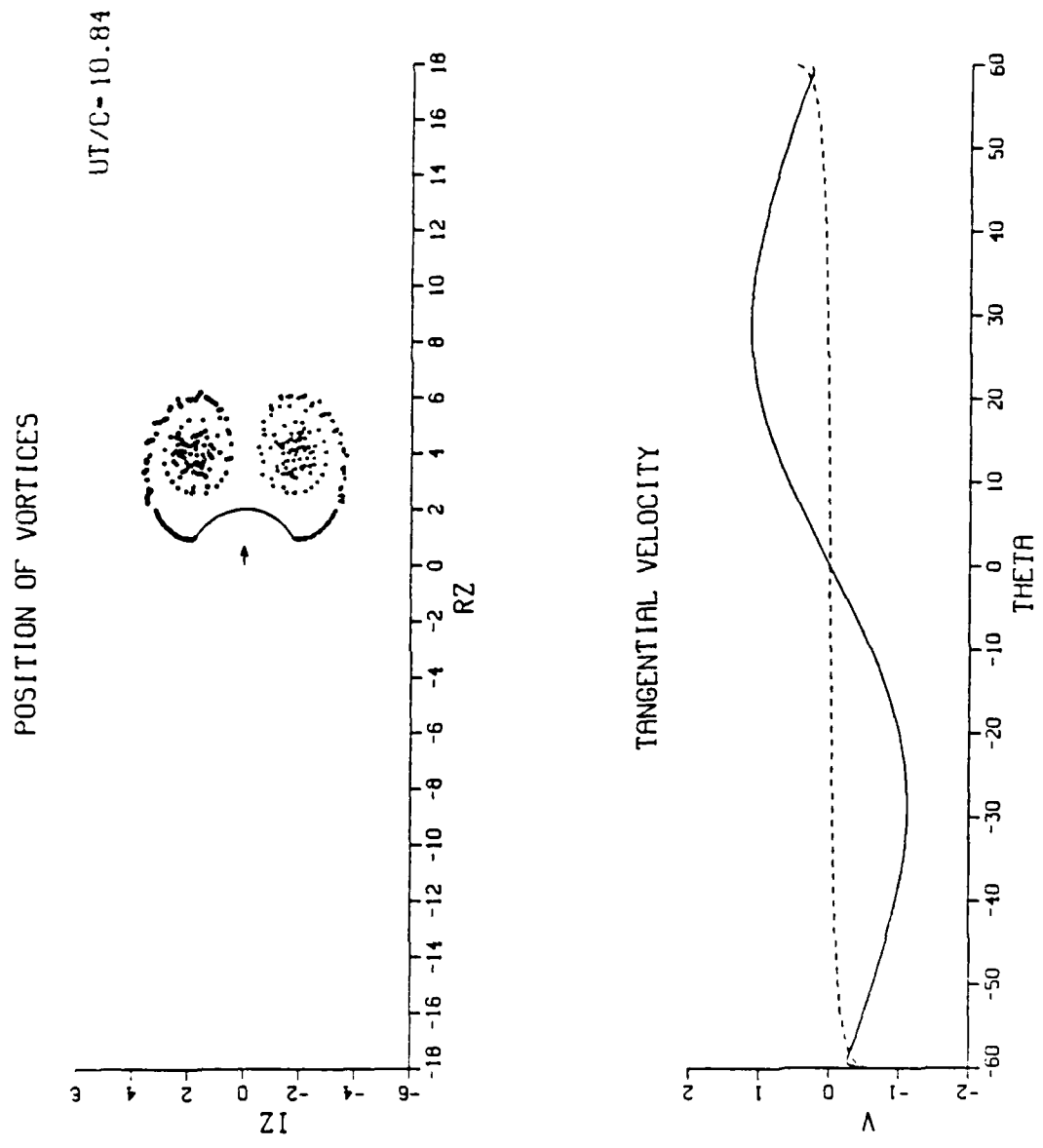


Figure 4.5 Tangential velocity at $T^* = 10.84$.

VELOCITY PROFILE ALONG RZ

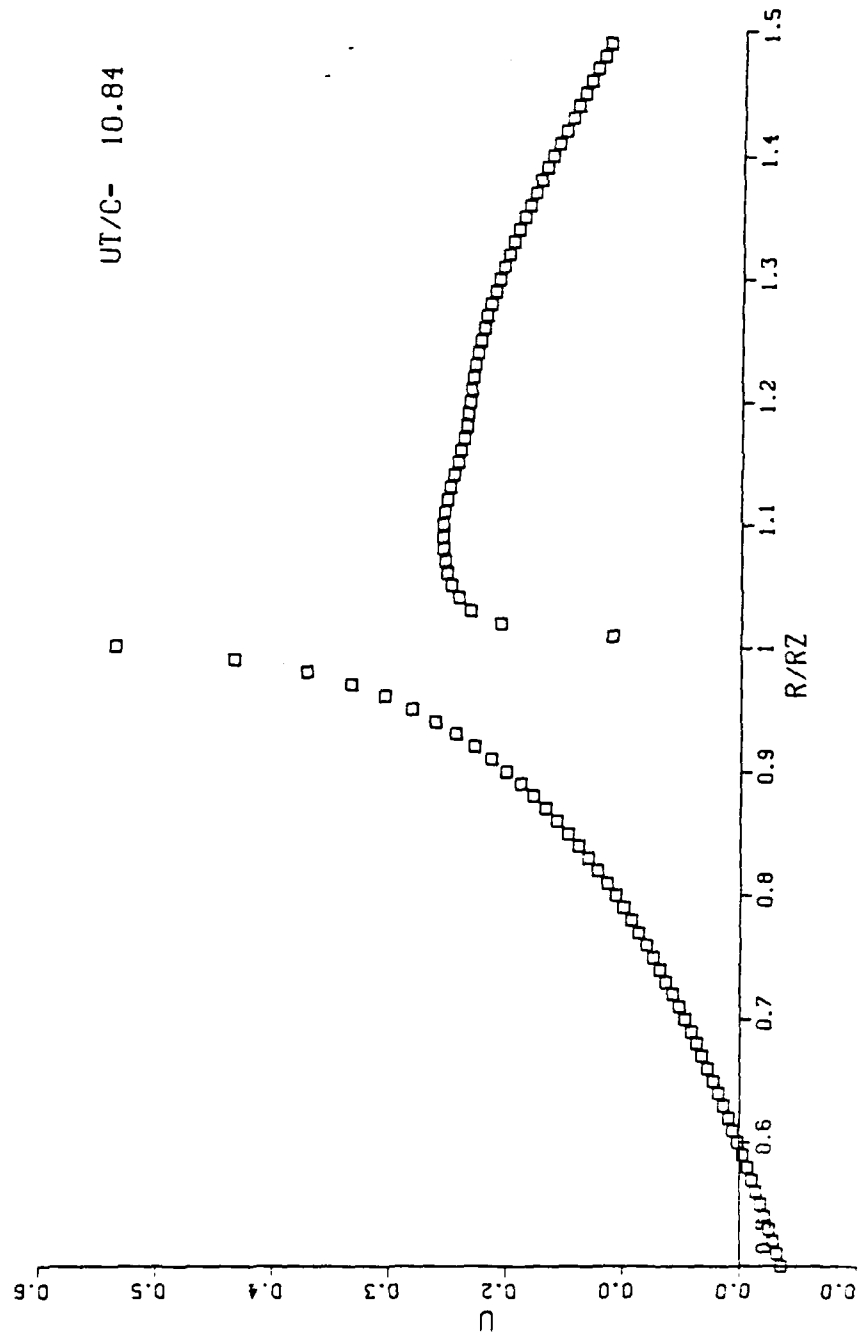
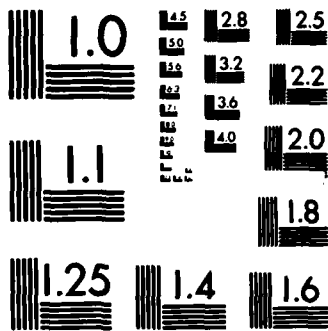


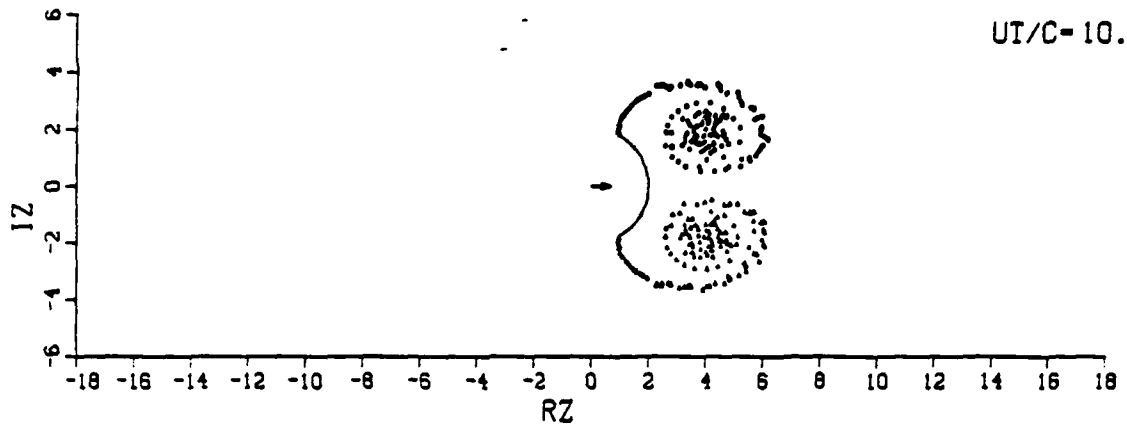
Figure 4.6 Tip velocity at $T^* = 10.84$.



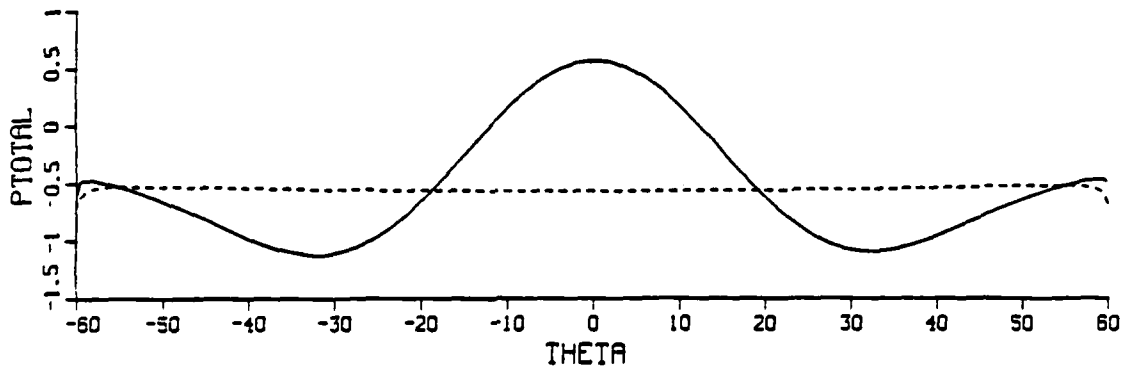
MICROCOPY RESOLUTION TEST CHART
NATIONAL BUREAU OF STANDARDS-1963-A

POSITION OF VORTICES

UT/C-10.84



TOTAL PRESSURE



DIFFERENTIAL PRESSURE

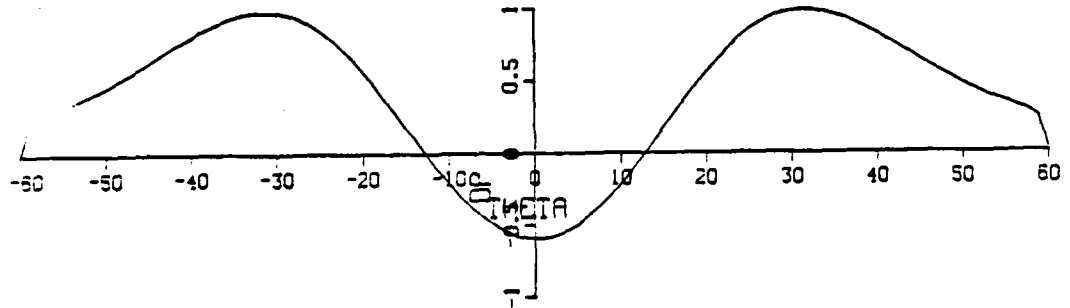


Figure 4.7 Pressure distribution at $T^* = 10.84$.

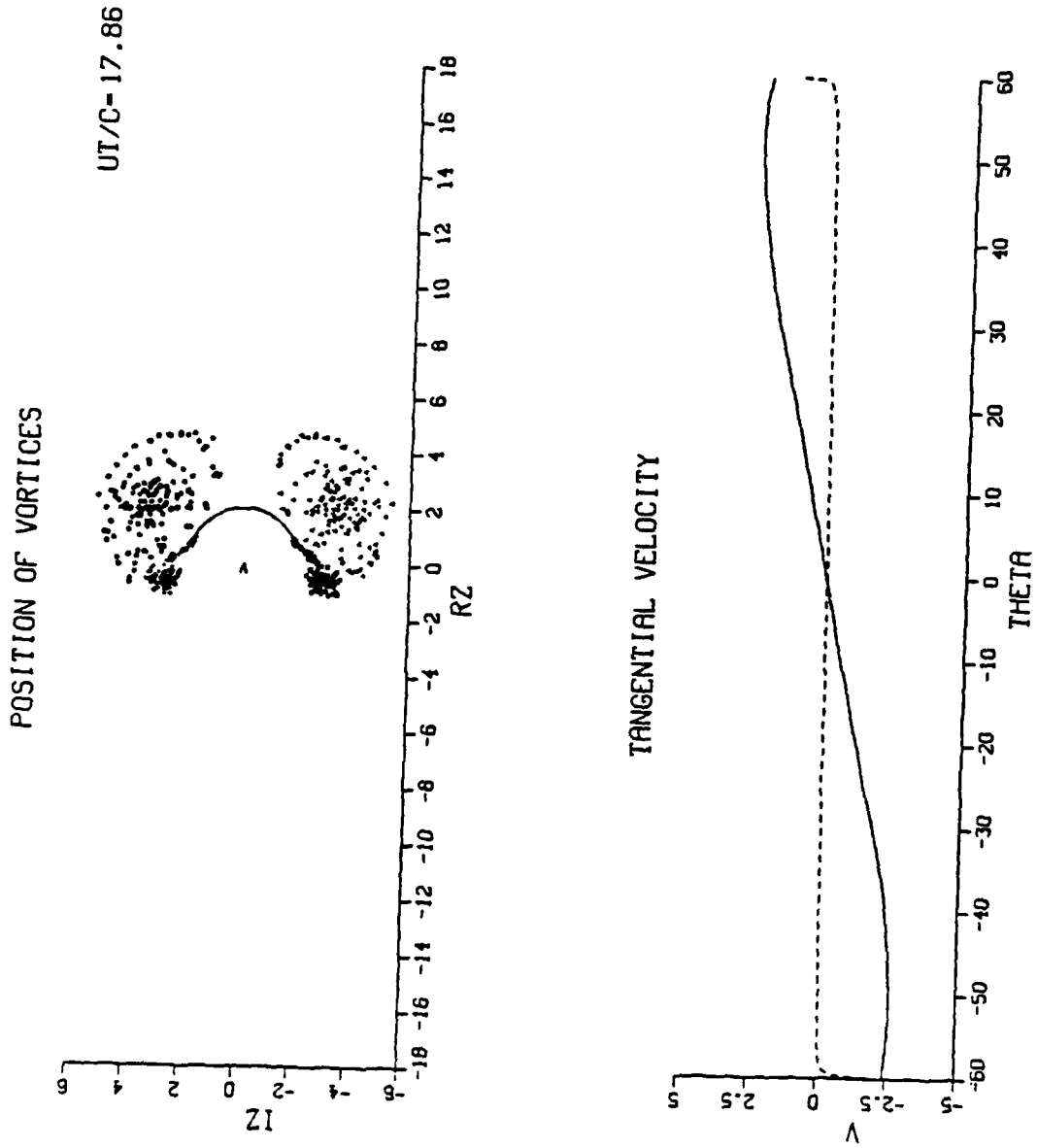


Figure 4.8 Tangential velocity at $T^* = 17.86$.

VELOCITY PROFILE ALONG RZ

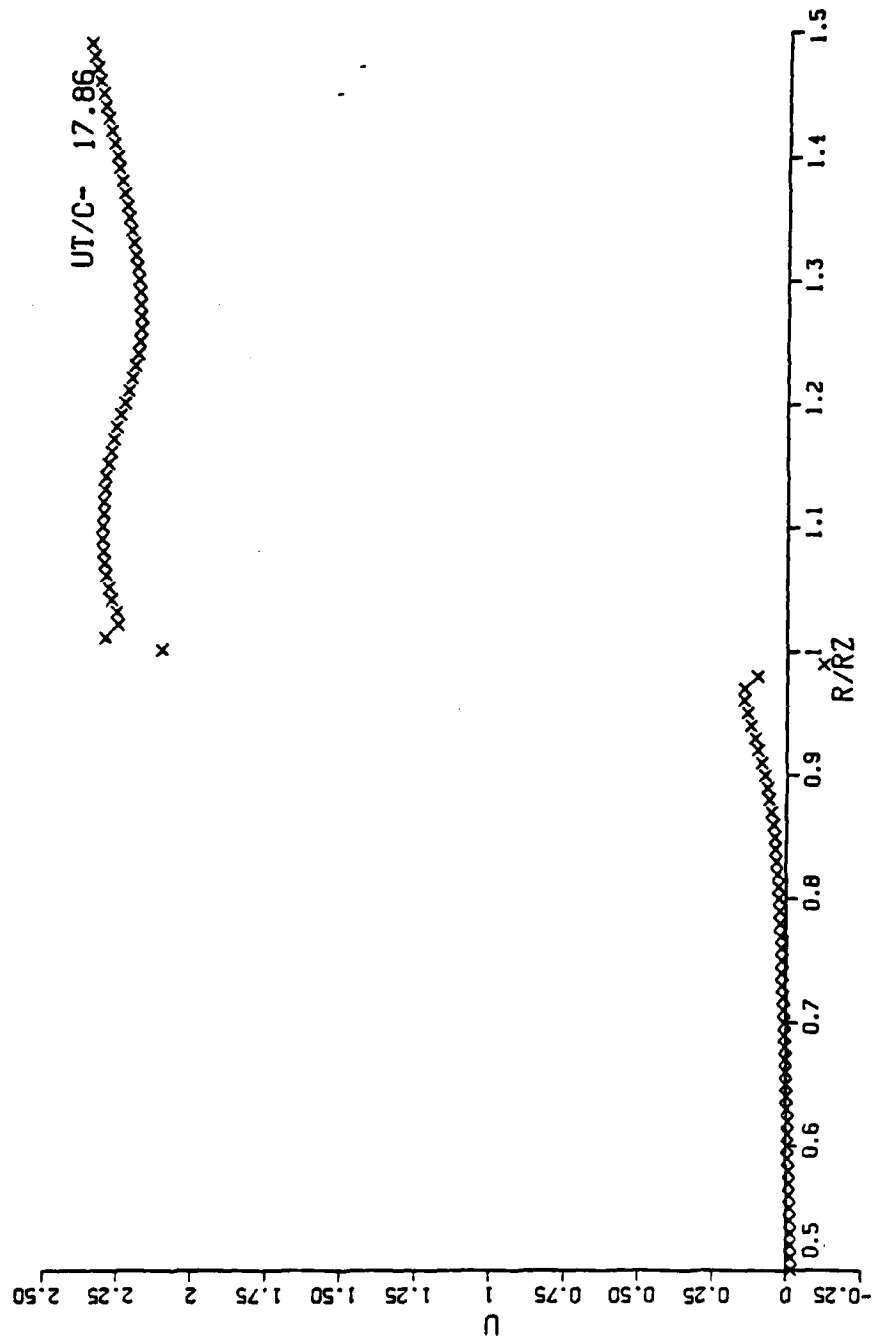
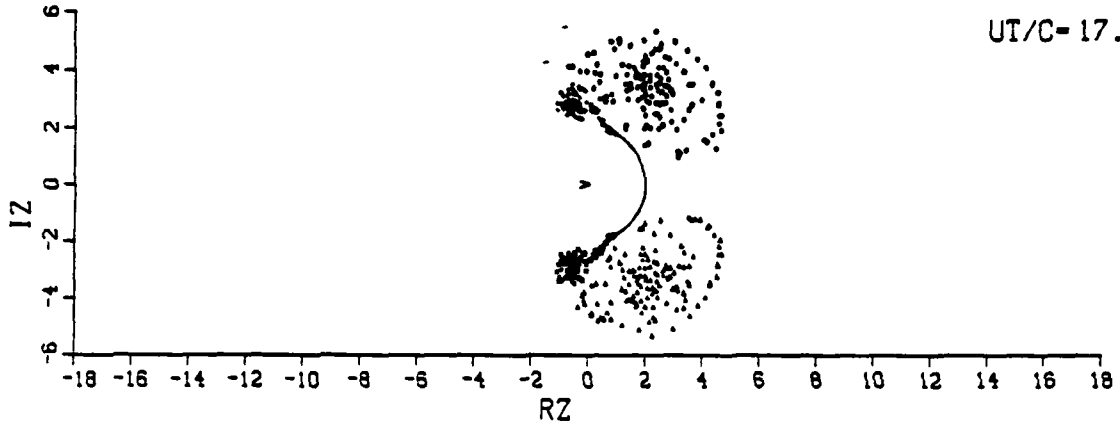


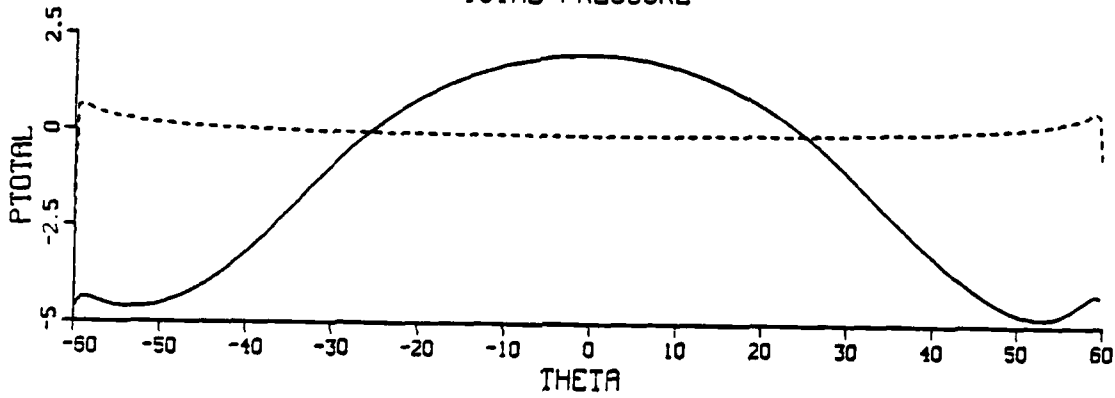
Figure 4.9 Tip velocity at $T^* = 17.86$.

POSITION OF VORTICES

UT/C-17.86



TOTAL PRESSURE



DIFFERENTIAL PRESSURE

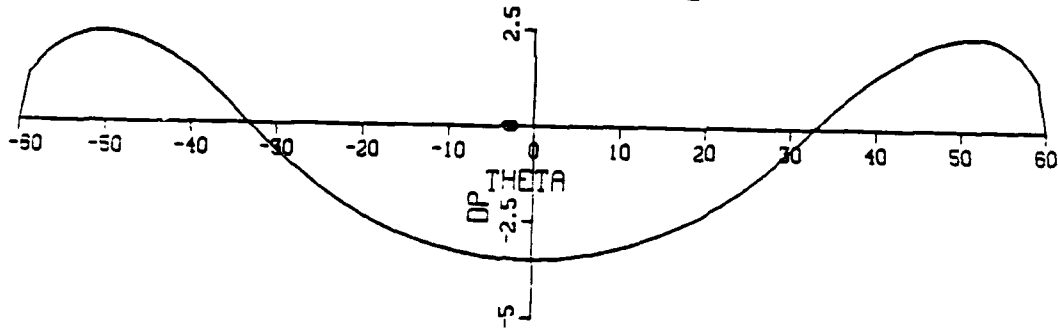


Figure 4.10 Pressure distribution at $T^* = 17.86$.

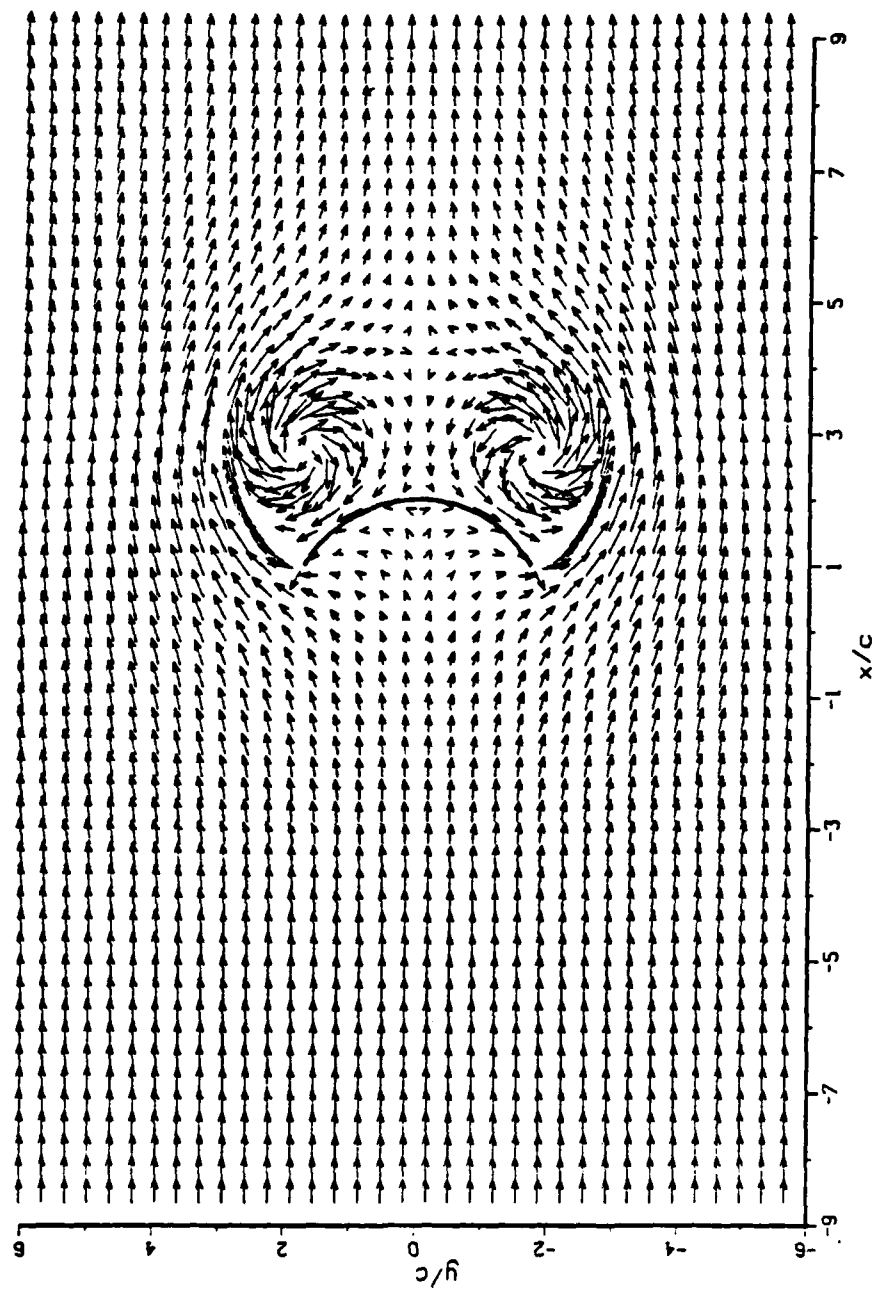


Figure 4.11 The velocity field about the camber at $T^* = 4.35$.

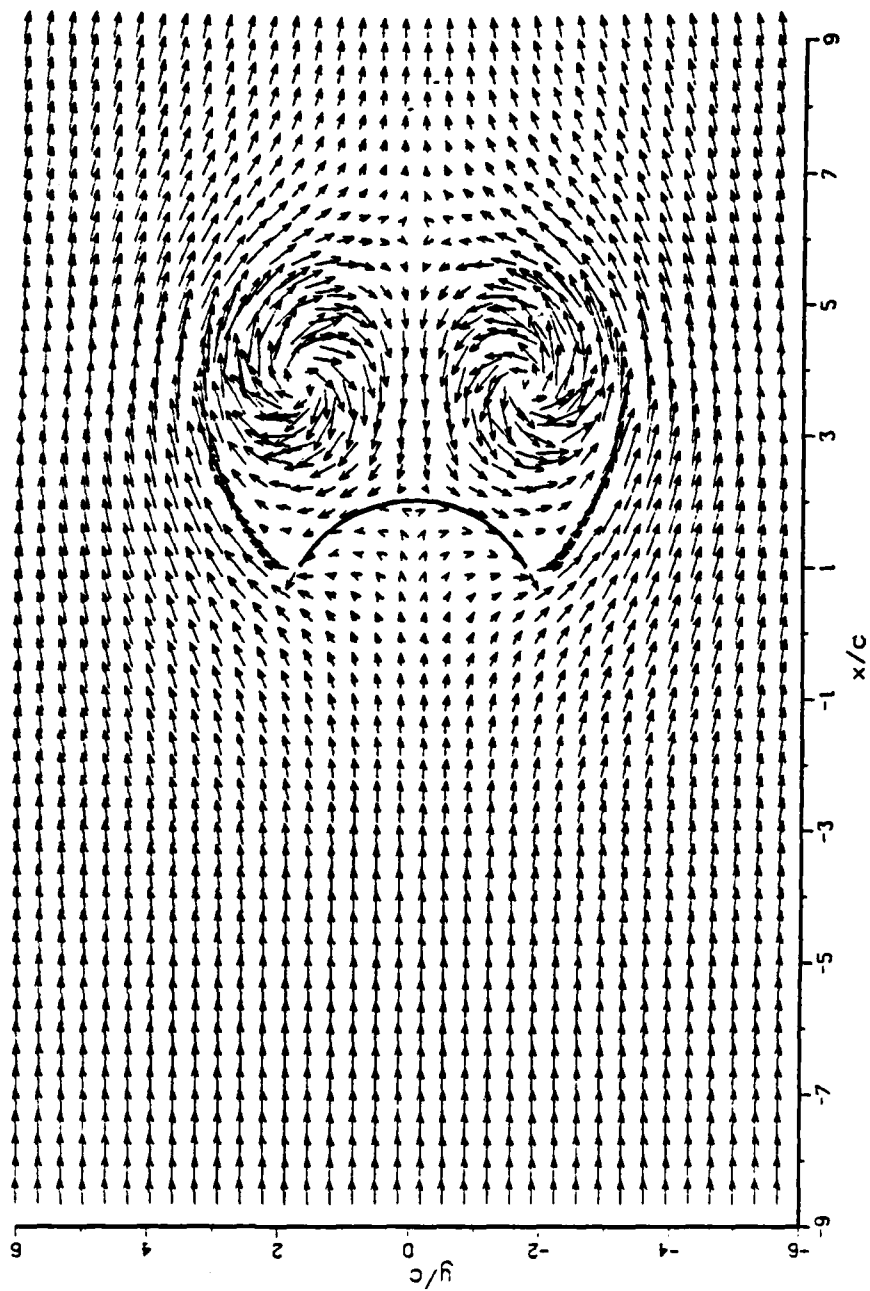


Figure 4.12 The velocity field about the camber at $T^* = 6.05$.

The remainder of the discussion of the results will deal with the variation with time of the tip velocities and the drag and lift forces.

Figures 4.17 and 4.18 show the velocities V_1 and V_2 as a function of T^* . The tip velocity V_1 decreases from an initially large value of about 3.5 to a nearly constant value of about 1.5 just prior to the onset of deceleration. Subsequently, V_1 decreases rapidly during the period of deceleration and prior to the inception of the secondary separation. Then V_1 increases to about 2 because of the backward motion of the large vortices near the tips of the camber. Finally, V_1 decreases once again as the primary and secondary vortices move sideways and away from the tips of the camber due to their mutual induction (see Fig. 4.16).

The variation of V_2 with T^* is significant only during two, relatively short, time intervals: at the start of the motion and at the start of the deceleration. These are the periods during which the vorticity flux changes rapidly in order to maintain the Kutta condition. During the remainder of time V_2 is negligibly small, as expected on the basis of the pioneering experiments of Fage and Johansen (1928) with steady flow over various types of bluff bodies.

Figures 4.19 and 4.20 show the variation of the drag and lift coefficients as a function of time. The former is based on the integration of pressure and the latter on the rate of change of impulse. The drag coefficient calculated through the use of the rate of change of impulse is somewhat larger than that obtained through the integration of the instantaneous differential-pressure distribution. This is due to the fact that the impulse expression includes the rate of change of circulation between two successive time steps whereas the pressure expression does not. It is a well-known fact that in real fluids the memory of the fluid resides in its vorticity. Whereas in inviscid flows there is no memory and the dynamic characteristics of the flow (pressures and forces) are functions of only the instantaneous state of the flow. The analysis presented herein is for an inviscid fluid even though the phenomenon concerns the motion of a real fluid. The question of whether the rate of change of circulation should be included or excluded in the discrete vortex analysis (first discussed by Sarpkaya in 1968) is an unsettled issue. It appears that only the comparisons with experiments can clarify the question.

Figures 4.19 and 4.20 also show that C_d rises rapidly (due to the rapid accumulation of vorticity in the growing vortices) and begins to decrease as the vortices develop under the influence of a constant ambient velocity. Then the force

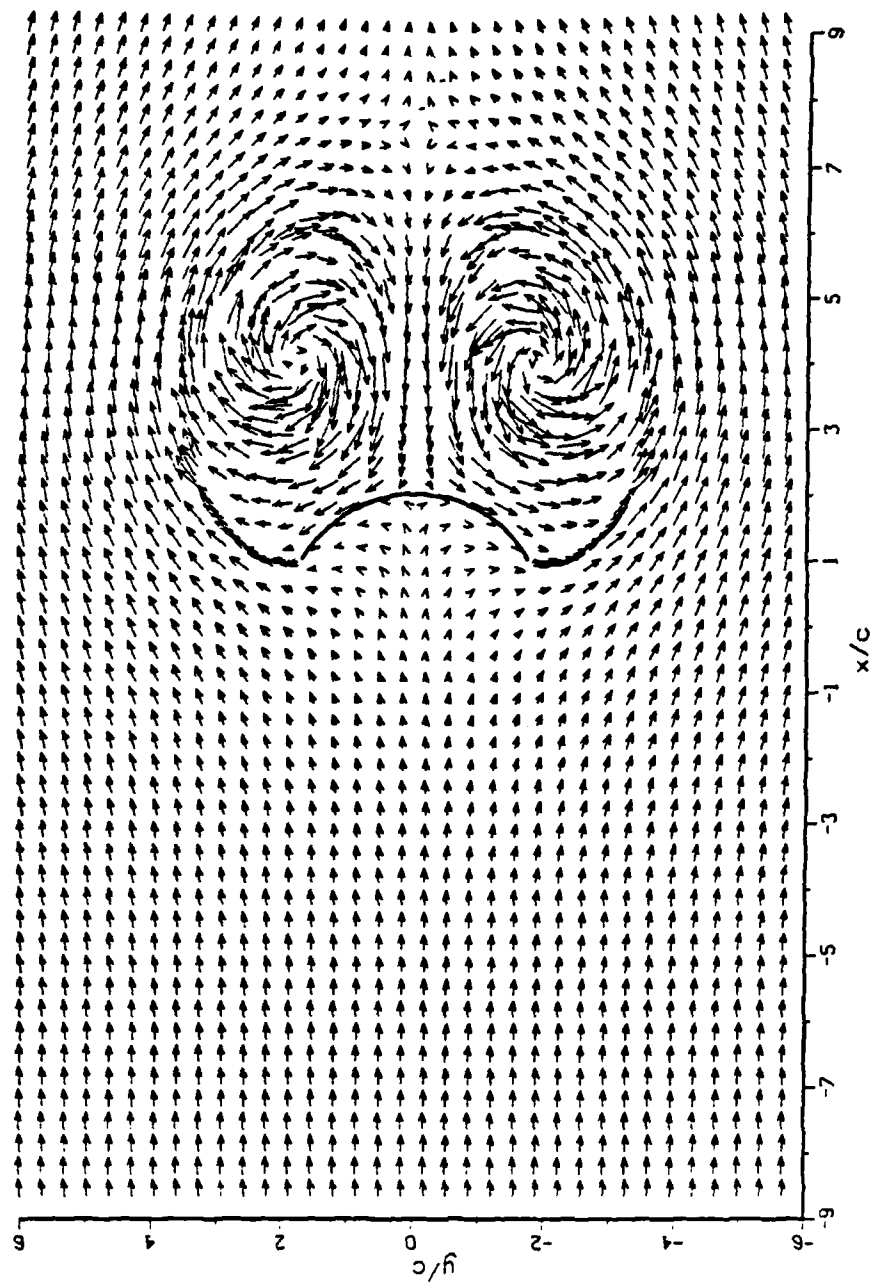


Figure 4.13 The velocity field about the camber at $T^* = 8.55$.

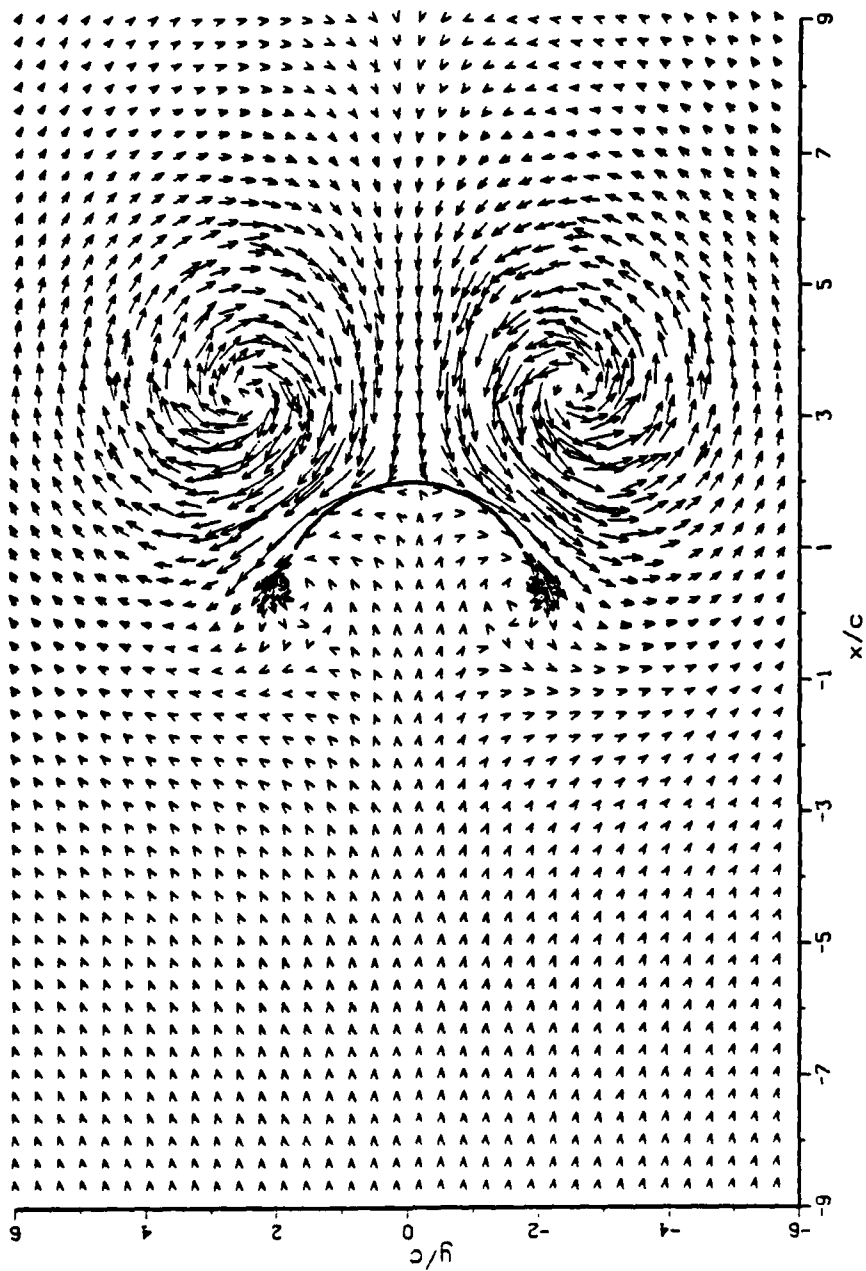


Figure 4.14 The velocity field about the camber at $T^* = 14.20$.

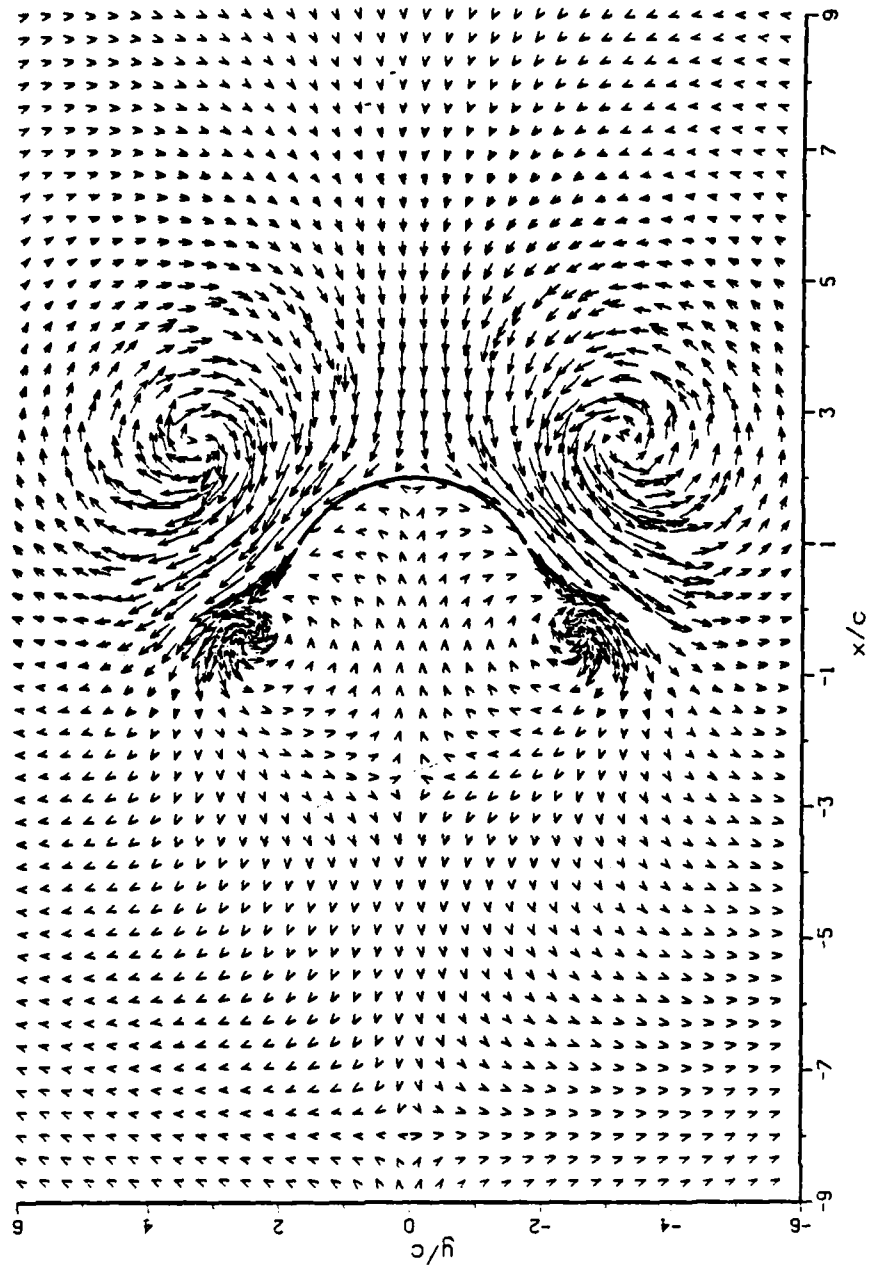


Figure 4.15 The velocity field about the camber at $T^* = 16.30$.

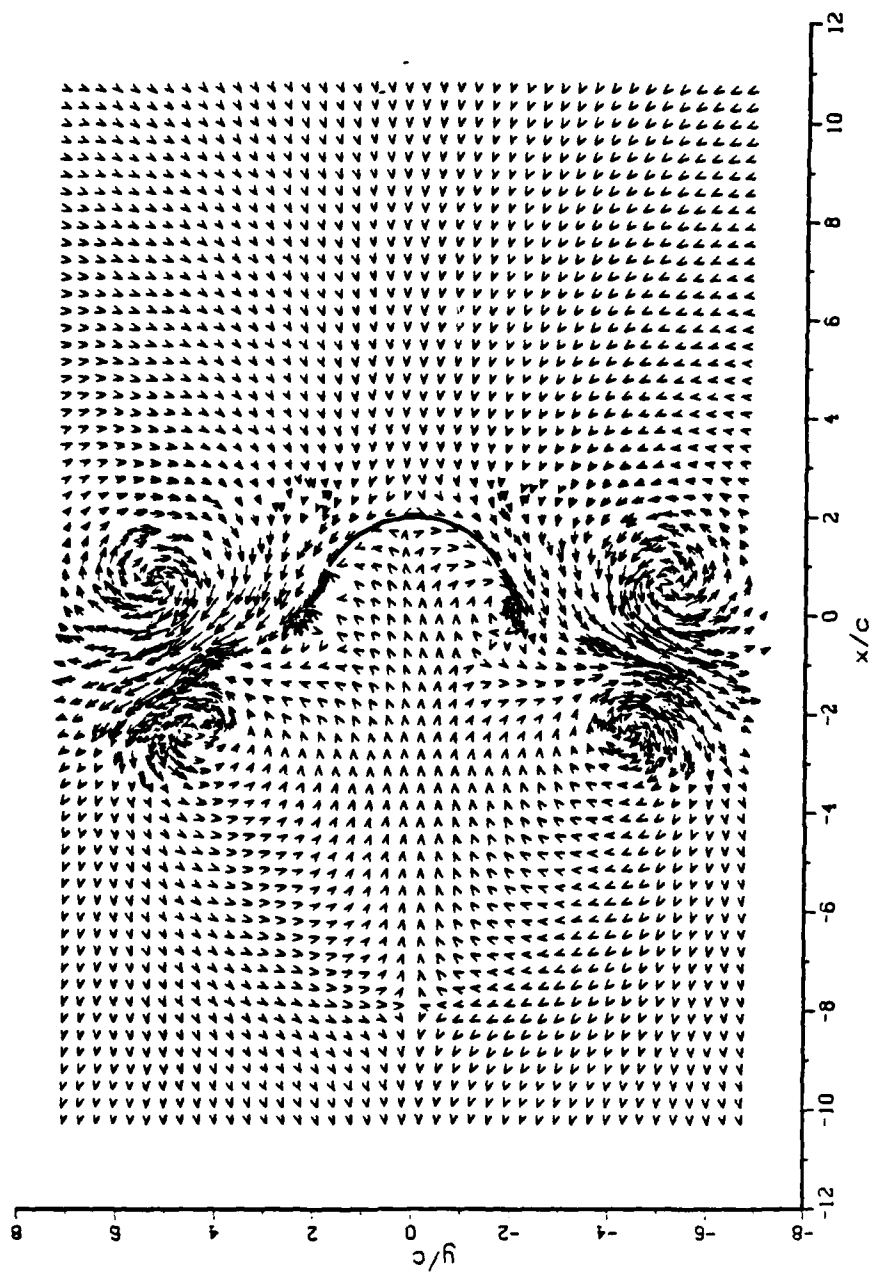


Figure 4.16 The velocity field about the camber at $T^* = 21.50$.

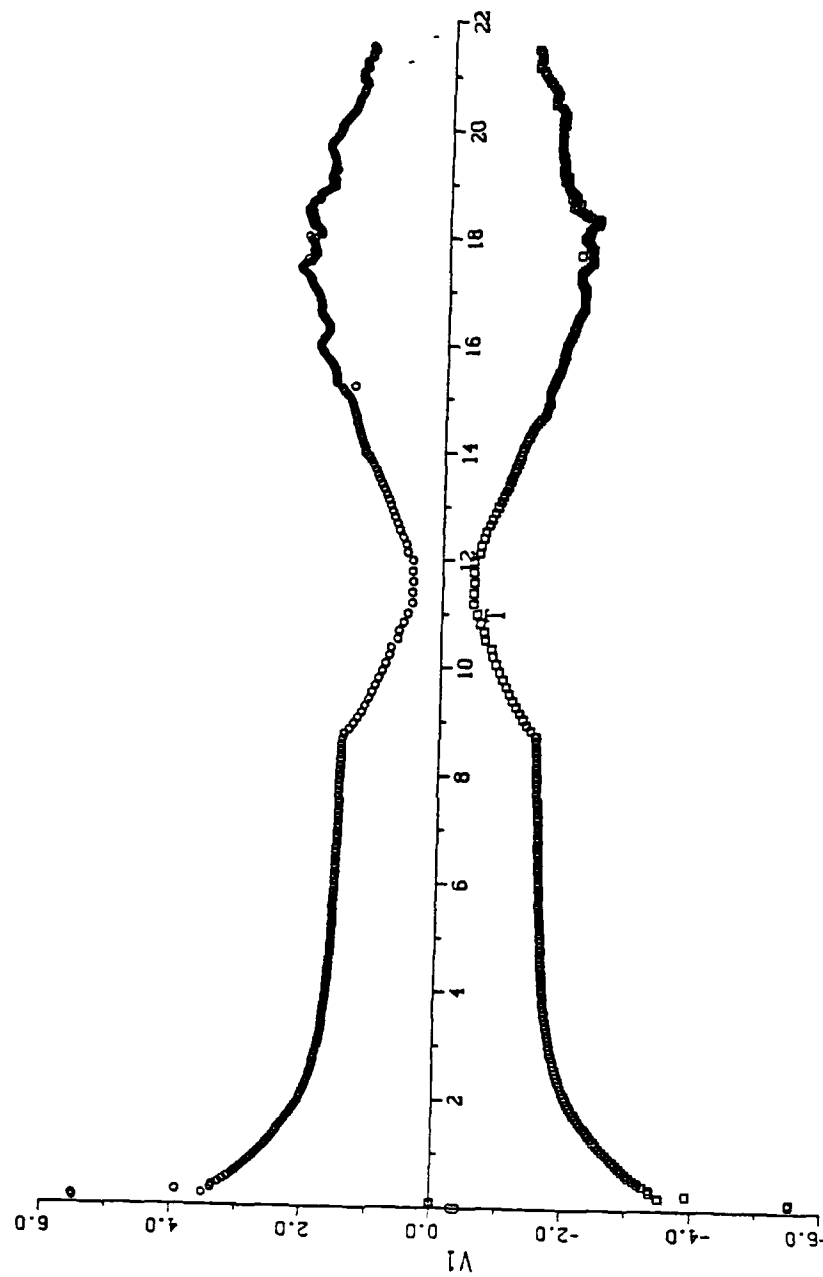


Figure 4.17 Variation of V_1 with time.

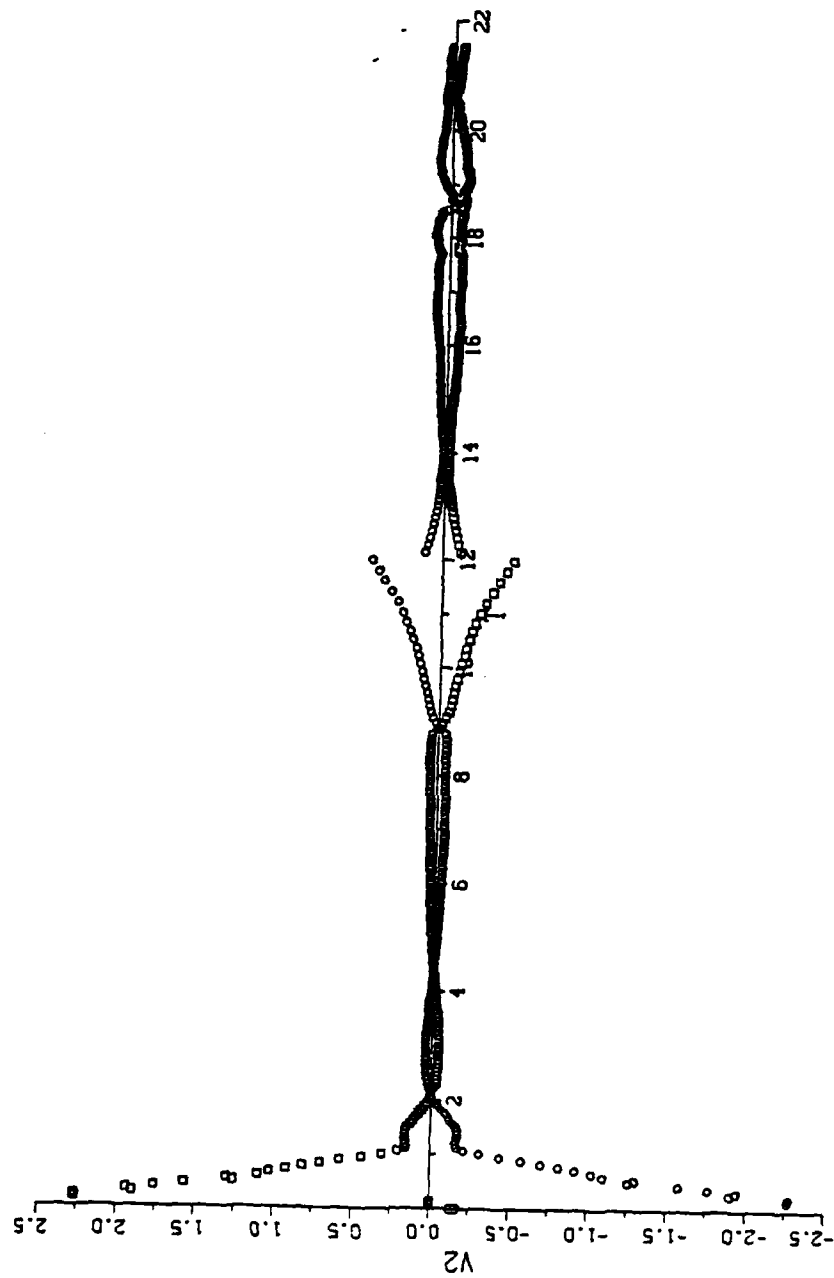


Figure 4.18 Variation of V_2 with time.

decreases sharply at the onset of deceleration and goes through zero near the middle of the deceleration period ($T^* = 11$). The force acquires its largest negative value towards the end of the deceleration period. Subsequently, the force gradually decreases to zero.

Also shown in Figs. 4.19 and 4.20 is the variation of the lift force. It is negligible even in the later stages of the motion. This is primarily due to the fact that there is not sufficient time for the development of alternate vortex shedding either during the period of steady flow or during the period of rapid deceleration.

Figure 4.21 shows a comparison of the calculated (through pressure integration) and measured drag coefficients. In general the agreement between the calculated and the measured drag coefficient is quite good. In the time intervals between 13 and 16 and between 19 and 22, the calculated C_d is somewhat larger. The reason for this is as follows. In the said time intervals the drag coefficient is relatively small and the viscous effects are relatively important in dissipating the vortices. This is not taken into consideration in the numerical analysis. It is possible to introduce a small artificial reduction in circulation in order to bring the calculated and measured values into closer agreement. This has been avoided in the present analysis in order to keep the discrete vortex analysis as pure and simple as possible. Figure 4.21 also shows that the calculation of the drag coefficient through the integration of pressure is superior to that through the use of the rate of change of impulse.

Finally, a comparison is made between the calculated and photographed flow fields at corresponding times. Figures 4.22 through 4.24 show at times $T^* = 6.05$, 8.55 and 16.30 the flow in the immediate vicinity of the camber (plotted to the same scale). shows that the agreement between the calculated and observed flow fields is indeed very good.

B. CONCLUDING REMARKS

The results presented in this section have shown that the discrete vortex model can be used with confidence to predict the evolution of the wake about a cambered plate immersed in a an arbitrary time-dependent flow. The evolution of the wake is remarkably similar (including the formation of the secondary vortices) to that obtained in flow visualization experiments. The drag coefficients resulting from the analysis and experiments agree reasonably well. This agreement can be improved with the introduction of a small circulation dissipation. The drag coefficient calculated through the integration of the instantaneous pressure distribution agrees more closely with that

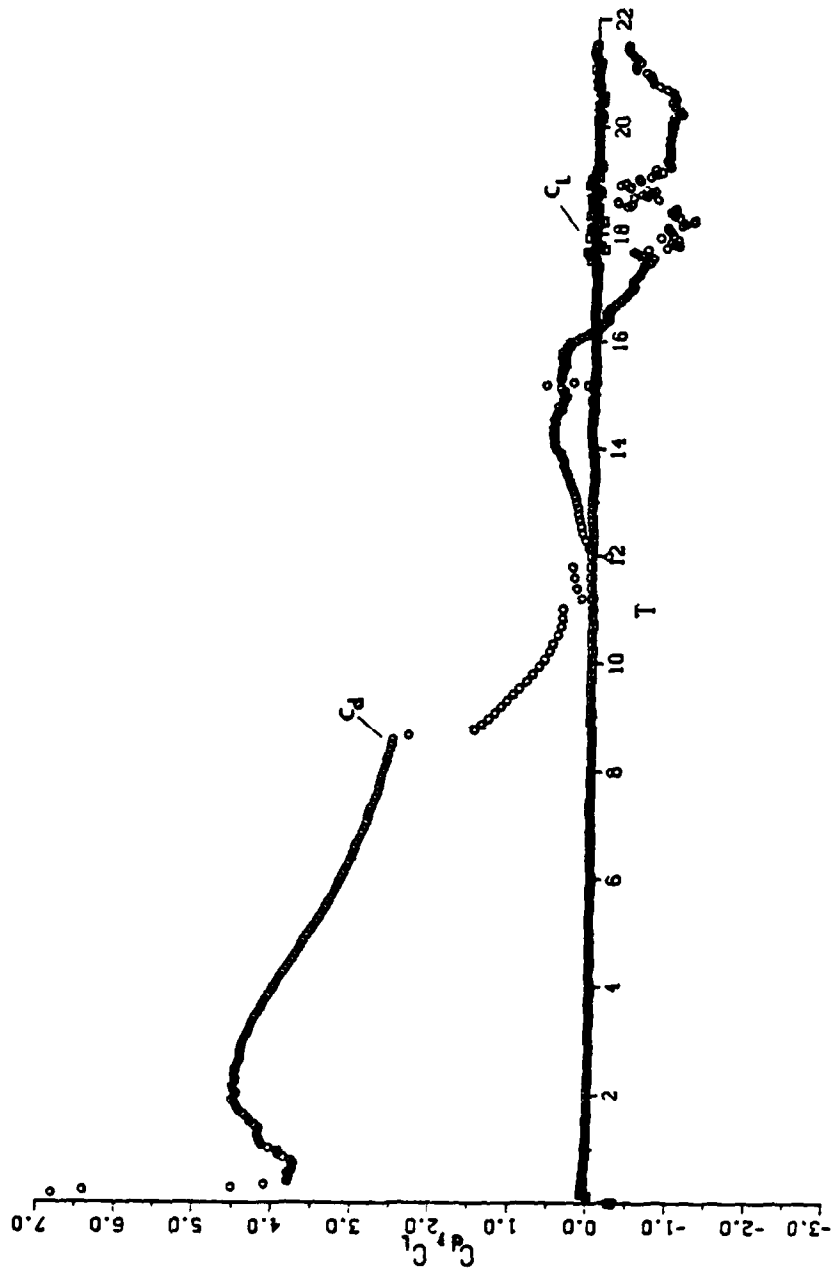


Figure 4.19 Drag coefficient calculated from pressure integration.

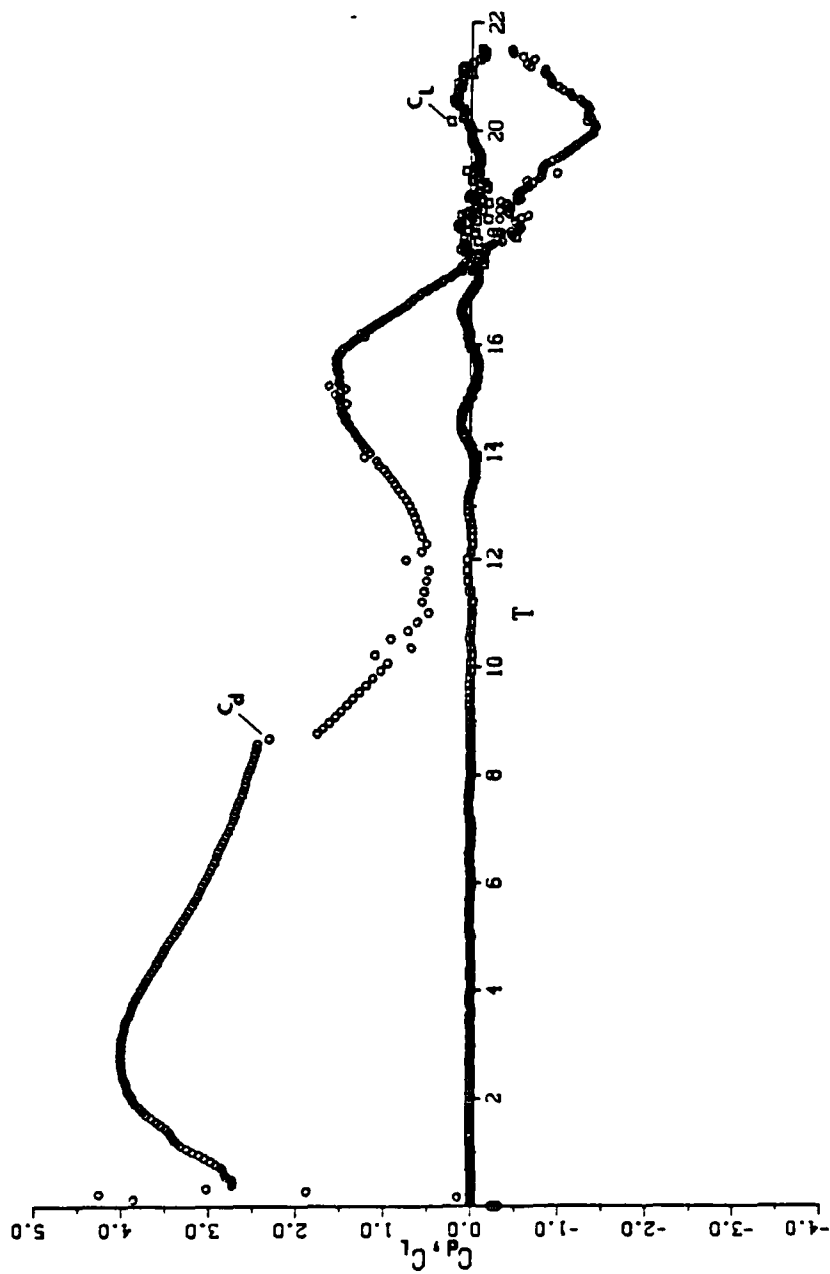


Figure 4.20 Drag coefficient calculated from impulse expression.

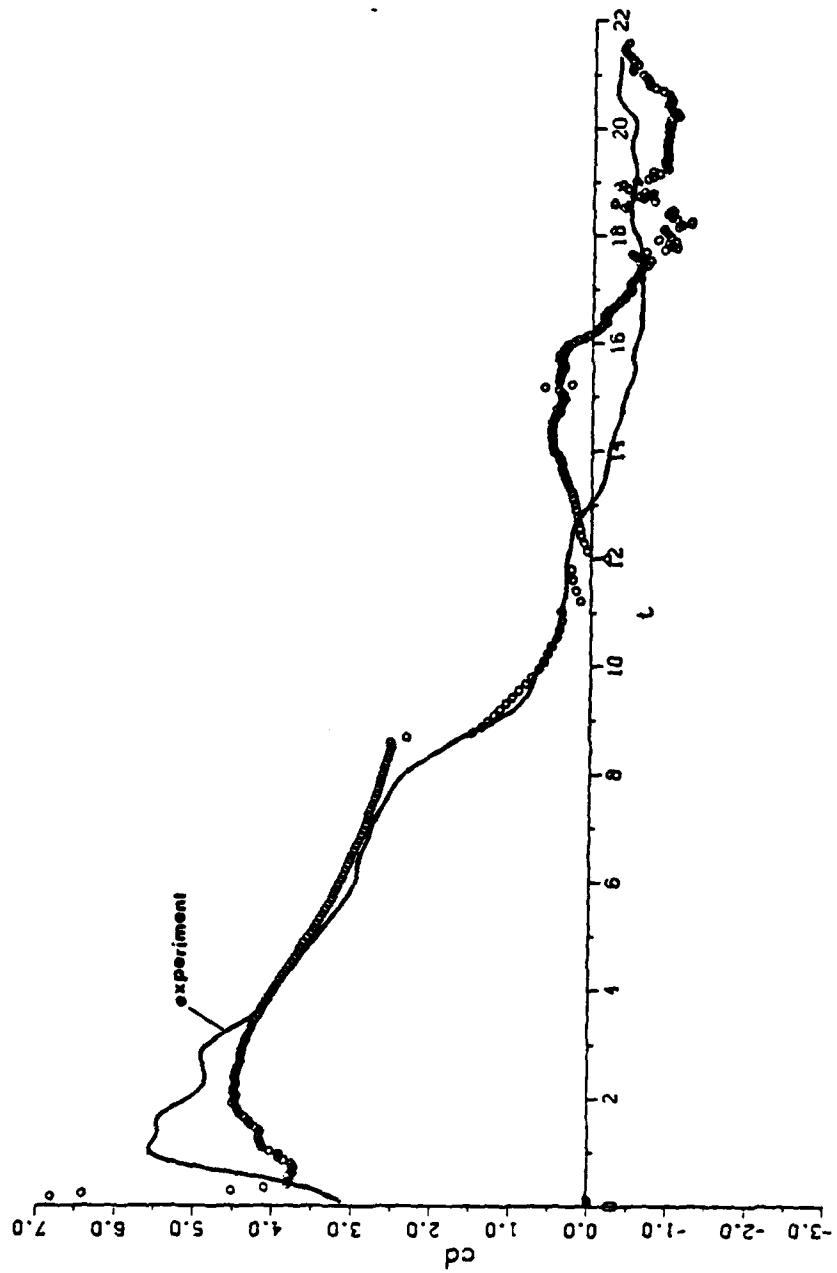


Figure 4.21 Calculated and measured drag coefficients.

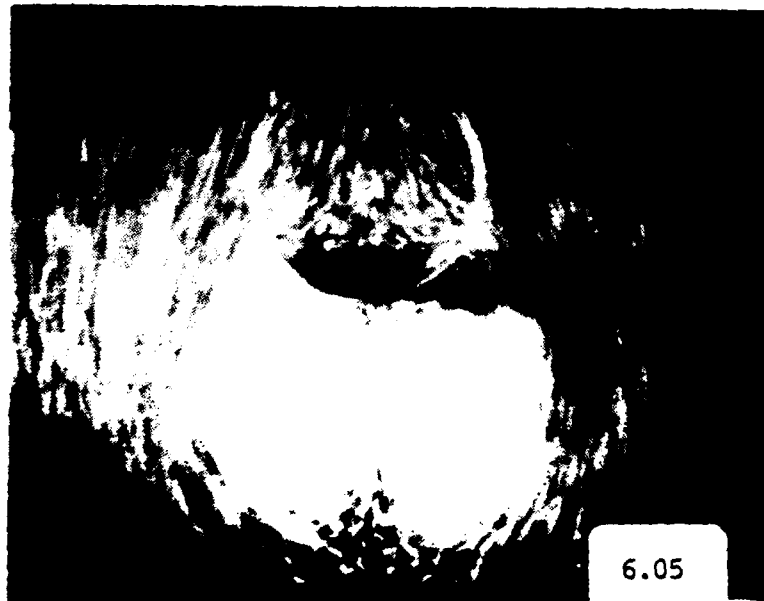
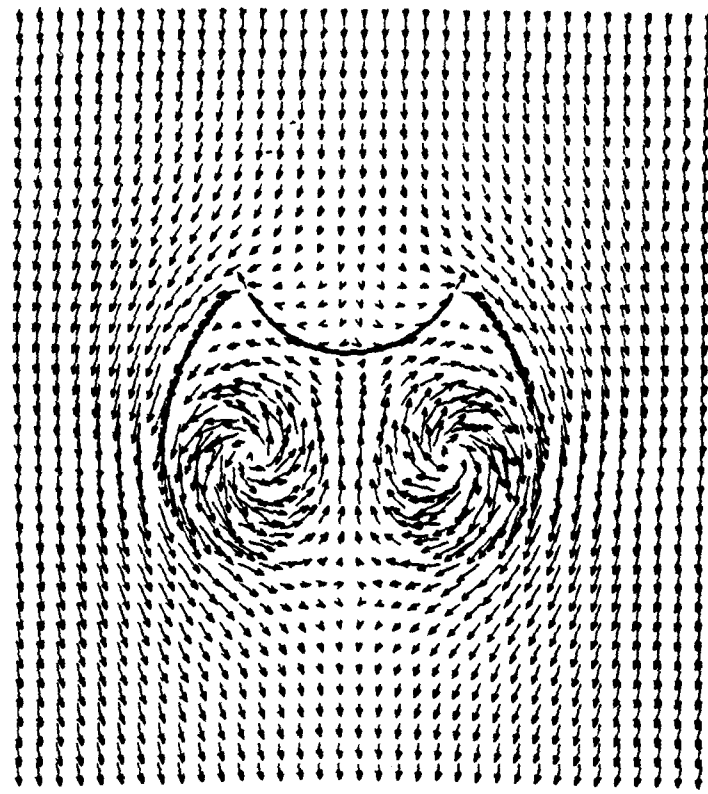


Figure 4.22 Comparison of flow fields at $T^* = 6.05$.

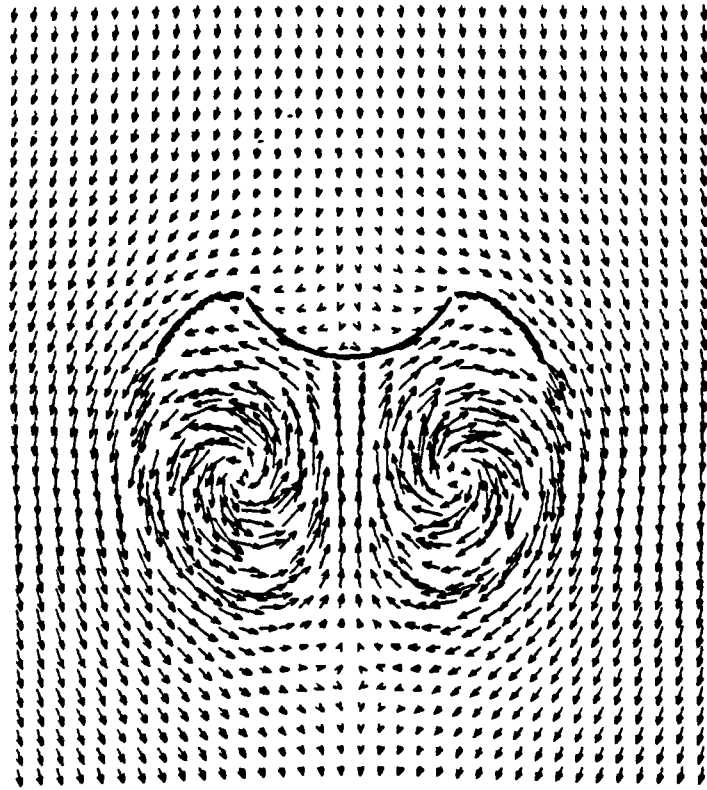


Figure 4.23 Comparison of flow fields at $T^* = 8.55$.

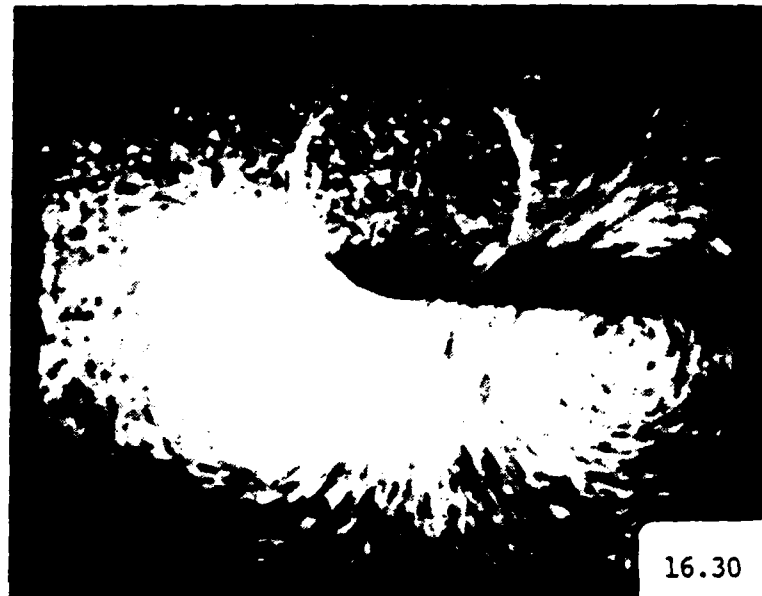
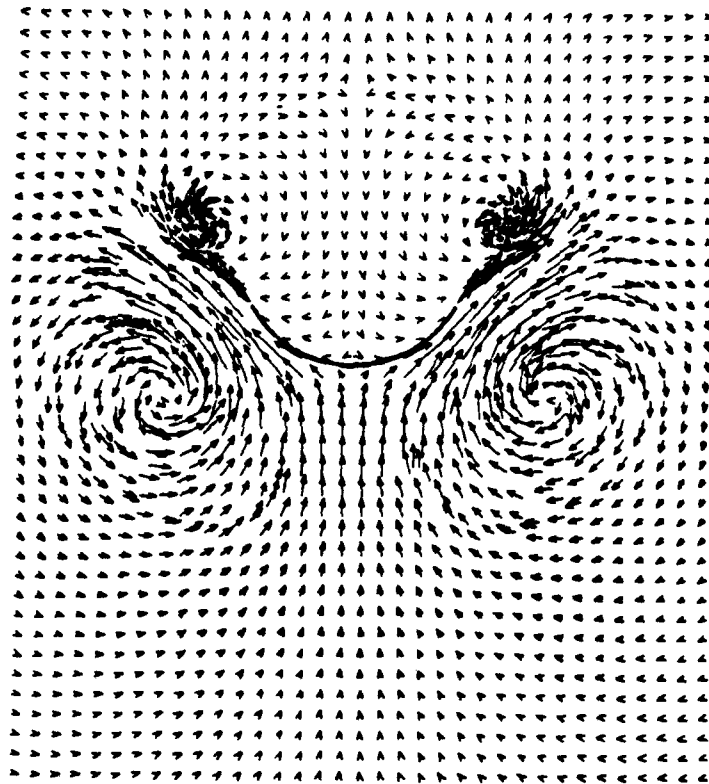


Figure 4.24 Comparison of flow fields at $T^* = 16.30$.

obtained experimentally and points out the fact that the inclusion of the rate of change of circulation term in the impulse method is not in conformity with the behavior of the flow.

The development of negative differential pressures near the central region of the camber is thought to be primarily responsible for the inception of the partial collapse of a parachute at high rates of deceleration. This phenomenon takes place even when the total drag force acting on the parachute is still positive. The sample analysis presented herein also shows that the negative differential pressure can cover a large region of the parachute and even result in negative drag. The basic idea emerging from the analysis reported herein is that the designs which incorporate into them the idea of delaying or preventing the return of the shed vortices to the canopy (e.g. porosity management, change of deceleration history, parachute shape, dissipation and or destruction of the organized wake) will be the ones which could avoid the collapse phenomenon. Extensive analysis and small scale experiments coupled with few judiciously selected field tests may help to arrive at practically and phenomenologically sound parachute designs.

V. CONCLUSIONS

In this chapter the conclusions reached in the preceding sections are summarized and the areas in which the greatest need for further work is perceived are pointed out.

A brief review has shown that two-dimensional finite difference and finite element methods can simulate successfully the low Reynolds number flows but serious impediments remain to extending them to high Reynolds number range that is of practical interest. The major obstacles are: the large computational requirements which grow rapidly with Reynolds number, stability problems, difficulty of implementing boundary conditions and artificial viscosity.

The discrete vortex model is seen to avoid many of the problems of the Eulerian finite difference methods but are subject to some of their own. Chief among these is the introduction of vorticity, determination of the separation points, excessive computation time for the convection of vortices, and the need to introduce artificial dissipation to bring the measured and calculated results into closer agreement.

The first section of this study dealt with the numerical simulation of a sinusoidally oscillating flow about a circular cylinder.

The discrete vortex model has been combined with the boundary layer calculations and the positions of the separation and stagnation points have been calculated as accurately as possible for a Keulegan-Carpenter number of $K = 10$. The results have accurately predicted the formation of a half Karman vortex street in the transverse direction. The calculated positions of the vortices were found to be in good agreement with those obtained experimentally. The measured and calculated drag force and the differential pressure distributions showed reasonably good agreement. The results have also shown that the effect of the backward convection of a large vortex over one side of the cylinder is indeed very pronounced on all the measured and computed characteristics of the flow. This is one of the most important reasons as to why the Morison's equation (see e.g., Sarpkaya & Isaacson 1981) fails to represent the in-line force acting on the cylinder with reasonable accuracy particularly in the range $8 < K < 13$.

The number of numerical parameters involved in the simulation made a complete parametric study of their effects impossible. However, several tests were made in which

the time step and convection scheme were varied. The results showed expected improvements as the time step was reduced and the order of convection scheme was increased but no undue sensitivity was observed.

The application of the discrete vortex model to a particular time-dependent flow past a camber required an extensive study of the velocity field in the vicinity of the sharp edges of the camber. The results have shown that the nascent vortices can be introduced only at judiciously selected points. The numerical experiment predicted satisfactorily the evolution of the wake and the forces acting on the body. Furthermore, the calculations have provided a plausible explanation for the cause of parachute collapse, a phenomenon which has provided the impetus for the simulation described herein.

In the course of the present work, two aspects of the discrete vortex model were identified that seem to be in greatest need for further investigation. The first is the determination of the mobile separation points on a body without sharp edges. The existing methods cannot be considered satisfactory for the prediction of separation in unsteady laminar and or turbulent boundary layers. The use of Pohlhausen's method seemed to produce good results (as judged by the experimental data), but it is the most difficult part of the model to defend.

The second aspect of the model which requires further work is the discovery of a systematic and conceptually satisfactory method to reduce vorticity. It seems clear, at least on the basis of experiments, that there is a physical basis for dissipating vorticity, but it remains to be proved that the global error involved in doing so is reasonable and in conformity with the behavior of nature. Future efforts will probably have to be preceded by careful measurements of the finer details of the unsteady flow field.

APPENDIX A NUMERICAL RESULTS

This section presents additional figures showing the evolution of sinusoidally oscillating flow about a cylinder. It is seen that the convection of the previously shed vortex over the shoulder of the cylinder precipitates earlier separation, establishes a preferred position for the next dominant vortex, and gives rise to additional primary and secondary separation points.

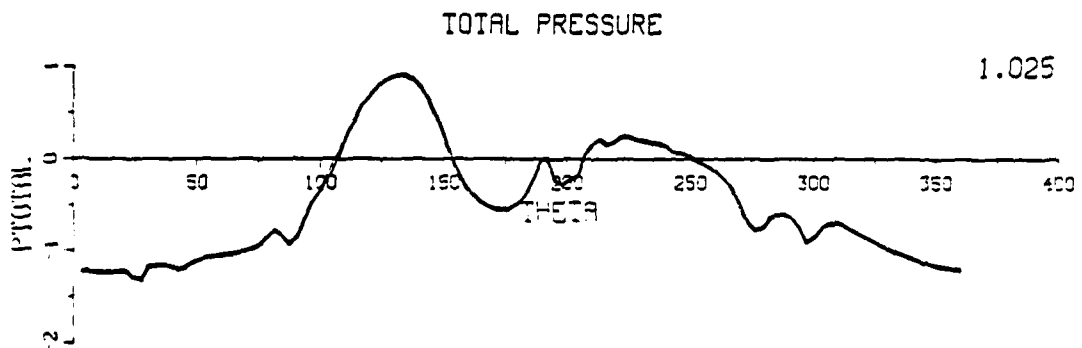
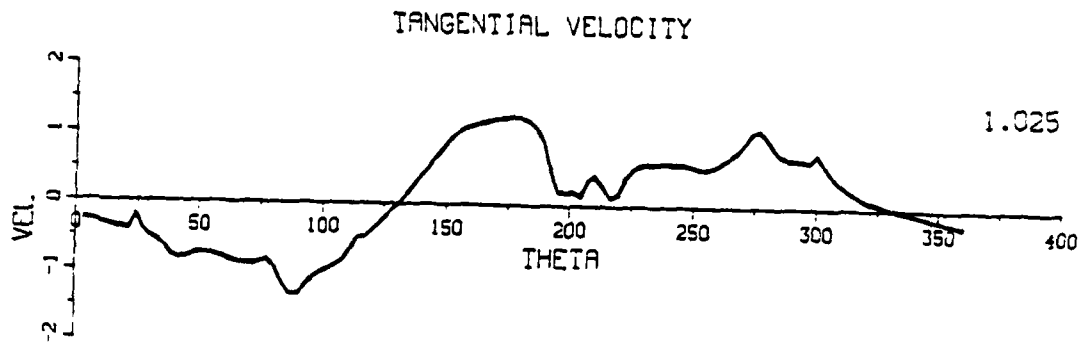
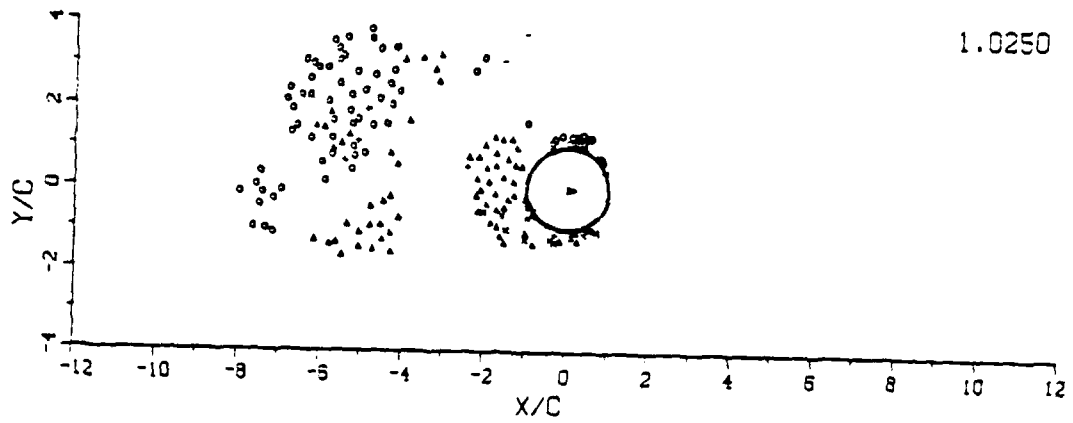


Figure A.1 Position of vortices, velocity and pressure distribution at $T^* = 1.025$.

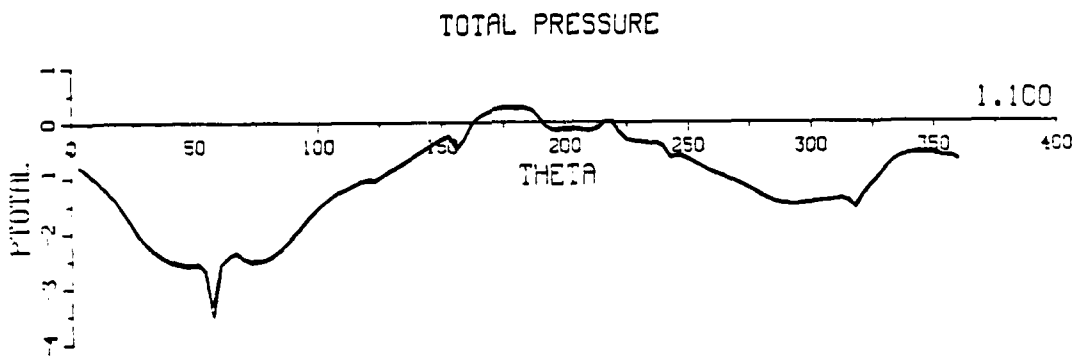
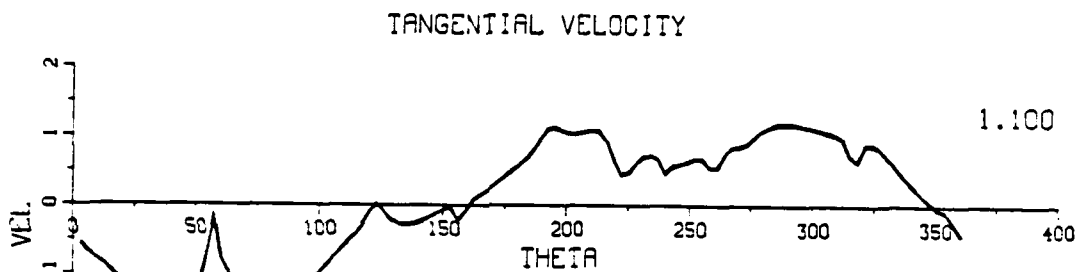
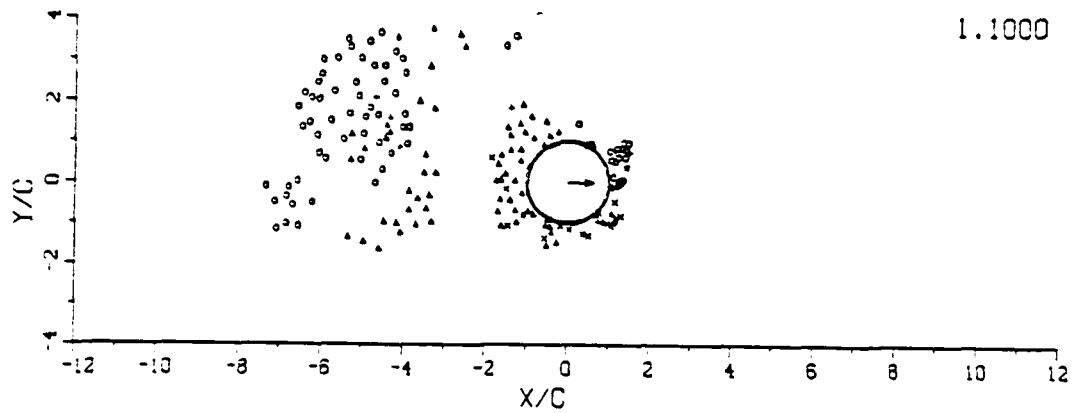


Figure A.2 Position of vortices, velocity and pressure distribution at $T^* = 1.100$.

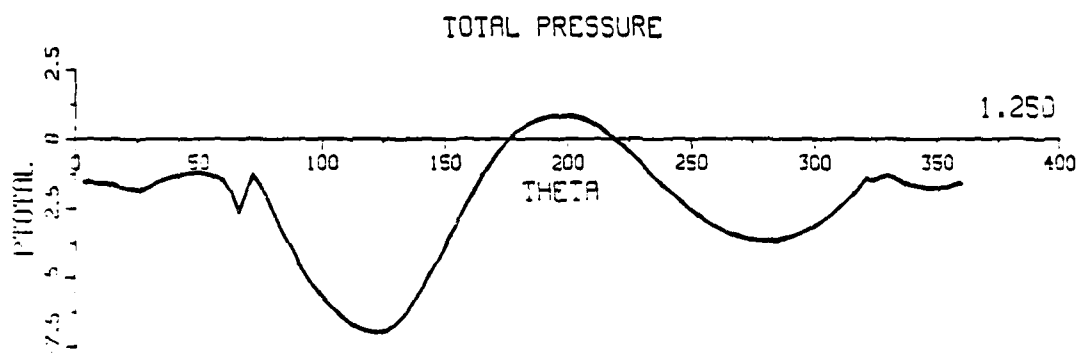
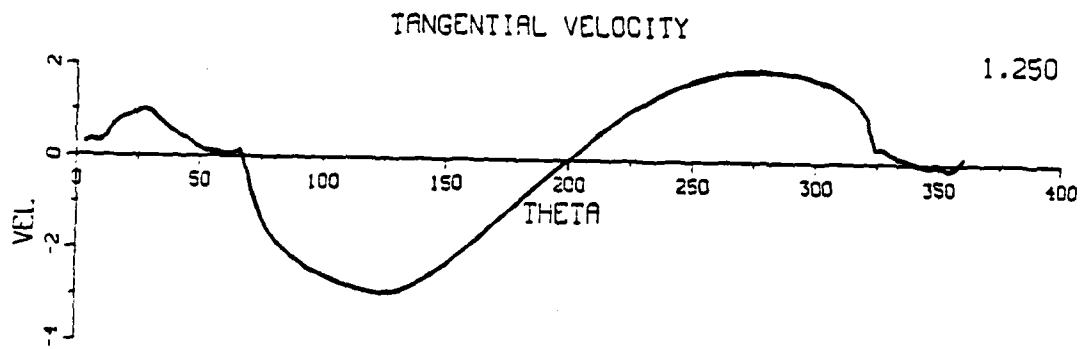
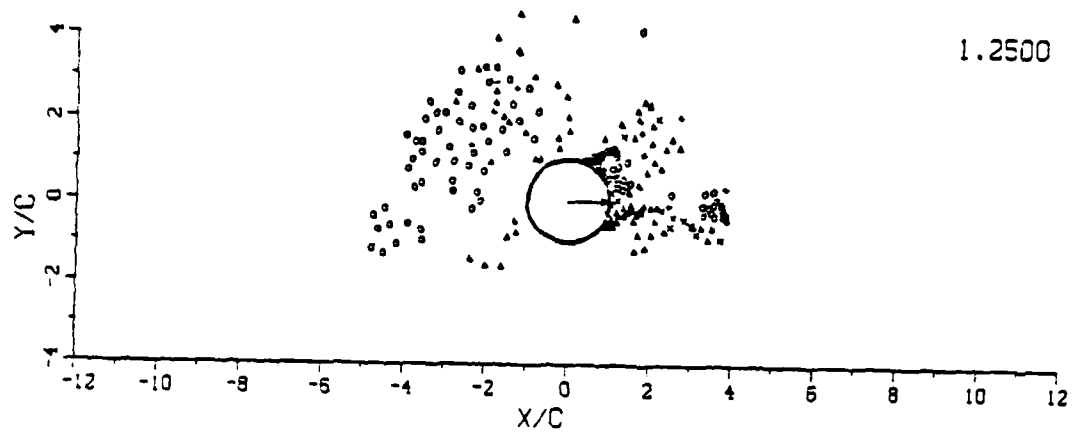


Figure A.3 Position of vortices, velocity and pressure distribution at $T^* = 1.250$.

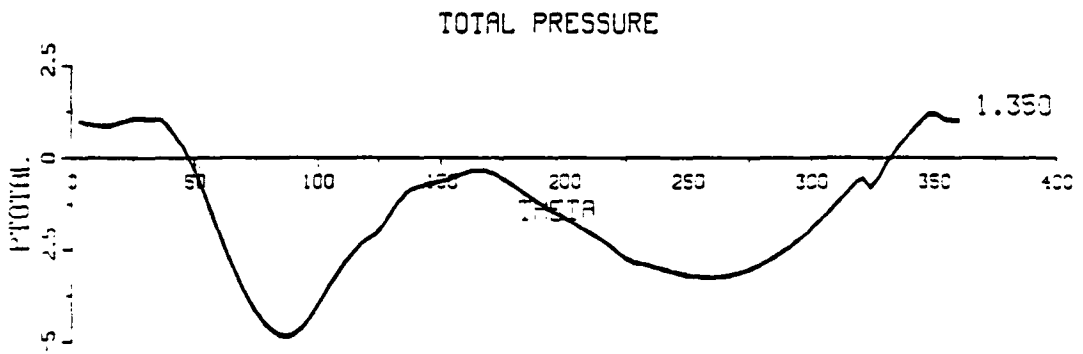
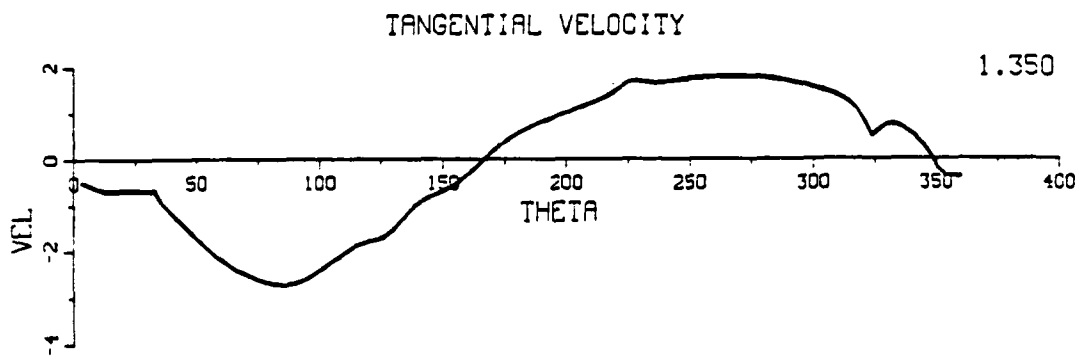
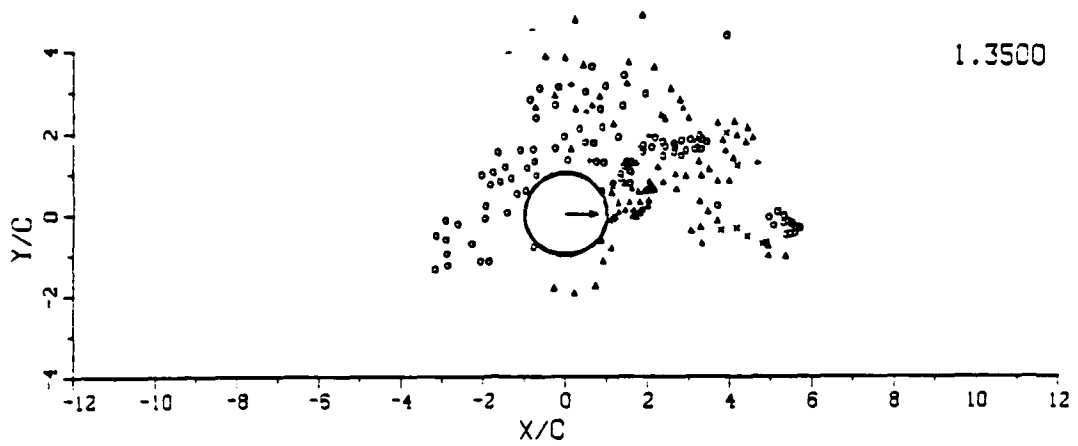


Figure A.4 Position of vortices, velocity and pressure distribution at $T^* = 1.350$.

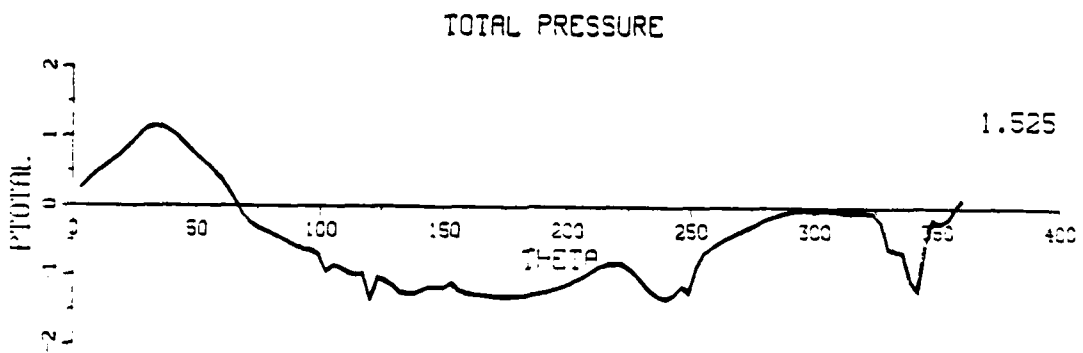
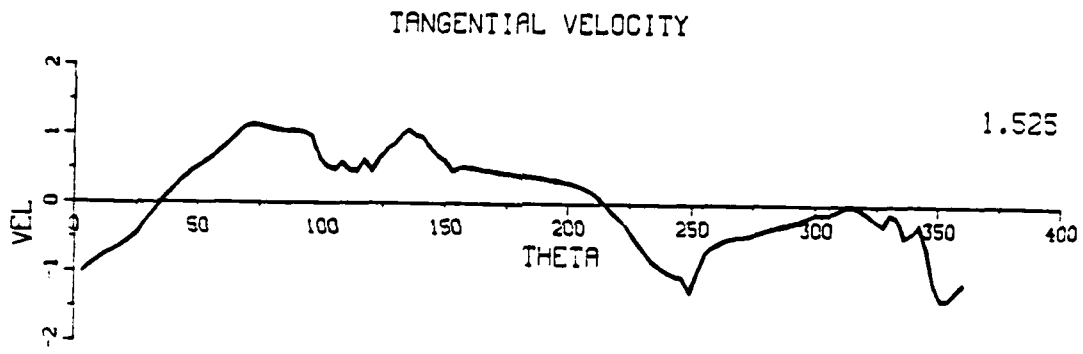
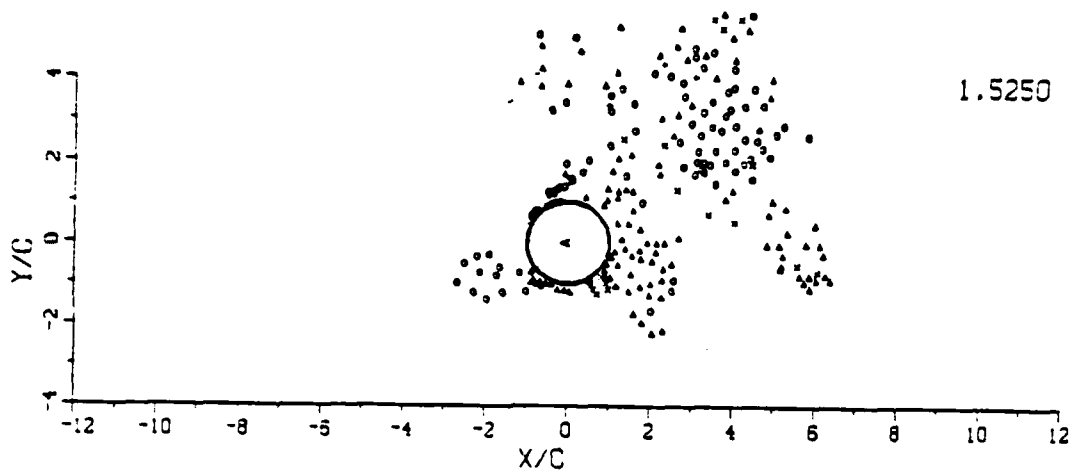


Figure A.5 Position of vortices, velocity and pressure distribution at $T^* = 1.525$.

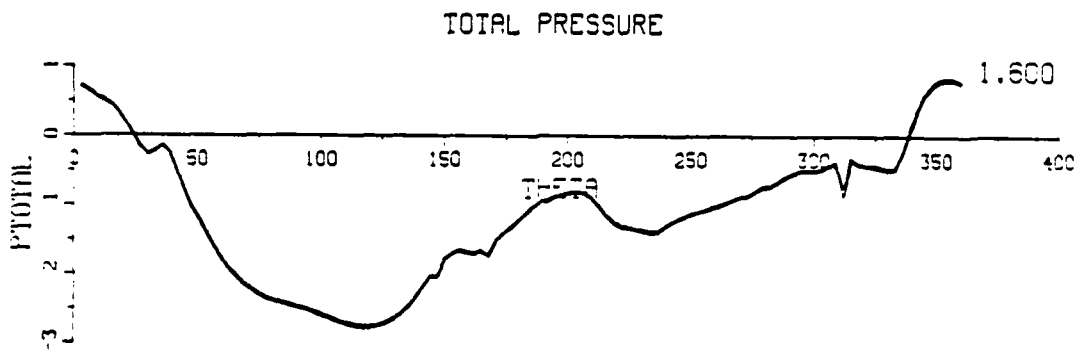
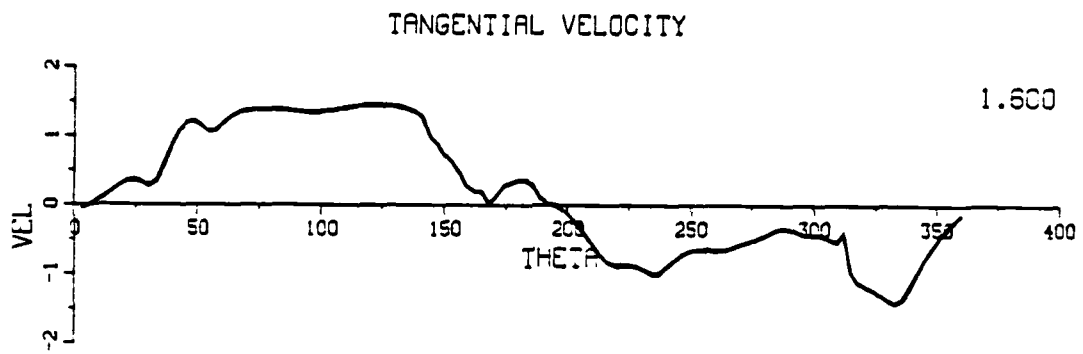
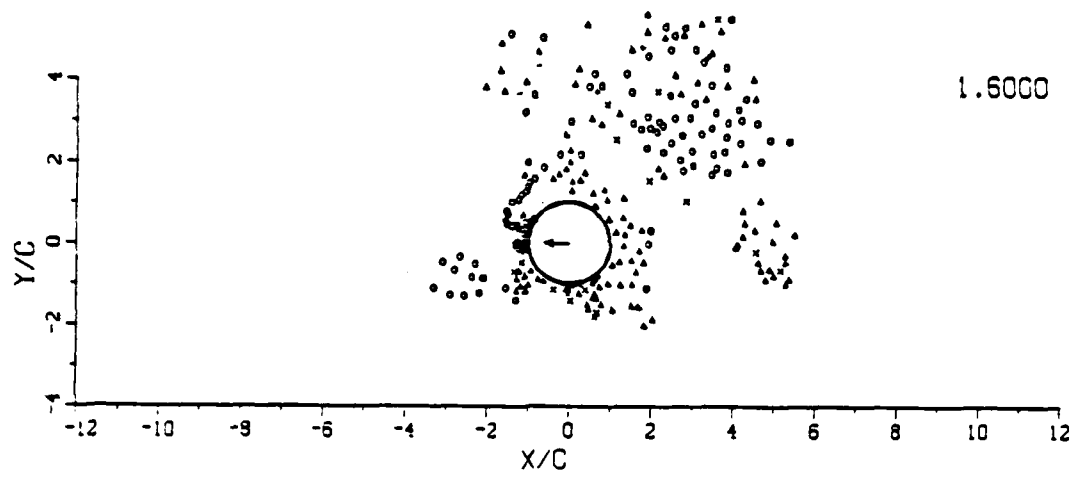


Figure A.6 Position of vortices, velocity and pressure distribution at $T^* = 1.600$.

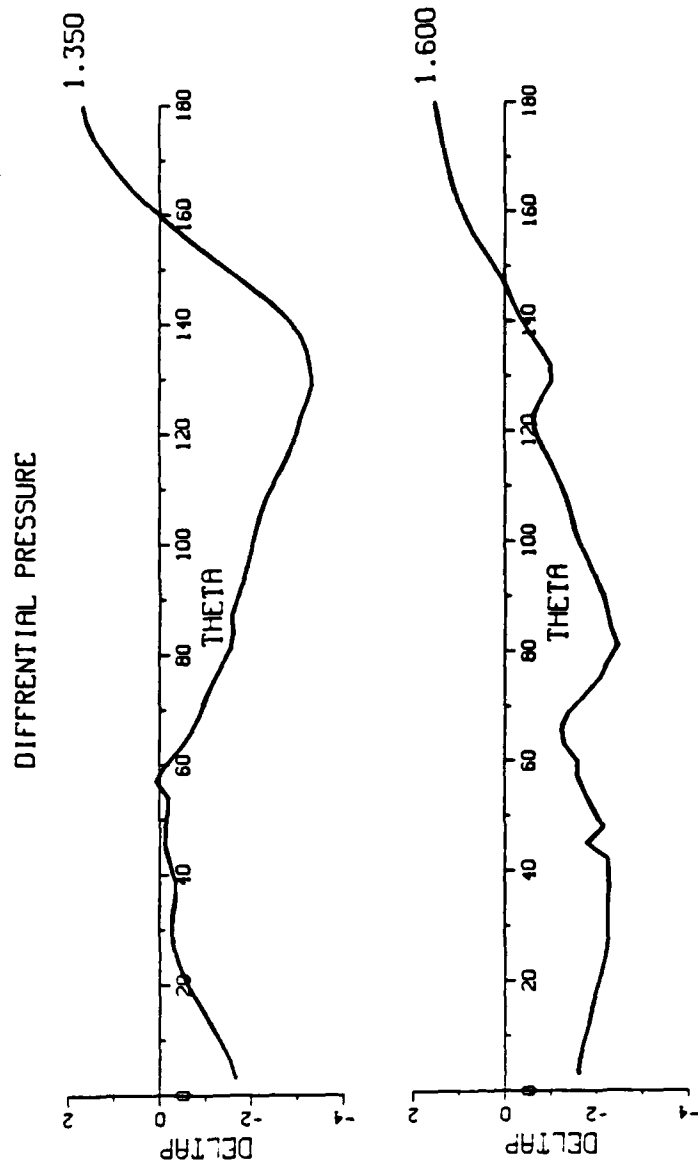


Figure A.7 Differential pressure distributions at $T^* = 1.350$ and 1.600 .

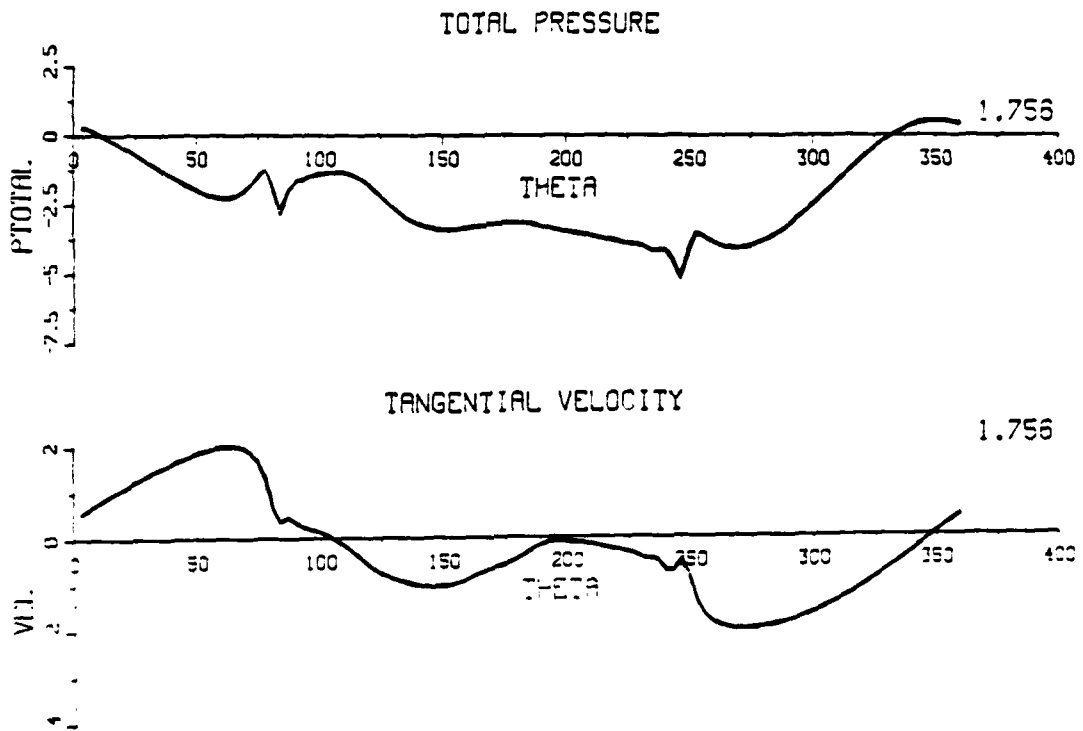
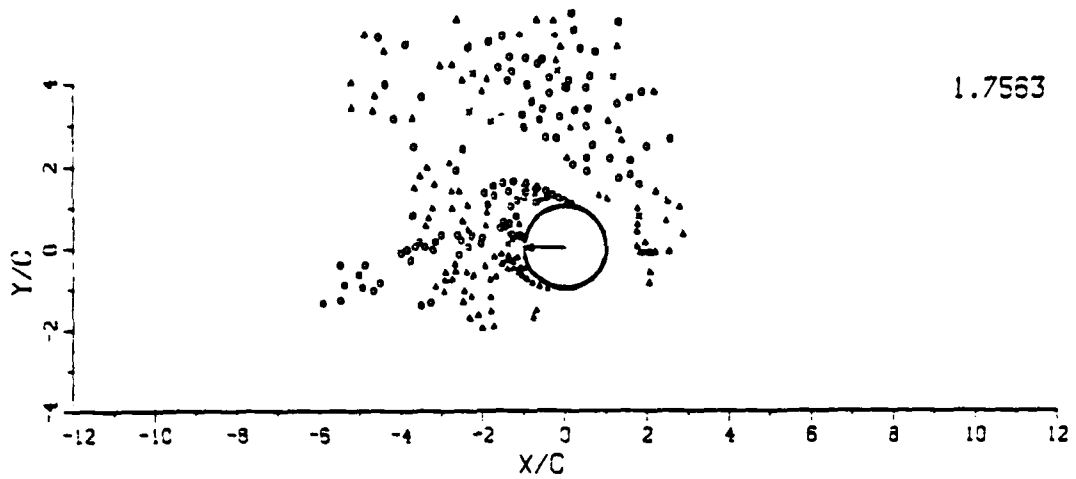


Figure A.8 Position of vortices, velocity and pressure distribution at $T^* = 1.756$.

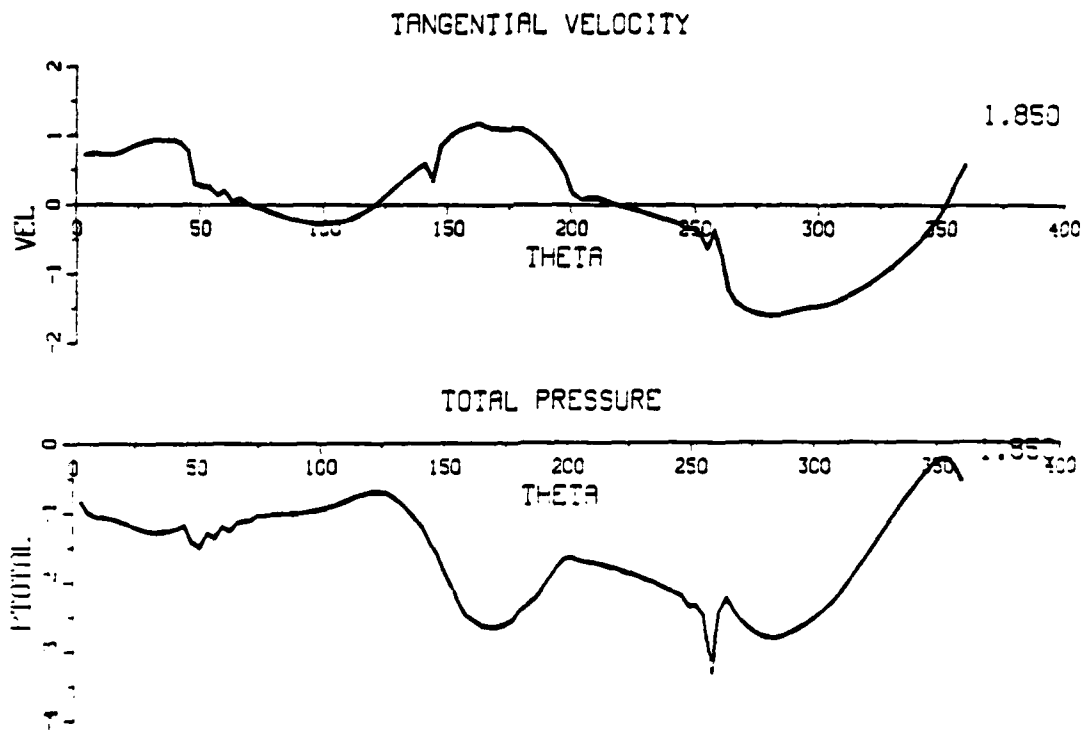
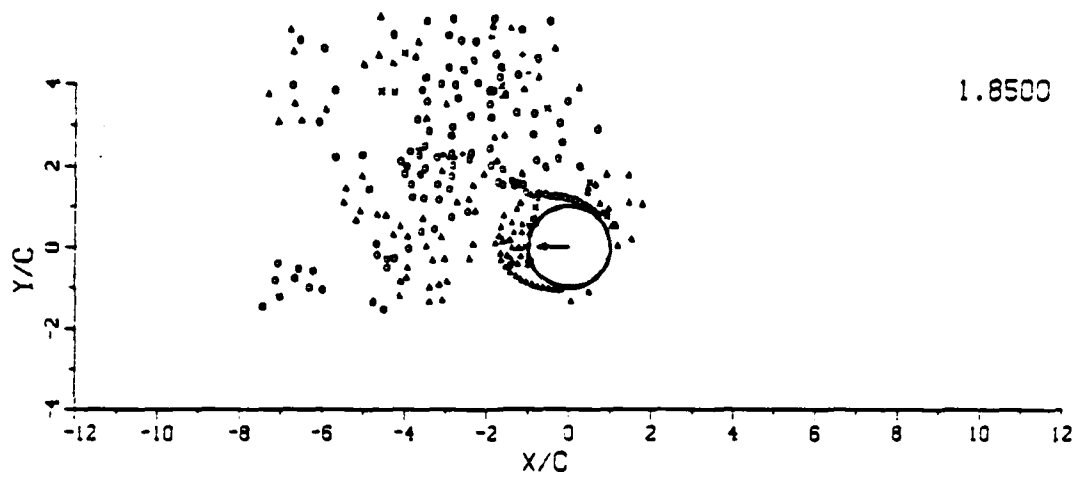


Figure A.9 Position of vortices, velocity and pressure distribution at $T^* = 1.850$.

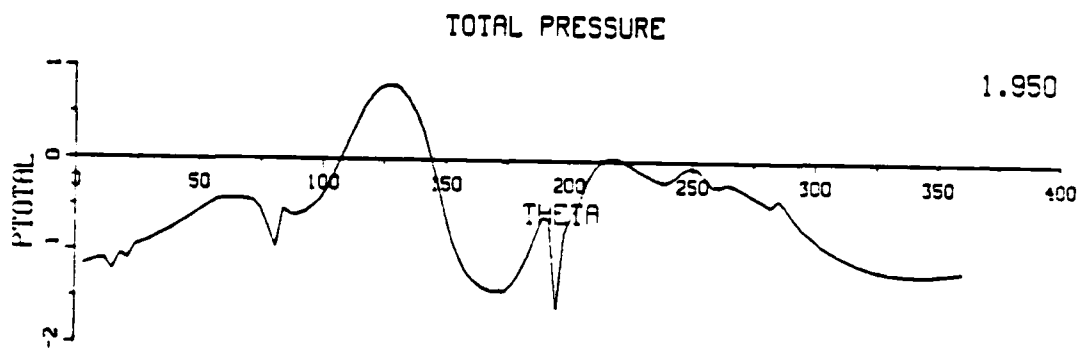
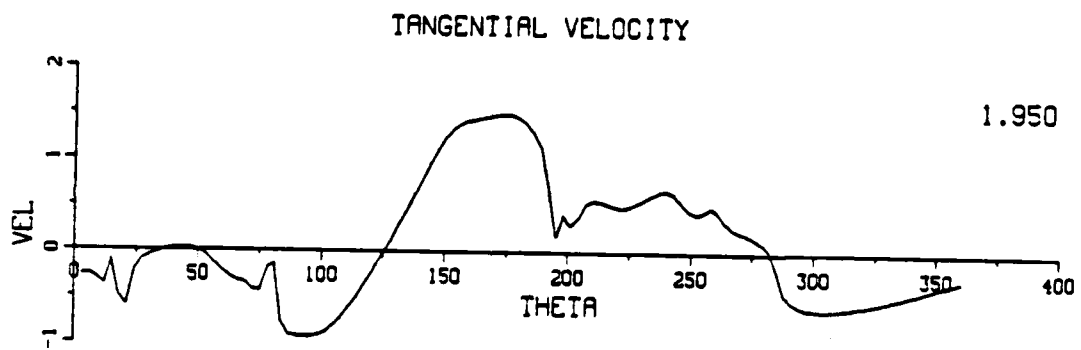
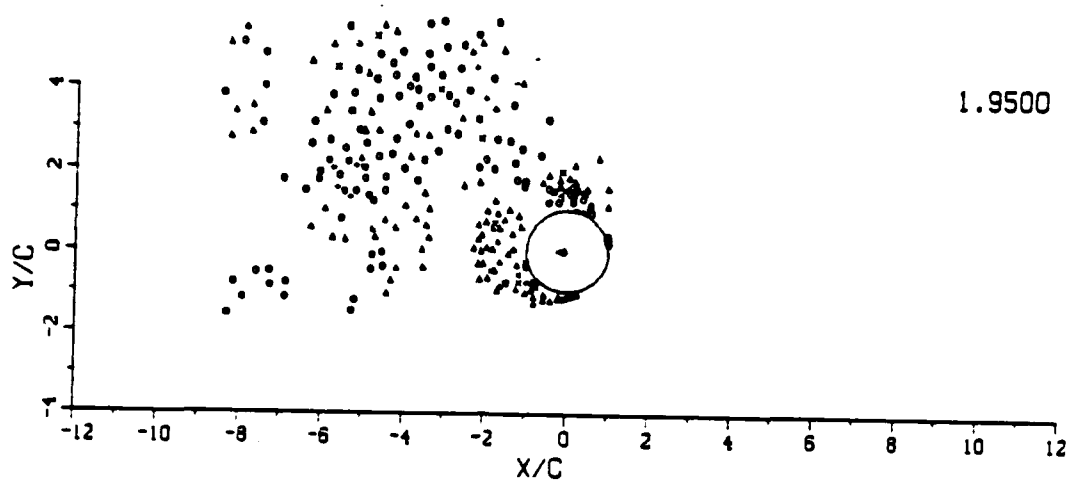


Figure A.10 Position of vortices, velocity and pressure distribution at $T^* = 1.950$.

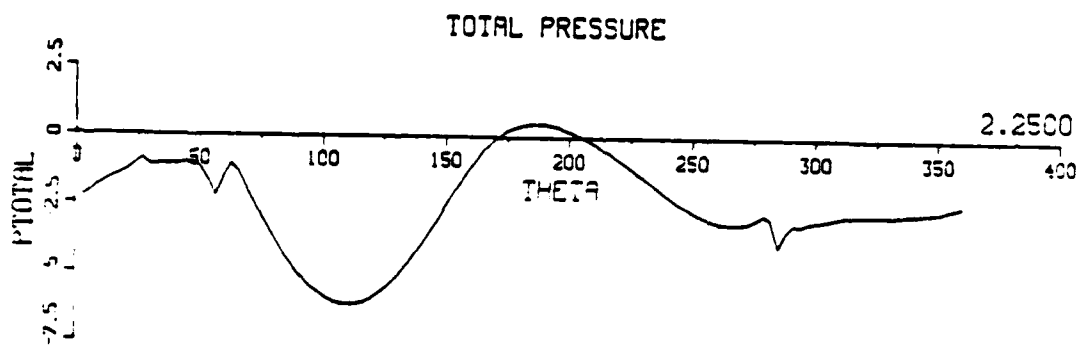
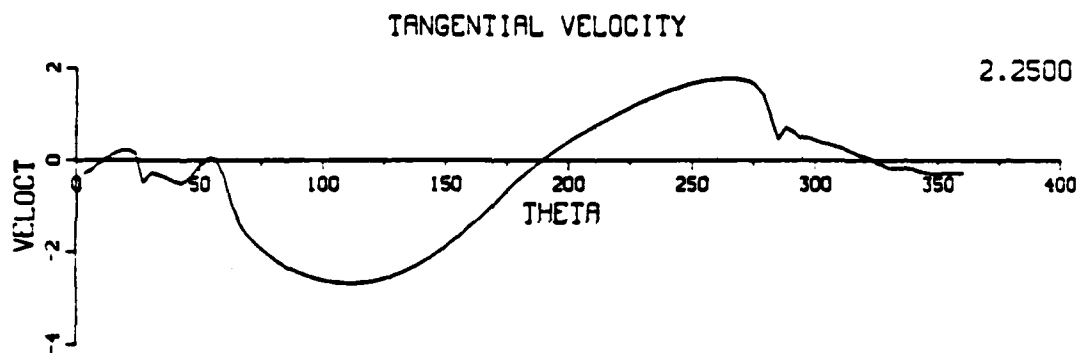
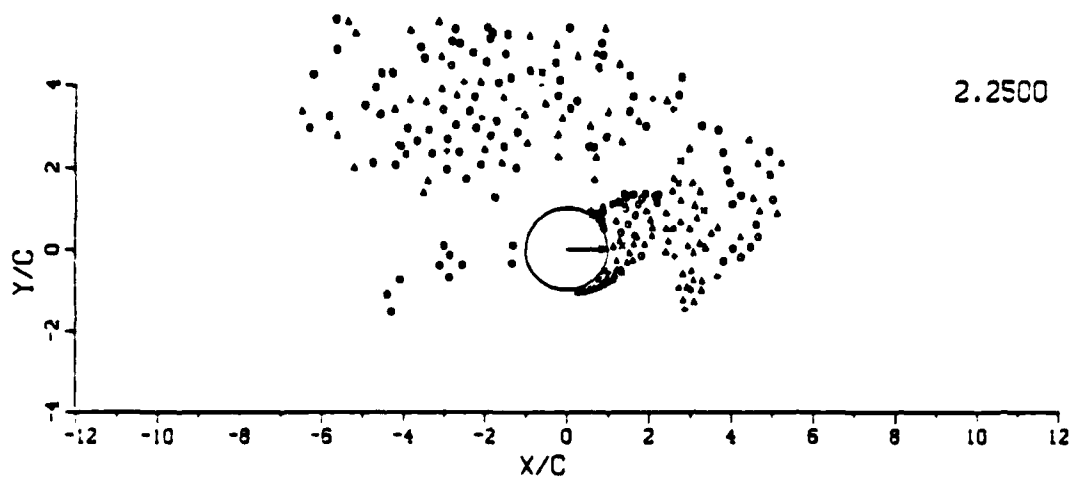


Figure A.11 Position of vortices, velocity and pressure distribution at $T^* = 2.250$.

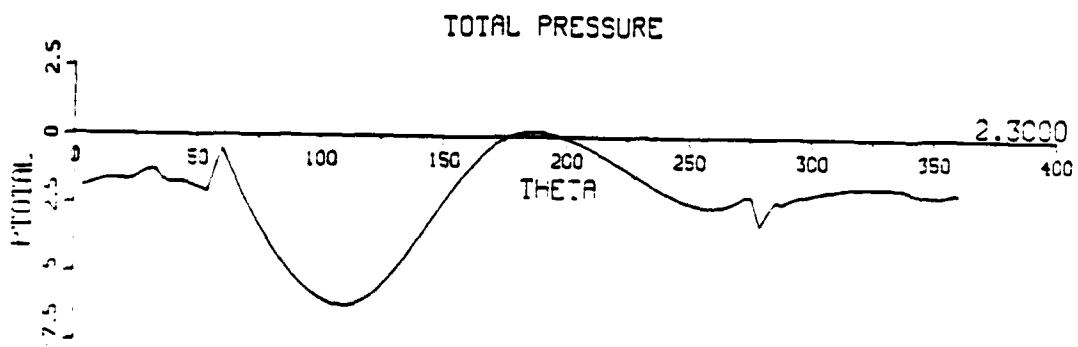
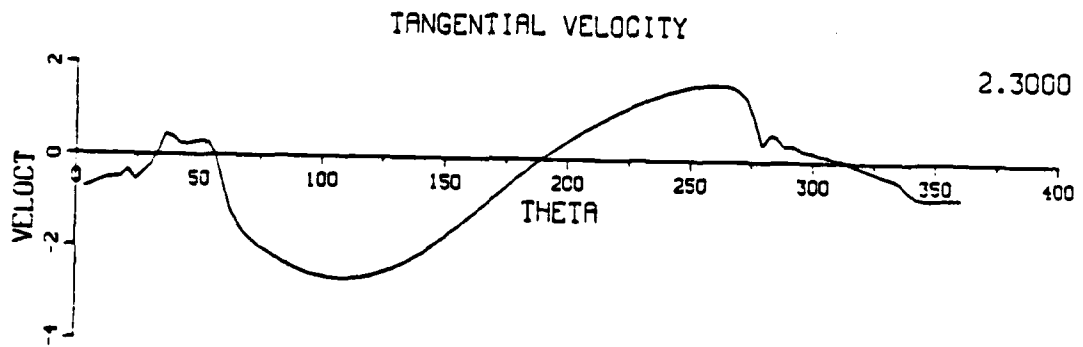
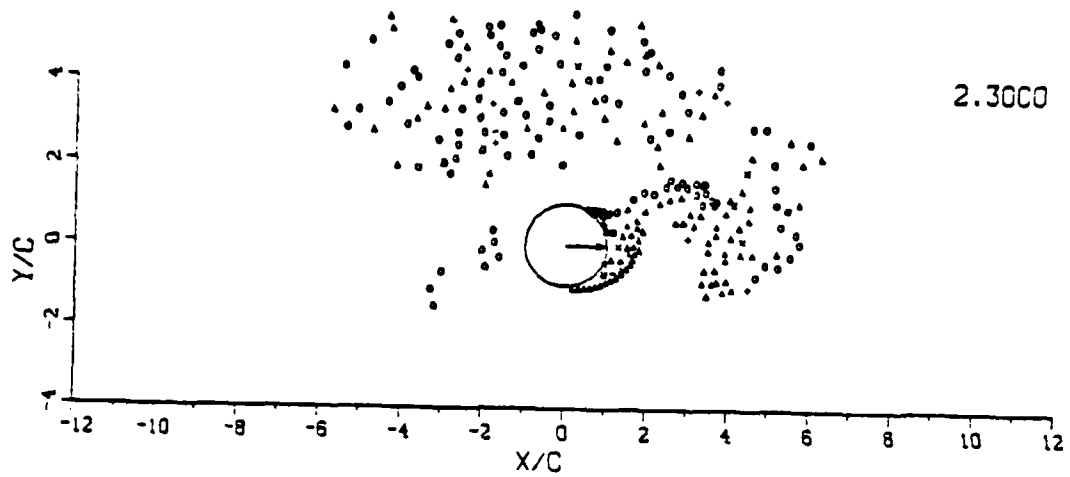


Figure A.12 Position of vortices, velocity and pressure distribution at $T^* = 2.300$.

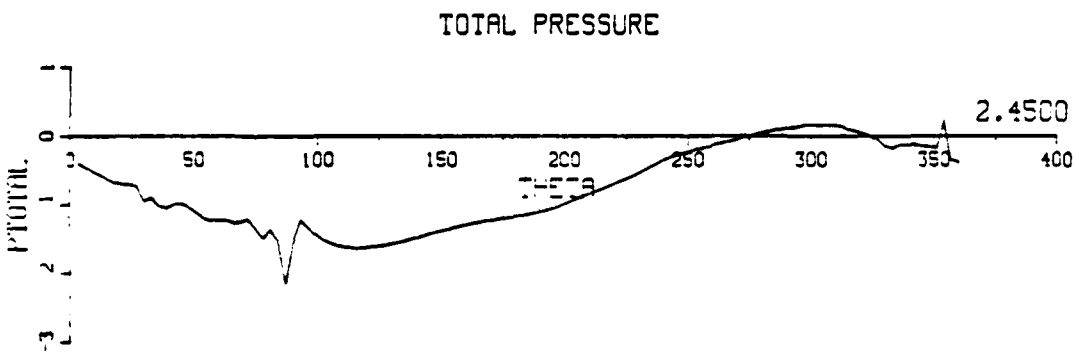
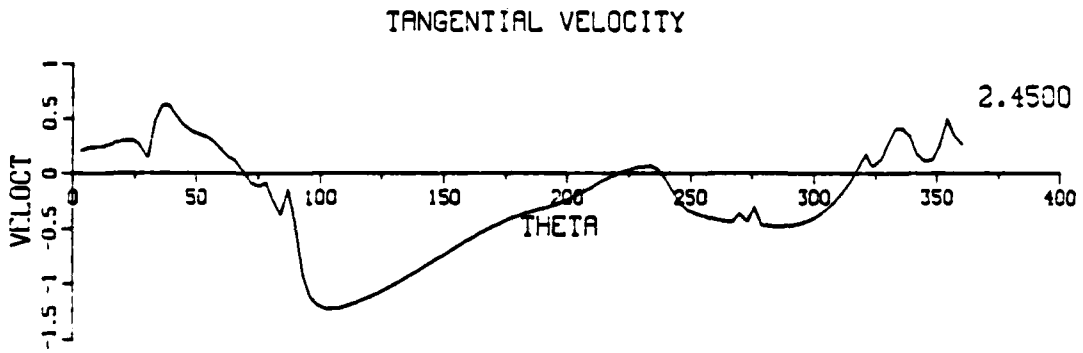
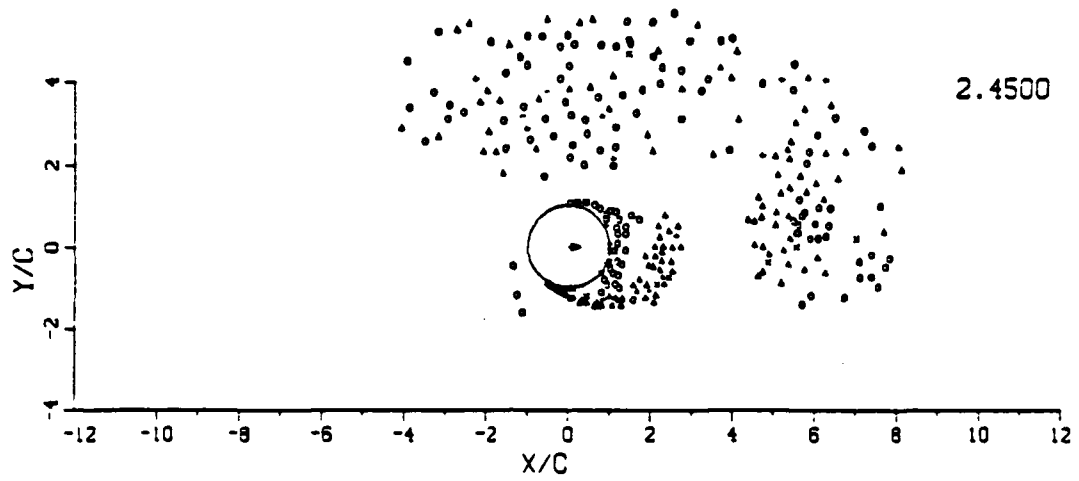
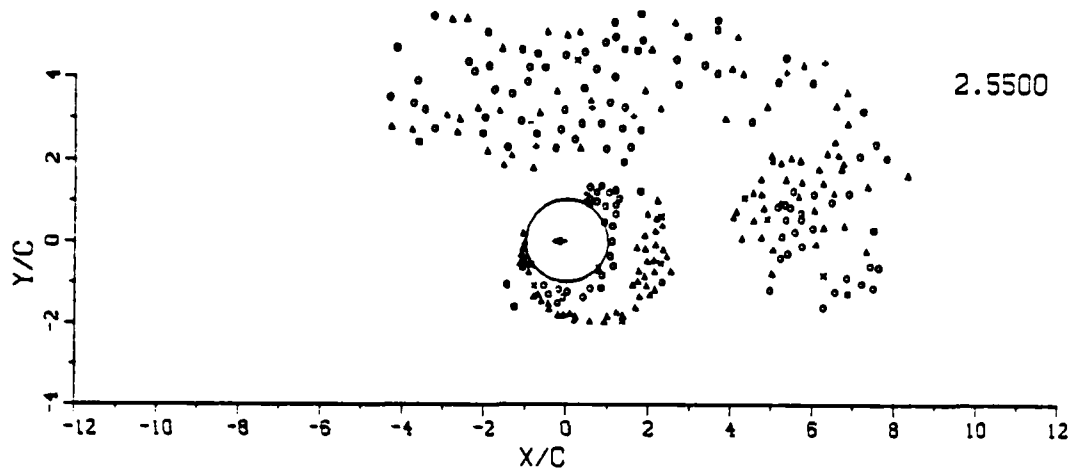
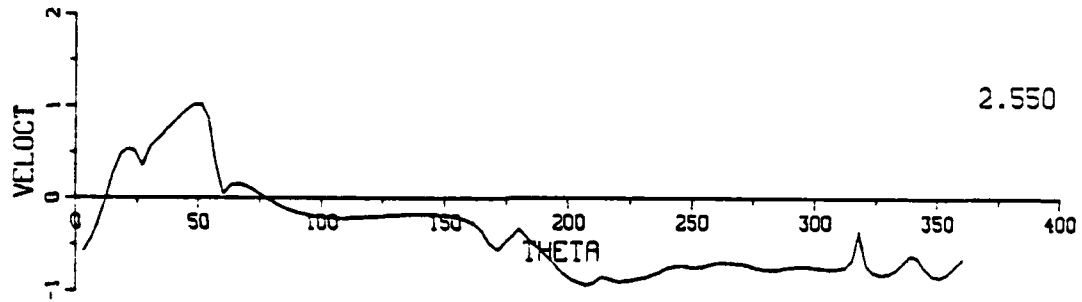


Figure A.13 Position of vortices, velocity and pressure distribution at $T^* = 2.450$.



TANGENTIAL VELOCITY



TOTAL PRESSURE

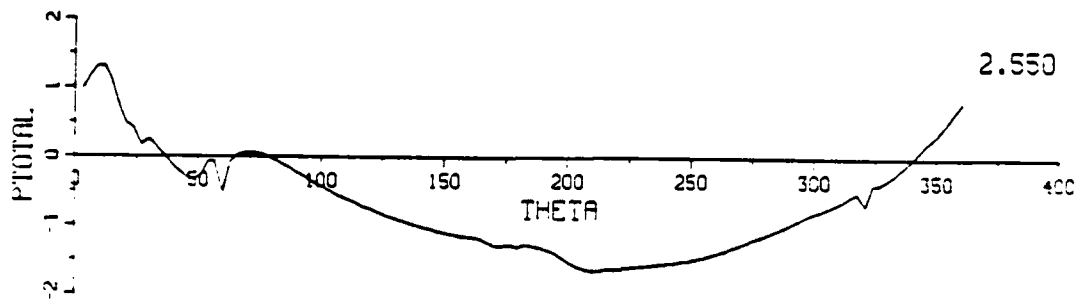


Figure A.14 Position of vortices, velocity and pressure distribution at $T^* = 2.550$.

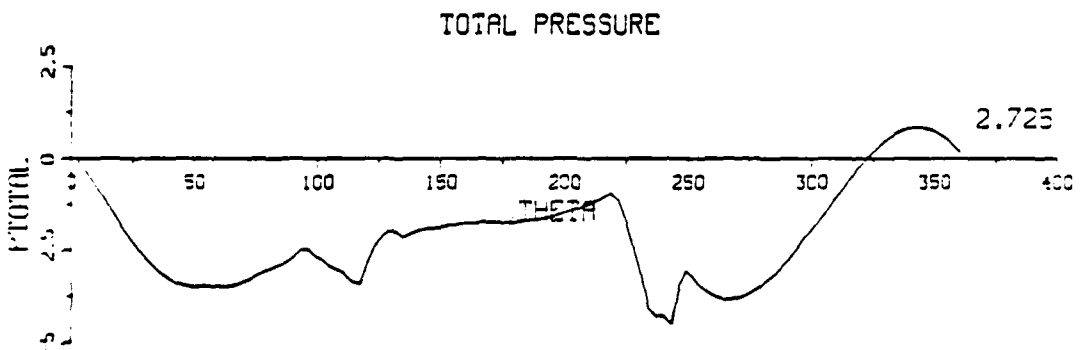
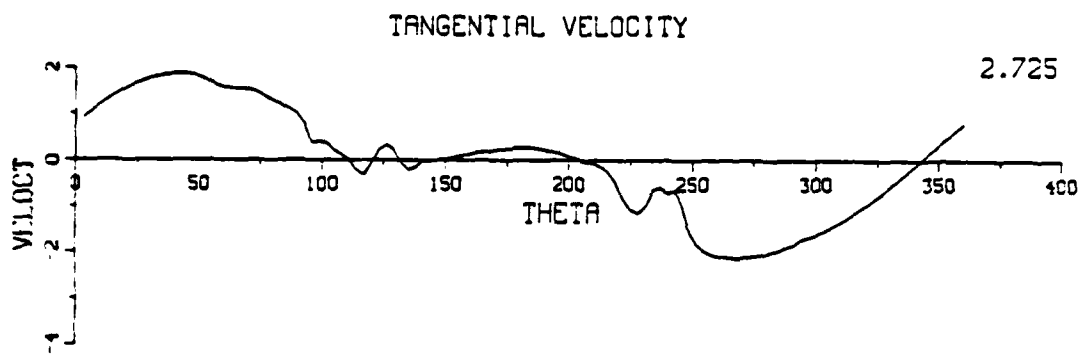
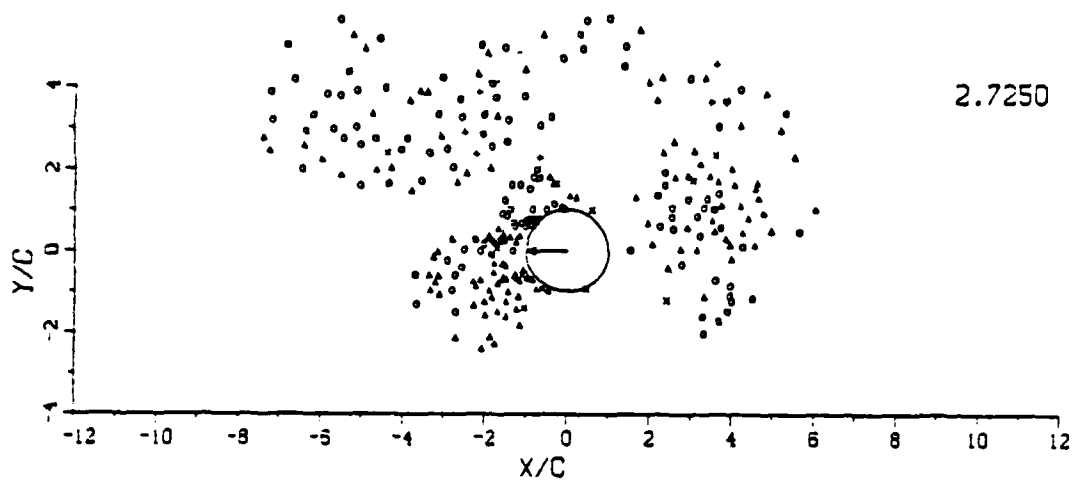


Figure A.15 Position of vortices, velocity and pressure distribution at $T^* = 2.725$.

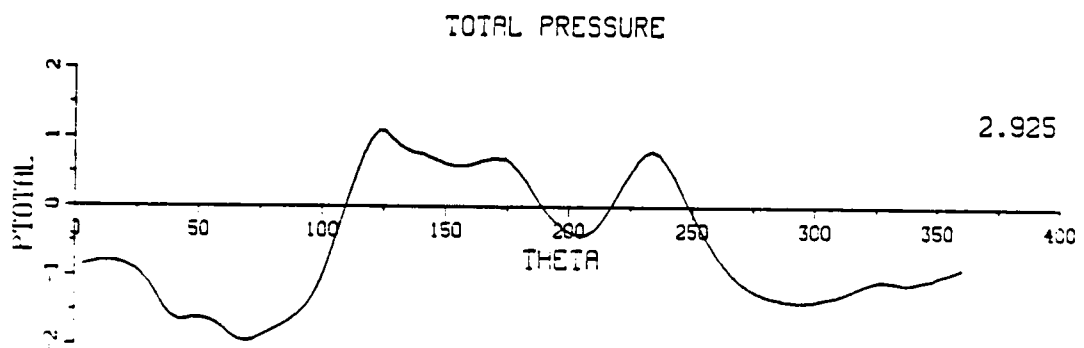
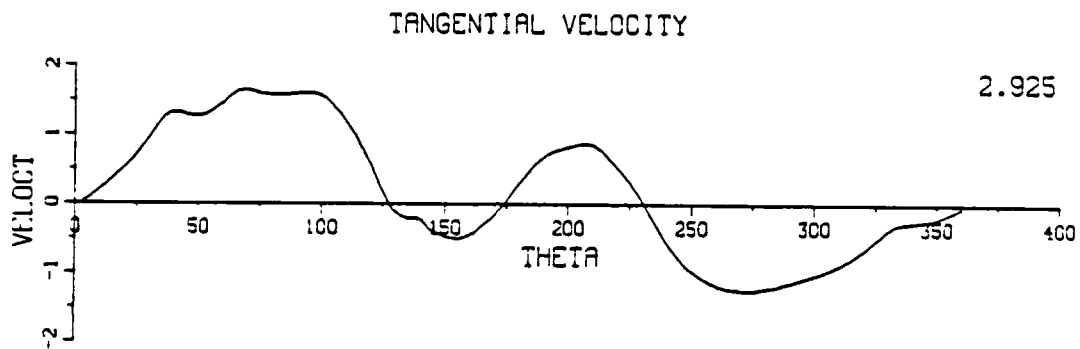
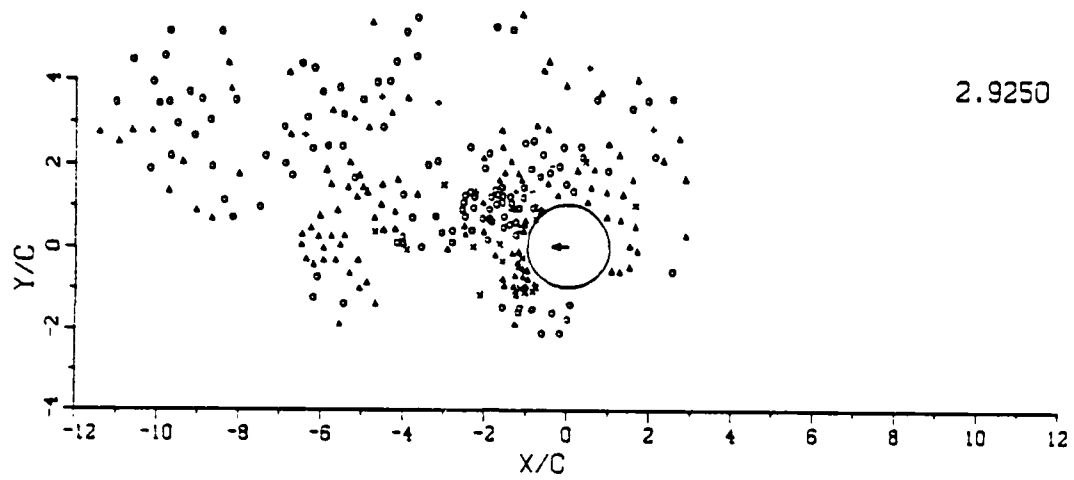


Figure A.16 Position of vortices, velocity and pressure distribution at $T^* = 2.925$.

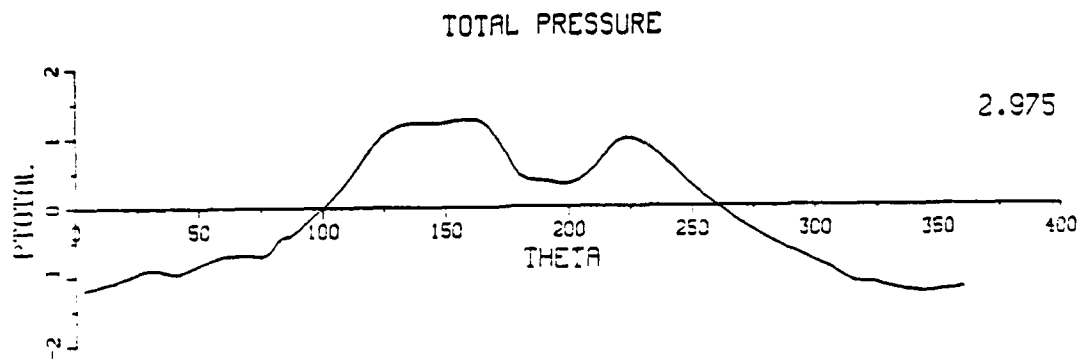
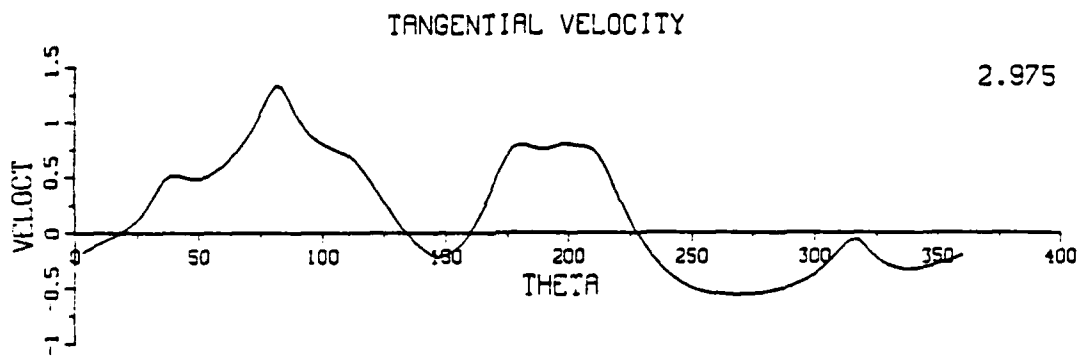
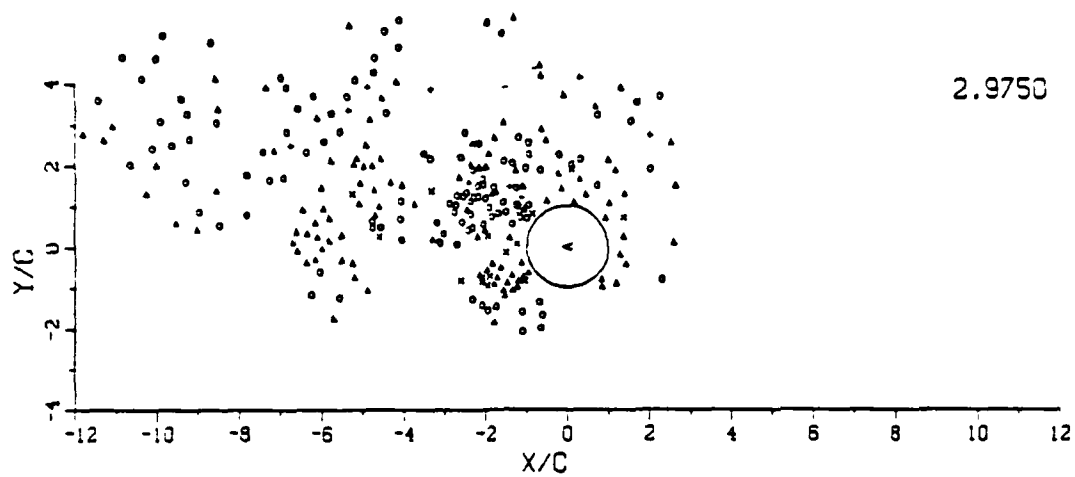


Figure A.17 Position of vortices, velocity and pressure distribution at $T^* = 2.975$.

LIST OF REFERENCES

- Bearman, P. W. 1985. "Vortex Trajectories in Oscillating Flow," in *Proceedings of Separated Flow Around Marine Structures* Trondheim, Norway. pp. 133-135. The Norwegian Institute of Technology, Trondheim, Norway.
- Bradbury, L. J. S., Durst, F., Launder, B. E., Schmidt, F.W., and Whitelaw, J. H. Eds. 1982. *Turbulent Shear Flows-III*, Springer-Verlag, New York.
- Carr, L. W. 1981. "A Review of Unsteady Turbulent Boundary-Layer Experiments," in *Unsteady Turbulent Shear Flows* (Eds: R. Michael et al.), Springer-Verlag, N. Y., pp. 3-34.
- Chorin, A.J. 1973. "Numerical Study of Slightly Viscous Flow," *Journal of Fluid Mechanics* Vol. 57, pp. 785-96.
- Clements, R. 1973. "An Inviscid Model of Two-Dimensional Vortex Shedding," *Journal of Fluid Mechanics* Vol. 57, pp. 321-335.
- Davis, R. W. and Moore, E. F. 1982. "A Numerical Study of Vortex Shedding from Rectangles," *Journal of Fluid Mechanics* Vol. 116, pp. 475-506.
- Fage, A. and Johansen, R. C., 1928. "The Structure of Vortex Sheets," *Aeronautical Research Council R&M*, No. 1143.
- Gerrard, J. H. 1966. "The Mechanics of the Formation Region of Vortices behind Bluff Bodies," *Journal of Fluid Mechanics* Vol. 25, pp. 401-413.
- Gresho, P. M., Chan, S. T., Lee, R. L. and Upson, C. D. 1984. "A Modified Finite Element Method for Solving the Time Dependent, Incompressible Navier-Stokes Equations, Part 2: Applications," *International Journal of Numerical Methods in Fluids* Vol. 4, pp. 619-640.
- Heinrich, H. G. and Saari, D. P. 1978. "Parachute Opening Shock Calculations with Experimentally Established Input Functions," *Journal of Aircraft* Vol. 15, No. 2, pp. 100-105.
- Ikeda, Y., and Himeno, Y. 1981. "Calculation of Vortex-Shedding Flow around Oscillating Circular and Lewis-form Cylinder," *Proceedings Third International Conference on Numerical Ship Hydrodynamics* Paris: Bassin d'Essais des Carenes, pp. 335-346.
- Kiya, M. and Arie, M. 1977. "A Contribution to an Inviscid Vortex-Shedding Model for an Inclined Flat Plate in Uniform Flow," *Journal of Fluid Mechanics* Vol. 82, pp. 223-240.
- Klimas, P. C. 1977. "Fluid Mass Associated with an Axisymmetric Parachute Canopy," *Journal of Aircraft* Vol. 14, No. 6 pp. 577-580.

- Kudo, K. 1979. "An Inviscid Model of Discrete-Vortex Shedding for Two-Dimensional Oscillating Flow around a Flat Plate," *Journal of the Society of Naval Architects of Japan* 145, pp. 54-62.
- Kuwahara, K. 1973. "Numerical Study of Flow Past an Inclined Flat Plate by an Inviscid Model," *Journal of the Physical Society of Japan* Vol. 35, pp. 1545-1553.
- Lecoq, Y. and Piquet, J. 1984. "On the Use of Several Compact Methods for the Study of Unsteady Incompressible Viscous Flow Round a Circular Cylinder," *Computers in Fluids* Vol. 12, pp. 255-280.
- McWey, D. F. and Wolf, D. F. 1972. "Analysis of Deployment and Inflation of Large Ribbon Parachutes," *Journal of Aircraft* Vol. 11, pp. 96-103.
- Moore, F. K. 1958. "On the Separation of Unsteady Laminar Boundary Layer," UTAM Symposium, Boundary Layers, Freiberg, pp. 296-311.
- Muramoto, K. K. and Garrard, W. L. 1984. "A Method for Calculating the Pressure Field about a Ribbon Parachute Canopy in Steady Descent," AIAA 8th Aerodynamic Decelerator and Balloon Technology Conference, Hyannis, Mass., AIAA-84-0794.
- Roache, P. J. 1972. "On Artificial Viscosity," *Journal of Computational Physics* Vol. 10, pp. 169-184.
- Roshko, A. 1954. "On the Drag and Shedding Frequency of Two-Dimensional Bluff Bodies," *NACA Technical Note* No. 3169.
- Rott, N. 1956. "Unsteady Viscous Flow in the Vicinity of a Stagnation Point," *Quarterly Applied Mathematics* Vol. 13, pp. 444-451.
- Sarpkaya, T. 1967. "Separated Unsteady Flow about a Rotating Plate," in *Developments in Mechanics* Vol. 4, pp. 1485-1499.
- Sarpkaya, T. 1968. "An Analytical Study of Separated Flow about Circular Cylinders," *Journal of Basic Engineering* Trans. ASME, Vol. D-90, pp. 511-520.
- Sarpkaya, T. 1975. "An Inviscid Model of Two-Dimensional Vortex Shedding for Transient and Asymptotically Steady Separated Flow over an Inclined Plate," *Journal of Fluid Mechanics* Vol. 68, pp. 109-128.
- Sarpkaya, T. 1985. "Past Progress and Outstanding Problems in Time-Dependent Flows about Ocean Structures," *Separated Flow Around Marine Structures* Trondheim: The Norwegian Institute of Technology, pp. 1-36.
- Sarpkaya, T., and Ihrig, C. J. 1986. "Impulsively Started Flow about Rectangular Prisms: Experiments and Discrete Vortex Analysis," *Journal of Fluids Engineering* Vol. 108, pp. 47-54.
- Sarpkaya, T. 1986. "Forces on a Circular Cylinder in Viscous Oscillating Flow at Low Keulegan-Karpenter Numbers," *Journal of Fluid Mechanics* Vol. 165, pp. 61-71.
- Sarpkaya, T., and Shoaff, R.L. 1979. "Discrete Vortex Analysis of Flow about Stationary and Transversely Oscillating Circular Cylinders," Report No. Nps-69SL79011, Naval Postgraduate School, Monterey, Ca. (see also "Inviscid Model of Two-Dimensional Vortex Shedding by a Circular Cylinder," *AIAA Journal* 17 (11), pp. 1193-1200).

- Sarpkaya, T., and Wilson, J.R. 1984. "Pressure Distribution on Smooth and Rough Cylinders in Harmonic Flow," *Proceedings Ocean Structural Dynamics Symposium '84* Corvallis, Oregon State University, pp. 341-55.
- Sawaragi, T., and Nakamura, T. 1979. "Analytical Study of Wave Force on a Cylinder in Oscillating Flow," *Coastal Structures* Vol. I. New York: American Society of Civil Engineers, pp. 154-73.
- Sears, W. R. 1976. "Unsteady Motion of Airfoils with Boundary-Layer Separation," *AIAA Journal* Vol. 14, pp. 216-220.
- Schlichting, H. 1932. "Berechnung ebener Periodischer Grenzschichtströmungen," *Physikalischer Zeitschrift*. XXXIII, pp. 327-35.
- Stansby, P.K. 1977. "An Inviscid Model of Vortex Shedding from a Circular Cylinder in Steady and Oscillatory far Flows," *Proceedings of the Institution of Civil Engineers* Vol. 63 (2), pp. 865-80.
- Stansby, P.K. 1979. "Mathematical Modelling of Vortex Shedding from Circular Cylinders in Planar Oscillatory Flows, Including Effects of Harmonics," *Mechanics of Wave-Induced Forces on Cylinders* (ed. T.I. Shaw), Marshfield, Ma., pp. 450-60.
- Stansby, P.K., 1981. "The Force on a Cylinder in Sinusoidal Flow," *American Society of Mechanical Engineers Paper 81-Wa:FE27*.
- Stansby, P.K., and Dixon, A.G. 1982. "The Importance of Secondary Shedding in Two-Dimensional Wake Formation at Very High Reynolds Numbers," *The Aeronautical Quarterly* XXXIII (2), pp. 105-23.
- Ward, E.G., and Dalton, C. 1969. "Strictly Sinusoidal Flow around a Stationary Cylinder," *Transactions of the American Society of Mechanical Engineers, Journal of basic Engineering* Vol. 91, pp. 141-74.
- Williamson, C. H. K. 1985. "Sinusoidal Flow Relative to Circular Cylinders," *Journal of Fluid Mechanics* Vol. 155, pp. 141-174.

INITIAL DISTRIBUTION LIST

		No. Copies
1.	Defense Technical Information Center Cameron Station Alexandria, VA 22304-6145	2
2.	Library, Code 0142 Naval Postgraduate School Monterey, CA 93943-5002	2
3.	Department Chairman, Code 69 Naval Postgraduate School Monterey, CA 93943-5000	2
4.	Prof. T. Sarpkaya Code 69SL Naval Postgraduate School Monterey, CA 93943-5000	6
5.	Maj. Gen. Moustafa Eid Moustafa 2308 Tracy Place, N. W. Washington, D. C. 20008	1
6.	Dr. Taymour Hussin Kamal Atomic Energy Authority P.O.Box 13759, Cairo, Egypt	2
7.	LCDR. P. Munz, USN 39 Eagle Lane Hauppuge, N. Y. 11788	1
8.	Col. Samir I. Mostafa Mechanical Engineering Dpt. Naval Postgraduate School Monterey, CA 93943-5000	5
9.	Library of Faculty of Engineering Cairo University El-Gamaa Street, Giza, Egypt	1
10.	Ministry of Defense Kobri El-Kobba, Cairo, Egypt	2

END

10-87

DTIC